Environmentally benign three-dimensional aerogels for air filtration and the mechanisms

Ma, Daphne Xiu Yun

2020

Ma, D. X. Y. (2020). Environmentally benign three-dimensional aerogels for air filtration and the mechanisms. Doctoral thesis, Nanyang Technological University, Singapore.
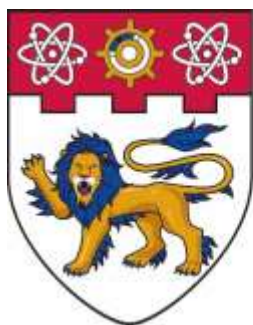
https://hdl.handle.net/10356/146137

https://doi.org/10.32657/10356/146137

ENVIRONMENTALLY BENIGN THREE-DIMENSIONAL AEROGELS FOR AIR FILTRATION AND THE MECHANISMS

MA XIU YUN, DAPHNE
Interdisciplinary Graduate School
Energy Research Institute @NTU (ERI@N)

2020

ENVIRONMENTALLY BENIGN THREE-DIMENSIONAL AEROGELS FOR AIR FILTRATION AND THE MECHANISMS

MA XIU YUN, DAPHNE

Interdisciplinary Graduate School
Energy Research Institute @NTU (ERI@N)

A thesis submitted to the Nanyang Technological University in partial fulfillment of the requirement for the degree of
Doctor of Philosophy

2020

Statement of Originality

I hereby certify that the work embodied in this thesis is the result of original research,

is free of plagiarised materials, and has not been submitted for a higher degree to any

other University or Institution.

21/08/2020
. . . .
Date   Ma Xiu Yun, Daphne

Supervisor Declaration Statement

I have reviewed the content and presentation style of this thesis and declare it is free of plagiarism and of sufficient grammatical clarity to be examined. To the best of my knowledge, the research and writing are those of the candidate except as acknowledged in the Author Attribution Statement. I confirm that the investigations were conducted in accord with the ethics policies and integrity standards of Nanyang Technological University and that the research data are presented honestly and without prejudice.

27/08/2020
. . . .
     Date   Assoc. Prof. Lu Xuehong

Authorship Attribution Statement

This thesis contains material from 2 papers published in the following peer-reviewed journals where I was the co-first author.

Chapter 4 is published as Ma, X. Y. D.; Ang, J. M.; Zhang, Y.; Zeng, Z.; Zhao, C.; Chen, F.; Ng, B. F.; Wan, M. P.; Wong, S.-C.; Li, Z., Highly porous polymer nanofibrous aerogels cross-linked via spontaneous inter-fiber stereocomplexation and their potential for capturing ultrafine airborne particles. *Polymer* **2019,** *179*, 121649. DOI: 10.1016/j.polymer.2019.121649.

The contributions of the co-authors are as follows:
- A/Prof Lu provided the initial project direction and edited the manuscript drafts.
- I prepared the manuscript drafts.
- I co-designed the study with Dr Ang and performed majority of the laboratory work at the School of Materials Science and Engineering. I also analyzed the data. Dr Ang also conducted the differential scanning calorimetry and X-ray diffraction patterns.
- Majority of the microscopy, including sample preparation, was conducted by me in the Facility for Analysis, Characterization, Testing and Simulation. Dr Ang also provided assistance on the microscopy work during the initial stages of the work.
- Dr Zhang and Dr Zeng assisted in the assembling of the filtration testing setup and provided guidance in the interpretation of the filtration results
- Dr Zhao and Dr Chen provided guidance on the preliminary electrospinning optimization work.
- A/Prof Ng and A/Prof Wan provided assistance to improve the filtration testing setup and helped to revise the manuscript drafts.
- Prof Wong, A/Prof He and Dr Li provided guidance and suggestions on the material preparation, and took part in the revision of the manuscript drafts.

Chapter 5 is published as Zeng, Z.; Ma, X. Y. D.; Zhang, Y.; Wang, Z.; Ng, B. F.; Wan, M. P.; Lu, X., Robust Lignin-Based Aerogel Filters: High-Efficiency Capture of Ultrafine Airborne Particulates and the Mechanism. ACS Sustainable Chemistry & Engineering 2019, 7 (7), 6959-6968. DOI: 10.1021/acssuschemeng.8b06567.

The contributions of the co-authors are as follows:

- A/Prof Lu suggested the materials area and edited the manuscript drafts.
- I co-wrote the drafts of the manuscript with Dr Zeng.
- Dr Zeng performed the materials synthesis, collected X-ray diffraction patterns, carried out scanning electron microscopy, TGA and DMA tests, and conducted the respective data evaluation.
- I conducted the FTIR analysis, carried out scanning electron microscopy, performed filtration testing and data evaluation of the filtration performance.
- Dr Zhang and Dr Wang provided guidance and suggestions on the analysis of the filtration test results.
- The manuscript was revised together with Dr. Zeng, A/Prof Ng and A/Prof Wan.

21/08/2020
. . . .
Date   Ma Xiu Yun Daphne

Abstract

In this PhD study, three-dimensional (3D), robust and highly-porous aerogels were employed as air filters because their large internal volume could promote higher removal efficiency of particulate matter (PM), especially for ultrafine particles, while their ultrahigh porosity could facilitate relatively low pressure drops (ΔPs). This synergistic behavior of aerogel filters could effectively address the efficiency-ΔP trade-off of conventional fibrous filters. The aerogels can be categorized as fibrous and non-fibrous, and they can be fabricated via two separate different methods: (1) freeze-drying in a mold or (2) ice-crystals-induced templating method. Apart from the intrinsic structures of the starting materials, the fabrication method adopted would determine the final microstructure of the aerogels. In short, the aerogels prepared in this work would possess either isotropic or aligned porous architectures. Nevertheless, a potential drawback of highly porous 3D aerogels is their relatively poor structural stabilities, which hinders their practical applications as air filters due to the constant compressive force exerted by the airflow in the filtration process. This problem may be overcome by employing chemically- or physically-induced cross-linking to reinforce the aerogel structure. Hence, the structures and morphologies of the aerogels would greatly affect the filtration performance of these aerogel filters. Thus, the aim of this thesis is to prepare highly robust 3D aerogel air filters and investigate the effects of the microstructures on the filtration performance as well as the respective underlying filtration mechanisms of the different as-prepared aerogels.

Three aerogel systems were adopted in this thesis study; (1) PLLA/PDLA blend stereocomplex nanofibers, (2) biomass-based lignin with graphene as reinforcement agent (3) lignin reinforcement agent and cellulose nanofibers. We report that highly-robust aerogels, both fibrous and non-fibrous, with either isotropic or preferably aligned pores are successfully fabricated via different facile cross-linking approaches; spontaneous inter-fiber stereocomplexation-induced cross-linking for

the PLLA/PDLA blend system while thermal treatment was adopted for the other remaining systems. For each system, it is demonstrated that the extent of cross-linking can be easily controlled by adjusting the microstructures and macroscopic shapes of the aerogels, which could influence the filtration performance of the various aerogels. Furthermore, as compared to conventional compact fibrous filters, all the as-prepared aerogel filters demonstrated higher overall filtration efficiency accompanied with a significantly lower ΔP. Through this work, it is believed that the understandings derived can serve as a guideline to facilely fabricate highly-robust and efficient filters for various air filtration applications.

Acknowledgements

First and foremost, I would like to express my deepest gratitude to my supervisor, Associate Professor Lu Xuehong (NTU) for her patience, motivation, and continuous support that she has rendered throughout my PhD journey. Her guidance kept me constantly engaged in my research, including the writing of this thesis. I could not have imagined having a better supervisor and mentor for my PhD study. I would also like to extend my appreciation to my co-supervisor Associate Professor Wan Man Pun (NTU) and mentor Associate Professor Tan Lay Poh (NTU) for their encouragement and insightful comments in every Thesis Advisory Committee meeting. I would also like to thank Assistant Professor Ng Bing Feng (NTU), Associate Professor He Chaobin (NUS), Dr Li Zibiao (IMRE), and Professor Wong Shing-Chung (UA) for sharing their immense knowledge and providing support for my thesis work.

I thank my past and present fellow group members in MSE: Dr Zhao Chenyang, Dr Zeng Zhihui, Dr Zhang Youfang, Dr Ang Jia Ming, Dr Wang Zhe, Dr Che Boyang, Dr Liu Jian, Dr Xu Lulu and Mr Ho Keen Hoe, for the stimulating discussions and for providing many constructive feedback to further develop my ideas. I would like to further extend my sincere appreciation for both Dr Zhang and Dr Xu, who went the extra mile to provide me with additional academic and emotional support. My sincere thanks also goes to Dr Shang Xiaopeng and Mr Ding Shirun from MAE for providing assistance with the loan of air filtration testing equipment. I am also truly grateful to the staffs of MSE and FACTS for sharing their knowledge and technical support on the various laboratory equipment and characterization techniques. I would also like to acknowledge with gratitude, the financial and academic support from the Energy Research Institute @NTU, Interdisciplinary Graduate School.

I am grateful to my close friends, especially Ms Koh Bi Qin, Ms Goh Yan Ngee, Ms Diane Peng, Ms Sylvia Quek, Ms Livia Liew and soon-to-be Dr Sherilyn Chong, all

of whom provided continuous encouragement and humour to keep me sane during challenging times.

Last but not least, I would like to express my utmost gratitude to my family and relatives for their never-ending support and encouragement to take on this PhD journey.

Table of Contents

Table Captions

Figure Captions

Figure 5. 1 Schemes showing the fabrication process of the honeycomb-like aerogels: (a) unidirectional ice-crystal-induced self-assembly of the lignin/GO suspension, (b) lignin-based aerogels prepared by freeze-drying, (c) cross-linked lignin/graphene (A-lignin/G) aerogels obtained by low-temperature annealing. Photographs of (d) lignin/GO aerogel and (e) A-lignin/G aerogel (the inset show that lignin/GO aerogel is crushed and A-lignin/G aerogels is stable when they are supporting a metal over 2000 times heavier). (f) A SEM image showing porous microstructures of A-lignin/G aerogels with honeycomb-like texture in cross sectional plane. Porous microstructures in longitudinal plane of (g) lignin/GO and (h) A-lignin/G aerogels. Cell walls of (i) lignin/GO and (j) A-lignin/G aerogels. (k) Compressive curves of the aerogels prepared from suspensions of various lignin

Abbreviations

2D	Two-dimensional
3D	Three-dimensional
A-CNFA	Annealed cellulose nanofibrous aerogel
A-CLNFA	Annealed cellulose-lignin nanofibrous aerogel
AFNFA	Aligned fibers nanofibrous aerogel
A-Lignin	Annealed lignin
A-Lignin/G	Annealed lignin and reduced graphene-oxide
ATR	Attenuated reflectance
C	Catechin
CA	Cellulose acetate
CPC	Condensation particle counter
C/L	Cellulose/lignin
CNFA	Cellulose nanofibrous aerogel
CLNFA	Cellulose-lignin nanofibrous aerogel
DSC	Differential scanning calorimetry
DCM	Dichloromethane
DMF	N,N-dimethylformamide
DEHS	Diethylhexyl sebacate
DMA	Dynamic mechanical analyzer
DI	Deionized
DTG	Derivative thermogravimetry
EC	Epicatechin
ECG	Epicatechin gallate
EGC	Epigallocatechin
EGCG	Epigallocatechin gallate
FESEM	Field emission scanning electron microscopy
FTIR	Fourier-Transform Infrared Spectroscopy

GO	Graphene-oxide
GCG	Gallocatechin gallate
HEPA	High-efficiency particulate arrestance
iNFA	Isotropic nanofibrous aerogel
IPA	Isopropyl alcohol
MPPS	Most penetrating particle size
M_w	Molecular weight
NFM	Nanofibrous membrane/mat
NFA	Nanofibrous aerogel
OPS	Optical particle sizer
PP	Polypropylene
PLA	Poly(lactic) acid
PI	Polyimide
Pul/PVA	Pullulan/poly(vinyl alcohol)
PAHs	Polycyclic aromatic hydrocarbons
PDLA	Poly-D-lactic acid
PLLA	Poly-L-lactic acid
PM	Particulate matter or Mass concentration
$PM_{2.5}$	Particles with sizes < 2.5 µm
$PM_{0.1}$	Particles with sizes < 0.1 µm
PN	Number concentration
QF	Quality factor
RH	Relative humidity
RDMA	Radial differential mobility analyzer
SC	Stereocomplex
SPMS	Scanning mobility particle sizer
SEM	Scanning electron microscopy
SEI	Secondary electron imaging
SGTL	Spent green tea leaves

T_m	Melting temperature
TBAC	Tetrabutylammonium chloride
TGA	Thermogravimetric analysis
UV	Ultraviolet
VOCs	Volatile organic compounds
WHO	World Health Organization
XRD	X-ray diffraction
ΔP	Pressure drop

Chapter 1

Introduction

1.1 Background and Problem Statement

Air pollution poses as a severe threat, with the atmospheric release of particulate matter (PM) comprising organic and inorganic compounds with trace amounts of metals, which can be detrimental to human health [1]. Studies have revealed that the exposure to PM, consisting of large amounts of micrometer- and nanometer-sized particles, can give rise to adverse health problems such as respiratory and cardiovascular diseases [2]. Current filtration technologies are targeted at removing micron- and submicron-sized particles. Studies have, however, shown that ultrafine particles, i.e., the ones with sizes smaller than 0.1 μm ($PM_{0.1}$) have higher reactivity due to their smaller sizes, which can penetrate the respiratory system much more easily and enter the blood stream [2-3]. Hence, strategies to remove these smaller particulate matters also need to be formulated in order to create a healthier living environment.

Considerable efforts have been focused on the development of air filtration technologies that are economic and energy efficient, especially in the area of conventional fibrous mats or membranes due to low-cost, large specific surface area for adsorption and ease of fabrication [4-7]. Air filtration via fibrous media is governed by four main mechanisms known as sieving, inertial impaction, interception and diffusion. The first three mechanisms are, however, not effective for removal of ultrafine particles. Capture of ultrafine particles mainly relies on diffusion, i.e., Brownian motion of these tiny particles can cause them to collide and adhere onto fibers if their residence time in the fibrous medium is long enough. Nevertheless, the tradeoff between filtration efficiency and pressure drop (ΔP) remains a challenge; high efficiency can be achieved by increasing fiber packing density but at the same time leads to a surge in ΔP, which increases energy consumption. Currently,

commercial high-efficiency particulate arrestance (HEPA) filters are able to achieve high removal efficiency of 99.97% for particles with sizes down to 0.3 μm but their ΔP is still considerably high.

Various approaches have been reported for improving the filtration efficiency for ultrafine particles. In particular, much focus have been placed on the development of nanofibrous membranes/mats (NFMs) due to their much larger specific surface areas that could increase diffusion and interception capture[4, 8-10]. Theoretical studies have also shown that nanofibers display significant slip flow phenomenon, which may lower airflow resistance to some extent, resulting in a smaller pressure drop across the filter[11-14]. However, in NFMs, the nanofibers are packed in roughly parallel planes. Thus, the high efficiency removal of ultrafine particles is still accompanied with a surge in air resistance across the filters due to their high fiber packing densities, which is not energy-efficient for filtration applications. Owing to their much smaller pores, NFMs typically give a much larger pressure drop than their microfiber counterparts[15-16]. Previous studies also suggest that the addition of a nanofibrous layer onto microfibrous filters significantly reduce the most penetrating particle sizes (MPPS) of the microfibrous filters[16-19]. However, the improved efficiency is often accompanied with a surge in air resistance and many challenges remain to strike a good balance between filtration efficiency and pressure drop. Moreover, when in use, the filtration area of these dense and compact filters are rapidly deposited with particles, followed by cake formation on the filter surface, which may greatly alter the filter performance; ΔP will increase and filtration efficiency is often reduced, limiting the filter service life [20-22]. Therefore, besides addressing the trade-off between filtration efficiency and ΔP, there is an urgent need to develop a new kind of filter with anti-clogging features that could make the filters more durable.

More recently, three-dimensional (3D) aerogels, endowed with ultrahigh porosity and large volumes of voids, have also been employed as air filters. Unlike conventional fibrous filters, the unique features of these 3D aerogels such as

ultrahigh porosity exhibit potential to achieve greater capture efficiency of ultrafine particles that undergo Brownian motion (longer residence time), while at the same time, the ultralow material packing density could reduce the drag force. Additionally, these aerogel filters possess a larger internal surface where particle adsorption is dominated by depth filtration rather than cake filtration [11, 20, 23], making the filters more clog-resistant. Notably, in the field of 3D aerogels, nanofibrous aerogels (NFAs), which consist of loosely packed nanofibers in random orientations, have emerged as a popular choice due to their high specific surface area, low fiber packing density, slip flow effect and ease of fabrication[24-26]. Furthermore, simulation studies of NFAs as deep-bed filters also revealed the synergistic effects of ultrahigh porosity and ultralow density of NFAs can promote much higher dust loadings NFMs without compromising the filter performance, which extends the service life of these three-dimensional filters [20]. However, the poor structural stabilities of these highly porous aerogels restrict their application as air filters due to the constant compressive force exerted by the air flow, which may be overcome by introducing chemical and/or physical cross-links to improve the robustness of NFAs[24, 27-28]. Nevertheless, conventional choices of polymeric nanofibers and/or the cross-linking agents employed are typically made of petrochemicals or synthetic chemicals generated from non-renewable precursors that are harmful to the environment, which hampers their practical applications. Therefore, the need to identify a more economically viable and environmentally benign cross-linking agent that could make 3D NFA filters more robust or even reusable.

Besides NFAs, it was reported that 3D non-fibrous aerogels with aligned pore channels also displayed promising results as filter materials for the removal of PM [29]. It was reported that the aligned micrometer-sized hollow channels could help to significantly reduce the air resistance across the aerogel filter, which is dissimilar to that of fibrous filters made of randomly entangled fibers. Moreover, the hollow through-pores may render the aerogel with clog-resistant properties. In addition, recent works on cross-flow filtration has shown that aligned channels with open ends could result in a pressure drop of only one-fifth of that of conventional filtration

mode [30-31]. Simulation studies also suggested that cross-flow filtration removed particles based on size-dependent trajectory segregation, where smaller particles are deposited on the filter media while the larger ones travel continuously along the air flow [32]. Although these unconventional non-fibrous aerogels have been explored as alternatives to fibrous filters, the filtration mechanism of these materials have not yet been investigated and the starting materials used stem from non-renewable resources. Thus, besides addressing the issue of material renewability, it is crucial to conduct a systematic study on the filtration mechanism of aerogels with aligned pore channels to further assess the potential of these materials in the field of air filtration.

1.2 Hypotheses

To address the aforementioned issues, three new designs have been put forward in this thesis work, which will be elaborated in the subsections below. To fabricate eco-friendly aerogel filters, biodegradable polymeric electrospun nanofibers produced from renewable resources and biomass-based materials have been chosen as the starting materials to fabricate the aerogels. Freeze-drying method was adopted because this technique could allow water to be sublimated from the frozen aerogel without entering the liquid state, which could effectively avoid the collapse of the 3D structure. In order to realize cross-linking methods that are environmentally-benign, spontaneous physical cross-linking methods via self-assembly (NFAs), and low-temperature annealing (non-fibrous aerogels) have been adopted to endow the aerogel-based filters with robust mechanical properties, while at the same time, maintaining a high yield of product. Furthermore, the loosely packed and oriented structure of the 3D aerogel filters can help to enhance the diffusion capture of ultrafine particles via depth filtration, while simultaneously maintain a low air resistance across the filters.

1.2.1 Design 1: Robust NFA Filter and the Concept of 3D Filtration

Polylactic acid (PLA), a polymer derived from renewable resources, is capable of forming a polymer stereocomplex that is a stable composite of two stereoregular polymers with complementary helical conformations, which interlock each other by stereoselective interactions [33-34]. Therefore, in this work, we used a stereocomplexation approach to spontaneously induce inter-fiber agglutination in highly porous 3D nanofibrous aerogels (NFAs) formed by poly-L-lactic acid (PLLA)/poly-D-lactic acid (PDLA) blend nanofibers without thermal or other form of stimuli. Different from some reported works [35-36], PLLA/PDLA-SC inter-fiber agglutination points were spontaneously formed in the NFA fabrication process, which, combined with the favorable mechanical properties of the PLLA/PDLA blend fibers [37-39], could enhance the compression resistance of the highly porous NFAs and prevent them from collapsing in applications. We also hypothesized that the extent of inter-fiber stereocomplexation may be related to the number of free chain ends on the nanofiber surface because with free ends, chain segments on a fiber surface could adjust their conformations more easily to form stereocomplex with appropriate chain segments on a neighboring fiber surface. Since lower-molecular-weight polymer (shorter chains) has more chain ends per unit mass than the corresponding higher-molecular-weight polymer, this implies that the extent of inter-fiber stereocomplexation may be influenced by the molecular weights of the two stereoisomers. To demonstrate the usefulness of our 3D filter, a highly porous PLLA/PDLA-SC NFA was combined with a HEPA filter to assess the filtration performance of ultrafine particles, where the loosely packed structure of the PLLA/PDLA-SC NFA could help to enhance the filtration efficiency of ultrafine particles accompanied by a small increase in ΔP. The scheme of the design is shown in Figure 1.1. In chapter 4, the related verification results will be presented and discussed.
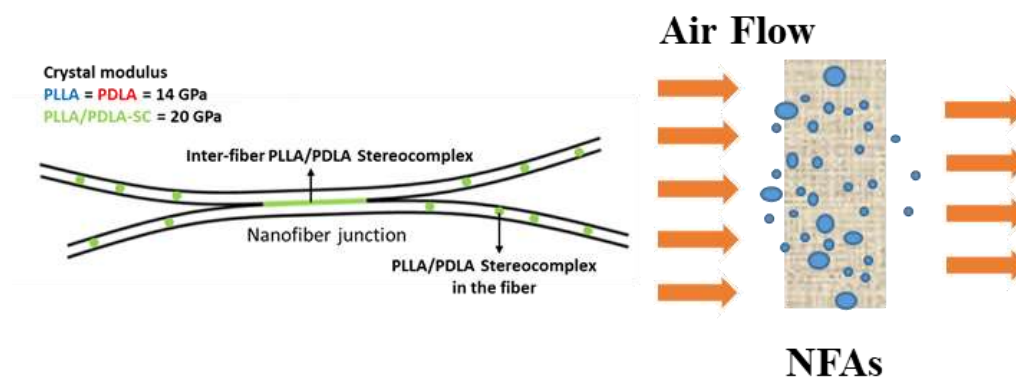
Figure 1.1 The schematic illustrations of the spontaneous inter-fiber cross-linking and the particle residence of NFA filters.

1.2.2 Design 2: Non-Fibrous Aerogel Filter with Aligned Solid Channels and the Mechanism

Recently, besides NFA filters, non-fibrous honeycomb-like aerogels have also emerged as attractive alternatives to replace conventional fibrous filters [29]. However, the filtration mechanism of non-fibrous aerogels was not explored, which restricts the practical applications of these materials. Thus, in the new design of the study, the issues of material renewability and a systematic study of the filtration mechanism are addressed simultaneously. Specifically, we design a new type of lignin-based wood-like aerogel filters composed of aligned micrometer-sized pores, prepared via a facile unidirectional ice-crystal-induced self-assembly from an aqueous solution. Furthermore, low-temperature annealing and a very small amount of graphene was added to reinforce the mechanical stiffness, thermal stability and humidity/water resistance of the aerogels. Different from typical NFAs, the high porosity and large internal volume could enhance the diffusion capture of ultrafine particles via depth filtration while adsorption along the aligned hollow pores will not disturb the air flow significantly, rendering the filters more clog-resistant. Moreover, the abundant functional groups retained from lignin could improve PM adsorption via favourable dipole-dipole interations. The scheme of the design is shown in Figure 1.2. The related verification results will be presented and discussed in Chapter 5.
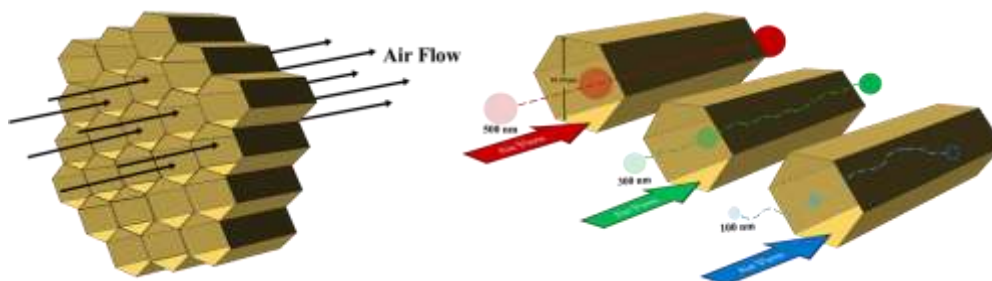
Figure 1.2 The schematic illustrations of the aligned pore structure of the lignin-based aerogel and the respective particle flow regime.

1.2.3 Design 3: Biodegradable NFA Filters with Aligned Fibrous Channels

Lately, a new kind of 3D NFA filter have been reported that consists of aligned nanofibrous channels prepared via unidirectional freezing and thermal cross-linking, which exhibited much lower ΔP while maintaining a high filtration efficiency. Compared with other reinforcement methods, thermal cross-linking has emerged as a more facile and cheaper method. However, by adopting this method, many researchers have also reported annealing-induced shrinkage of the porous materials, especially at relatively high heat treatment temperatures ($> 500^{\circ}C$), which could induce pore size reduction or even pore structural change of the porous materials [40-42]. To minimize such unfavourable morphological change, a plausible approach is to introduce hyperbranched macromolecular cross-linking agents into the system, which could act as spacers between the fibers to prevent highly porous 3D NFAs from collapsing into much denser structures. In addition, since the contacting area between adjacent nanofibers are expected to be small in general, the contact of hyperbranched macromolecules with nanofibers may also boost cross-linking reactions. Nevertheless, so far the cross-linking agents employed are typically linear polymers [43-46]. Therefore, in this work, we employed lignin (also a hyperbranched natural macromolecule) as an effective cross-linker for fabrication of lignin/cellulose-based 3D NFAs with preferably aligned pores and hierarchical porous structures. Unlike recently reported cellulose-based aerogels [47-50], by subjecting the as-prepared lignin/cellulose NFAs to low-temperature annealing, the

material shrinkage could be largely minimized, and hence the initial morphology of the NFAs could be largely retained after the annealing, minimizing the negative effect of thermal annealing on porosity and pore structures, which are essential for high filtration efficiency and low ΔP. The scheme of the design is shown in Figure 1.3. The related verification results will be presented and discussed in Chapter 6.
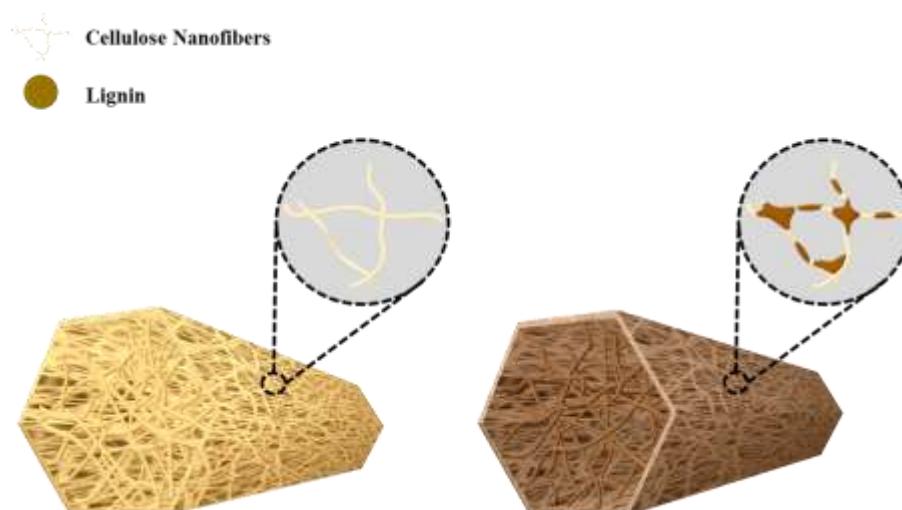
Figure 1.3 The schematic illustrations of the inter-fiber cross-linking with and without lignin.

1.3 Objectives

The PhD work in this thesis is focused on the design and fabrication of robust 3D aerogel filters that are capable of achieving high filtration efficiency of ultrafine particles with low air resistance and to investigate their respective filtration mechanism. The objectives include the following:

1. The first objective is to verify the spontaneous inter-fiber stereocomplexation within the NFA, correlate the extent of cross-linking to the molecular weight (M_w) of the polymer, as well as demonstrate the concept of 3D air filtration.

2. The second objective is to fabricate a robust lignin-based aerogels with aligned micrometer-sized channels, demonstrate that the hollow pores channels can promote high filtration efficiency of ultrafine particles via diffusion capture while maintaining a low ΔP, and investigate the underlying filtration mechanism of non-fibrous aerogel filter.

3. The third objective is to verify that hyperbranched macromolecular cross-linking agents can give rise to a larger extent of cross-linking compared to that of inter-fiber cross-linking, demonstrate that lower ΔP can be achieved after thermal annealing and investigate the respective filtration mechanism.

1.4 Dissertation Overview

In *Chapter 1*, the background on air pollution and its adverse health impacts are briefly introduced. The current issues of conventional two-dimensional (2D) fibrous filters used to tackle air pollution problems are also discussed. The concept of 3D air filtration is also presented as well as the potential applications of aerogel as 3D air filters. Motivation leading up to the study is also addressed, followed by the proposed hypotheses and the detailed objectives of this study. Subsequently, the major findings and outcomes derived from this study are highlighted.

In *Chapter 2*, the key performance parameters of air filters are provided with emphasis on the filtration performance and operational costs. The effectiveness of current air filtration technologies are discussed, with the advantages of conventional 2D fibrous filters being highlighted. The filtration mechanism of fibrous media is explained, followed by the discussion on the developments and drawbacks of micro- and nanofibrous filters. The detailed concept of 3D air filtration is elaborated together with the latest advancement in 3D aerogel-based air filters being reviewed. Finally, the direction of this study is presented in an attempt to bridge the research gap.

In *Chapter 3*, the rationale on material selection for the three designs of this thesis study is discussed and elucidated. Reasons for choosing electrospinning and unidirectional freezing as the main NFA fabrication methods are provided and rationalized. For the filtration test, the motivation for the selection of the model haze particles is provided and the underlying principles of the particle detection techniques are explained. Finally, the theories and working principles of the material characterization techniques carried out in this study are elaborated and justified as to why they are necessary for the study.

In *Chapter 4*, the spontaneous cross-linking phenomenon of PLLA/PDLA blend electrospun nanofibers is reported, and the morphological structures and the fiber agglutination process are revealed. It is found with SEM that the extent of cross-linking and the molecular weights of the polymer are correlated. NFA reinforcement is verified via tensile and compression tests. Two types of model haze particles are used to evaluate the filtration performance of the NFA filters and the results obtained verified the concept of 3D air filtration.

In *Chapter 5*, the fabrication of robust graphene-oxide-reinforced lignin aerogels with unidirectional porous architectures is reported, and the morphology of the hierarchical pores are revealed. After subjected to annealing, the changes in mechanical properties, morphology and chemical compositions are discussed and justified, with emphasis on the benefits of the addition of a small amount of GO. Subsequently, the filtration performance of the aerogel filters are evaluated using the model haze particles. Along with studies done in the literature, the results obtained are used to elucidate the possible filtration mechanism.

In *Chapter 6*, the fabrication of robust lignin-assisted cross-linked electrospun cellulose-based NFAs with preferably aligned pores and hierarchical porous structure is reported. The positive influence of hyperbranched macromolecular lignin as cross-linking agents on the annealing-induced-shrinkage and mechanical properties are discussed and verified. The possible cross-linking mechanisms that

occurred during annealing are deduced from TGA-IR results in conjunction with studies reported in the literature. For the filtration test, DEHS model haze particle was used to evaluate the filtration performance of the NFA filter and the results obtained are used to derive the possible filtration mechanism.

In *Chapter 7*, all the findings in Chapter 4, 5 and 6 are drawn together. The conclusions of these chapters are summarized and associated back to the initial hypotheses and objectives of the thesis study. The significant findings and novel outcomes of this study are emphasized and their potential implications on future work are discussed. Some preliminary studies that lack sufficient data to be written into a complete chapter are also briefly covered. Finally, some suggestions on the direction for future research are proposed.

References

1.   See, S. W.; Balasubramanian, R.; Wang, W., A study of the physical, chemical, and optical properties of ambient aerosol particles in Southeast Asia during hazy and nonhazy days. *Journal of Geophysical Research: Atmospheres* **2006,** *111* (D10), n/a-n/a.

2.   Zhang, Q.; Jiang, X.; Tong, D.; Davis, S. J.; Zhao, H.; Geng, G.; Feng, T.; Zheng, B.; Lu, Z.; Streets, D. G., Transboundary health impacts of transported global air pollution and international trade. *Nature* **2017,** *543* (7647), 705.

3.   Ostro, B.; Hu, J.; Goldberg, D.; Reynolds, P.; Hertz, A.; Bernstein, L.; Kleeman, M. J., Associations of mortality with long-term exposures to fine and ultrafine particles, species and sources: results from the California Teachers Study Cohort. *Environmental health perspectives* **2015,** *123* (6), 549.

4.   Liu, C.; Hsu, P. C.; Lee, H. W.; Ye, M.; Zheng, G.; Liu, N.; Li, W.; Cui, Y., Transparent air filter for high-efficiency PM2.5 capture. *Nat Commun* **2015,** *6*, 6205.

5.   Wang, C.; Wu, S.; Jian, M.; Xie, J.; Xu, L.; Yang, X.; Zheng, Q.; Zhang, Y., Silk nanofibers as high efficient and lightweight air filter. *Nano Research* **2016,** *9* (9), 2590-2597.

6.   Li, J.; Zhang, D.; Yang, T.; Yang, S.; Yang, X.; Zhu, H., Nanofibrous membrane of graphene oxide-in-polyacrylonitrile composite with low filtration resistance for the effective capture of PM2. 5. *Journal of membrane science* **2018,** *551*, 85-92.

7.   Huang, X.; Jiao, T.; Liu, Q.; Zhang, L.; Zhou, J.; Li, B.; Peng, Q., Hierarchical electrospun nanofibers treated by solvent vapor annealing as air filtration mat for high-efficiency PM2. 5 capture. *Science China Materials* **2019,** *62* (3), 423-436.

8.   Zhang, Y.; Yuan, S.; Feng, X.; Li, H.; Zhou, J.; Wang, B., Preparation of nanofibrous metal–organic framework filters for efficient air pollution control. *Journal of the American Chemical Society* **2016,** *138* (18), 5785-5788.

9.   Gu, G. Q.; Han, C. B.; Lu, C. X.; He, C.; Jiang, T.; Gao, Z. L.; Li, C. J.; Wang, Z. L., Triboelectric nanogenerator enhanced nanofiber air filters for efficient particulate matter removal. *ACS nano* **2017,** *11* (6), 6211-6217.

10.   Han, K. S.; Lee, S.; Kim, M.; Park, P.; Lee, M. H.; Nah, J., Electrically Activated Ultrathin PVDF-TrFE Air Filter for High-Efficiency PM1. 0 Filtration. *Advanced Functional Materials* **2019**, 1903633.

11.   Sambaer, W.; Zatloukal, M.; Kimmer, D., 3D modeling of filtration process via polyurethane nanofiber based nonwoven filters prepared by electrospinning process. *Chemical Engineering Science* **2011,** *66* (4), 613-623.

12.   Graham, K.; Ouyang, M.; Raether, T.; Grafe, T.; McDonald, B.; Knauf, P. In *Polymeric nanofibers in air filtration applications*, Fifteenth Annual Technical Conference & Expo of the American Filtration & Separations Society, Galveston, Texas, 2002; pp 9-12.

13.   Zhao, X.; Wang, S.; Yin, X.; Yu, J.; Ding, B., Slip-Effect Functional Air Filter for Efficient Purification of PM 2.5. *Scientific reports* **2016,** *6*, 35472.

14.   Hung, C.-H.; Leung, W. W.-F., Filtration of nano-aerosol using nanofiber filter under low Peclet number and transitional flow regime. *Separation and purification technology* **2011,** *79* (1), 34-42.

15.   Barhate, R. S.; Ramakrishna, S., Nanofibrous filtering media: Filtration problems and solutions from tiny materials. *Journal of Membrane Science* **2007,** *296* (1–2), 1-8.

16.   Leung, W. W.-F.; Hung, C.-H.; Yuen, P.-T., Effect of face velocity, nanofiber packing density and thickness on filtration performance of filters with nanofibers coated on a substrate. *Separation and purification technology* **2010,** *71* (1), 30-37.

17.   Podgorski, A.; Bałazy, A.; Gradoń, L., Application of nanofibers to improve the filtration efficiency of the most penetrating aerosol particles in fibrous filters. *Chemical Engineering Science* **2006,** *61* (20), 6804-6815.

18.   Tang, M.; Chen, S.-C.; Chang, D.-Q.; Xie, X.; Sun, J.; Pui, D. Y., Filtration efficiency and loading characteristics of PM2. 5 through composite filter media consisting of commercial HVAC electret media and nanofiber layer. *Separation and Purification Technology* **2018,** *198*, 137-145.

19.   Wang, Z.; Pan, Z., Preparation of hierarchical structured nano-sized/porous poly (lactic acid) composite fibrous membranes for air filtration. *Applied Surface Science* **2015,** *356*, 1168-1179.

20.   Deuber, F.; Mousavi, S.; Federer, L.; Hofer, M.; Adlhart, C., Exploration of ultralight nanofiber aerogels as particle filters: capacity and efficiency. *ACS applied materials & interfaces* **2018,** *10* (10), 9069-9076.

21.   Joubert, A.; Laborde, J.-C.; Bouilloux, L.; Chazelet, S.; Thomas, D., Modelling the pressure drop across HEPA filters during cake filtration in the presence of humidity. *Chemical engineering journal* **2011,** *166* (2), 616-623.

22.   Li, P.; Wang, C.; Zhang, Y.; Wei, F., Air Filtration in the Free Molecular Flow Regime: A Review of High-Efficiency Particulate Air Filters Based on Carbon Nanotubes. *Small* **2014,** *10* (22), 4543-4561.

23.   Sambaer, W.; Zatloukal, M.; Kimmer, D., 3D air filtration modeling for nanofiber based filters in the ultrafine particle size range. *Chemical Engineering Science* **2012,** *82* (Supplement C), 299-311.

24.   Qian, Z.; Wang, Z.; Chen, Y.; Tong, S.; Ge, M.; Zhao, N.; Xu, J., Superelastic and ultralight polyimide aerogels as thermal insulators and particulate air filters. *Journal of Materials Chemistry A* **2018,** *6* (3), 828-832.

25.   Nemoto, J.; Saito, T.; Isogai, A., Simple freeze-drying procedure for producing nanocellulose aerogel-containing, high-performance air filters. *ACS applied materials & interfaces* **2015,** *7* (35), 19809-19815.

26.   Zhang, Y.-G.; Zhu, Y.-J.; Xiong, Z.-C.; Wu, J.; Chen, F., Bioinspired Ultralight Inorganic Aerogel for Highly Efficient Air Filtration and Oil–Water Separation. *ACS applied materials & interfaces* **2018,** *10* (15), 13019-13027.

27.   Feng, J.; Nguyen, S. T.; Fan, Z.; Duong, H. M., Advanced fabrication and oil absorption properties of super-hydrophobic recycled cellulose aerogels. *Chemical Engineering Journal* **2015,** *270*, 168-175.

28.   Si, Y.; Fu, Q.; Wang, X.; Zhu, J.; Yu, J.; Sun, G.; Ding, B., Superelastic and superhydrophobic nanofiber-assembled cellular aerogels for effective separation of oil/water emulsions. *ACS nano* **2015,** *9* (4), 3791-3799.

29.   Zhang, S.; Sun, J.; Hu, D.; Xiao, C.; Zhuo, Q.; Wang, J.; Qin, C.; Dai, L., Large-sized graphene oxide/modified tourmaline nanoparticle aerogel with stable honeycomb-like structure for high-efficiency PM 2.5 capture. *Journal of Materials Chemistry A* **2018,** *6* (33), 16139-16148.

30.   Wang, L.-Y.; Liya, E. Y.; Lai, J.-Y.; Chung, T.-S., Developing ultra-high gas permeance PVDF hollow fibers for air filtration applications. *Separation and Purification Technology* **2018,** *205*, 184-195.

31.   Wang, L.-Y.; Yong, W. F.; Liya, E. Y.; Chung, T.-S., Design of high efficiency PVDF-PEG hollow fibers for air filtration of ultrafine particles. *Journal of Membrane Science* **2017,** *535*, 342-349.

32.   Sibanda, V.; Greenwood, R.; Seville, J.; Ding, Y.; Iyuke, S., Predicting particle segregation in cross-flow gas filtration. *Powder Technology* **2010,** *203* (3), 419-427.

33.   Gupta, B.; Revagade, N.; Hilborn, J., Poly (lactic acid) fiber: An overview. *Progress in polymer science* **2007,** *32* (4), 455-482.

34.   Castro-Aguirre, E.; Iñiguez-Franco, F.; Samsudin, H.; Fang, X.; Auras, R., Poly (lactic acid)—Mass production, processing, industrial applications, and end of life. *Advanced drug delivery reviews* **2016,** *107*, 333-366.

35.   Kurokawa, N.; Hotta, A., Thermomechanical properties of highly transparent self-reinforced polylactide composites with electrospun stereocomplex polylactide nanofibers. *Polymer* **2018**.

36.   Jing, Y.; Zhang, L.; Huang, R.; Bai, D.; Bai, H.; Zhang, Q.; Fu, Q., Ultrahigh-performance electrospun polylactide membranes with excellent oil/water separation ability via interfacial stereocomplex crystallization. *Journal of Materials Chemistry A* **2017,** *5* (37), 19729-19737.

37.   Pan, G.; Xu, H.; Mu, B.; Ma, B.; Yang, Y., A clean approach for potential continuous mass production of high-molecular-weight polylactide fibers with fully stereo-complexed crystallites. *Journal of Cleaner Production* **2018,** *176*, 151-158.

38.   Pan, G.; Xu, H.; Mu, B.; Ma, B.; Yang, J.; Yang, Y., Complete stereo-complexation of enantiomeric polylactides for scalable continuous production. *Chemical Engineering Journal* **2017,** *328*, 759-767.

39.   Saini, P.; Arora, M.; Kumar, M. R., Poly (lactic acid) blends in biomedical applications. *Advanced drug delivery reviews* **2016,** *107*, 47-59.

40.   Li, L.; Hu, T.; Sun, H.; Zhang, J.; Wang, A., Pressure-sensitive and conductive carbon aerogels from poplars catkins for selective oil absorption and oil/water separation. *ACS applied materials & interfaces* **2017,** *9* (21), 18001-18007.

41.   Meador, M. A. B.; Alemán, C. R.; Hanson, K.; Ramirez, N.; Vivod, S. L.; Wilmoth, N.; McCorkle, L., Polyimide aerogels with amide cross-links: a low cost alternative for mechanically strong polymer aerogels. *ACS applied materials & interfaces* **2015,** *7* (2), 1240-1249.

42.   Pakula, T.; Trznadel, M., Thermally stimulated shrinkage forces in oriented polymers: 1. Temperature dependence. *Polymer* **1985,** *26* (7), 1011-1018.

43.   Deuber, F.; Mousavi, S.; Federer, L.; Adlhart, C., Amphiphilic nanofiber-based aerogels for selective liquid absorption from electrospun biopolymers. *Advanced Materials Interfaces* **2017,** *4* (12), 1700065.

44.   Fan, J. B.; Song, Y.; Wang, S.; Meng, J.; Yang, G.; Guo, X.; Feng, L.; Jiang, L., Directly coating hydrogel on filter paper for effective oil–water separation in highly acidic, alkaline, and salty environment. *Advanced Functional Materials* **2015,** *25* (33), 5368-5375.

45.   Wang, W.; Fang, Y.; Ni, X.; Wu, K.; Wang, Y.; Jiang, F.; Riffat, S. B., Fabrication and characterization of a novel konjac glucomannan-based air filtration aerogels strengthened by wheat straw and okara. *Carbohydrate polymers* **2019,** *224*, 115129.

46.   Zhou, L.; Zhai, Y.-M.; Yang, M.-B.; Yang, W., Flexible and Tough Cellulose Nanocrystal/Polycaprolactone Hybrid Aerogel Based on the Strategy of Macromolecule Cross-Linking via Click Chemistry. *ACS Sustainable Chemistry & Engineering* **2019,** *7* (18), 15617-15627.

47.   Li, X.; Lu, X.; Yang, J.; Ju, Z.; Kang, Y.; Xu, J.; Zhang, S., A facile ionic liquid approach to prepare cellulose-rich aerogels directly from corn stalks. *Green Chemistry* **2019**.

48.   Song, J.; Chen, C.; Yang, Z.; Kuang, Y.; Li, T.; Li, Y.; Huang, H.; Kierzewski, I.; Liu, B.; He, S., Highly compressible, anisotropic aerogel with aligned cellulose nanofibers. *ACS nano* **2017,** *12* (1), 140-147.

49.   Zhu, L.; Wang, Y.; Wang, Y.; You, L.; Shen, X.; Li, S., An environmentally friendly carbon aerogels derived from waste pomelo peels for the removal of organic pollutants/oils. *Microporous and Mesoporous Materials* **2017,** *241*, 285-292.

50.   Fan, P.; Yuan, Y.; Ren, J.; Yuan, B.; He, Q.; Xia, G.; Chen, F.; Song, R., Facile and green fabrication of cellulosed based aerogels for lampblack filtration from waste newspaper. *Carbohydrate polymers* **2017,** *162*, 108-114.

Chapter 2

Literature Review

In this chapter, the adverse health impacts of airborne particulate matter on human health is firstly discussed, and the severe consequences of exposure to ultrafine particles is also highlighted. The key performance parameters for air filters are then presented, and current filtration technologies are also reviewed based on these key parameters, with the attention drawn towards two dimensional (2D) fibrous filters. To highlight the superior filtration performance of fibrous filters, the filtration mechanism that governs fibrous media is also discussed, with emphasis on the main capture mechanism for ultrafine particles. Subsequently, a review on conventional 2D microfibrous filters and recent research on nanofibrous mats are presented, followed by pointing out the efficiency-pressure drop trade-off as the main issue of such fibrous filters with 2D compact structures. The concept of 3D air filtration is then introduced, and how 3D aerogel filters (fibrous and non-fibrous) can address the trade-off problem is also explained. A review on the aerogel air filters reported in the literature is also provided. Based on the literatures being reviewed, it is found that the issues of mechanical robustness, material renewability and production costs need to be addressed in order for these aerogels to be potentially explored as 3D air filters.

2.1 Key Performance Parameters of Air Filters

The main purpose of air filters is to regulate the airborne particulate concentrations and maintain high air quality of the environment. Thus, it is important to understand the size compositions and surface chemistries of particulate matter (PM), to effectively develop filters that are capable of obtaining high filtration efficiency. In fact, studies have shown that ultrafine particles (diameter < 0.1 µm) contribute significantly to the number concentration of airborne pollutants, generated mainly from industrial, agricultural and domestic emissions [1-4]. However, most research on air filtration are geared towards the remediation of particles in the size range of PM_{10} (diameter < 10 µm) and $PM_{2.5}$ (diameter < 2.5 µm). Furthermore, conventional PM measurement methods are focused on the particle mass concentration and do not precisely reflect the actual particle numbers of the various particle sizes, which undermines the effects of ultrafine particles [3]. Moreover, studies have also revealed that the reactivity of particles increases with decreasing size; ultrafine particles are more likely to possess stronger biological interactions within the human respiratory tract, giving rise to adverse health impacts such as cardiovascular and respiratory diseases [5-6]. Additionally, according to the World Health Organization (WHO) in 2016, 91% of the global population are still residing in environments where the air quality exceeds the WHO air quality guidelines, resulting in at least 8 million deaths annually. Therefore, besides placing emphasis on PM_{10} and $PM_{2.5}$, current filtration technologies should also be engineered towards the efficient removal of ultrafine particles, in order to create a healthier living environment.

Current filtration technologies can be tailored for the removal of ultrafine particles by optimizing the key performance parameters depending upon the applications and requirements. Air filters are mainly categorized as physical and non-physical air filters [7]. Physical air filters are the most common type of air filters, which can clean the air by acting as physical barriers to obstruct the movement of particles. Else, other types of air filters would be classified under non-physical filtration methods. Generally, the filtration performance is governed by the filtration efficiency,

pressure drop (ΔP) and quality factor (QF). Filtration efficiency is a measurement of the filter's ability to remove particles from the air stream. In fact, the removal efficiency varies with different particle sizes; larger particles tend to be trapped much more easily due to their larger size and inertia, while smaller particles are more difficult to be retained due to their much smaller size and erratic behavior. Filters with different filtration efficiencies serve different purposes; lower efficiency filters can be used to remove larger particles such as the removal of fine dust (diameter ≥ 1 μm) in circulating filters of air conditioning systems while higher efficiency filters can be used as end filters in hospitals, pharmaceutical laboratories or food industry where stricter air quality is preferred [7-8]. Essentially, the operational cost increases rapidly with cleanliness. On the other hand, ΔP is a measure of an air filter's resistance when air is moved through it, and this impediment of the air flow is directly related to the energy consumption; the higher the pressure drop, the more energy is required to drive the air across the air filter. Usually in the case of physical air filters, there exists a trade-off between efficiency and ΔP [8]; high efficiency is accompanied with a surge in ΔP due to higher material packing density. Therefore, the quality factor (QF) comes into place, taking both the efficiency and ΔP into consideration, which gives an overview of the filtration performance. QF is defined as –ln (E)/ΔP, where E is the filtration efficiency and ΔP is the pressure drop. Higher QF values indicate better filtration performance of the filter. Meanwhile, for easier maintenance of the air filters, other key performance parameters such as lifetime, loading capacity, mechanical property, and thermal stability would also need to be considered, depending on the type of filtration technology. A filter's lifetime refers to the effective service period before the filter is replaced with a new one, which is one of the main contributors to the operating cost. The loading capacity of a filter determines how much PM the filter can contain while maintaining its specified efficiency or within its rated ΔP. At large, the loading capacity determines the operating lifetime of a filter. The mechanical property is a crucial factor that determines the reusability of an air filter; robust filters can undergo washing to regenerate a clean filter. In addition, for physical filters, the robustness of a filter is also important to withstand the compressive forces of the air flow. The thermal

stability is important to prevent the decomposition of material at high temperature applications such as exhaust systems of buildings and vehicles [9-10]. On top of the key parameters mentions, the issue of material renewability and biodegradability is also important to reduce the carbon footprint of humans. Therefore, in order to fabricate a multifunctional filter that is both highly efficient and sustainable for the removal of ultrafine particles, the aforementioned key parameters should be addressed.

2.2 Air Filtration Technologies

As mentioned above, air filters are commonly categorized as physical and non-physical air filters. The most commonly employed physical air filters include fibrous filters and activated carbon adsorbents. Meanwhile, other non-physical filtration methods consist of ultraviolet (UV) irradiation and electronic air cleaners, which operate under different mechanisms [7-8]. Despite the wide range of available technologies, fibrous filters have emerged as the more popular choice due to their low cost, high filtration performance, ease of fabrication, large specific surface area and tunable surface chemistry [11-14]. It is also widely known that fibrous filters are the most efficient filters for trapping particles of different diameters [7-8, 15]. Although other filtration technologies are also employed in the industry, these technologies are not as efficient as fibrous filters in terms of their overall filtration efficiency and environmental sustainability. For example, the use of activated carbon is only targeted at the removal of odor, volatile organic compounds (VOCs) and gases via surface adsorption [16-17]. Moreover, activated carbon adsorbents typically possess low loading capacity (short lifetime) and are often used in conjunction with a pre-filter to reduce saturation of the pores. In addition, the air resistance across activated carbon adsorbents are known to be very large. Meanwhile, UV irradiation involves the use of UV light to deactivate microbiological pollutants but are generally ineffective in the removal of PM [18-19]. Furthermore, electronic air cleaners, which encompass the use of high voltages to generate an electric field to capture particles, produces ozone as a by-product and the filtration efficiency is much lower than that of fibrous filters [7, 20-21]. Thus, among all the available filtration technologies, fibrous

filter proves to be more environmentally sustainable and highly efficient for a wide range of particle sizes including ultrafine particles.

2.3 Two-Dimensional (2D) Fibrous Media
2.3.1 Filtration Mechanism of Fibrous Media

Air filtration in a fibrous medium is governed by four main mechanisms known as sieving, inertial impaction, interception and Brownian diffusion [22-23]. The particle capturing effectiveness of each mechanism is mainly influenced by the particle size and face velocity. The sieving method allows for the removal of particles with sizes larger than the pore size. When the filter pore sizes are smaller than the particle diameters, large particles will be captured and adsorbed onto the fiber surface. As illustrated in Figure 2.1, removal via interception happens when flowing particles experience van der Waals forces when nearing a fiber, causing them to deviate from the airflow streamlines and contact the fiber surface [23]. Interception is the main capture mechanism for particles with sizes between 0.1-1.0 µm, and becomes more dominant with increasing size. When approaching a fiber, inertial impaction occurs when particles impinge and deposit onto nearby fiber surfaces when they are unable to follow the curving contours of the air stream under the action of inertia [24]. This mechanism prevails for particles in the range of 0.3-1.0 µm, and becomes more pronounced for larger particle sizes and at higher face velocities. Diffusion capture is based on the Brownian motion of air particles [23]. The longer the mean free path of the particles, the chances of the particles getting adsorbed onto the fiber surface will be greater. Brownian diffusion is the main capture mechanism for ultrafine particles, and becomes more significant with decreasing particle size under low face velocities. Therefore, to enhance the capture efficiency of ultrafine particles, the filter should be endowed with features that can promote diffusion capture of these particles.
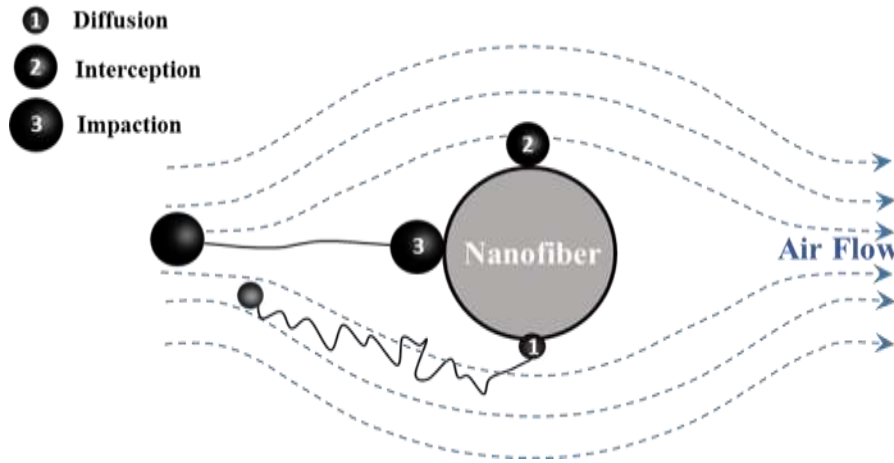
Figure 2. 1 The particle flow regime in a fibrous medium.

Besides particle size and face velocity, the single fiber diameter also has some influence on the particle capturing effectiveness of each mechanism[23, 25]. Figure 2.2 shows the typical trend of the capture efficiency curves of fibrous filters as a function of particle size and fiber diameter, where the minimum of each curve corresponds to the most penetrating particle size (MPPS) of each filter. Studies have shown that reducing the fiber diameter could enhance the interception and diffusion capture of smaller particles, shifting the MPPS to smaller sizes and improving the overall efficiency, which may be beneficial for the capture of ultrafine particles [26]. Thus, smaller fiber diameters should be incorporated into the fabrication of fibrous filters to improve the overall filtration efficiency, including that of ultrafine particles. Nonetheless, it is worthy to mention that excessively small fiber diameters may also shift the MPPS towards the ultrafine region, which could eventually reduce the filtration efficiency of ultrafine particles despite attaining higher overall efficiency. Hence, the balance between ultrafine filtration efficiency and fiber diameter should also be addressed.
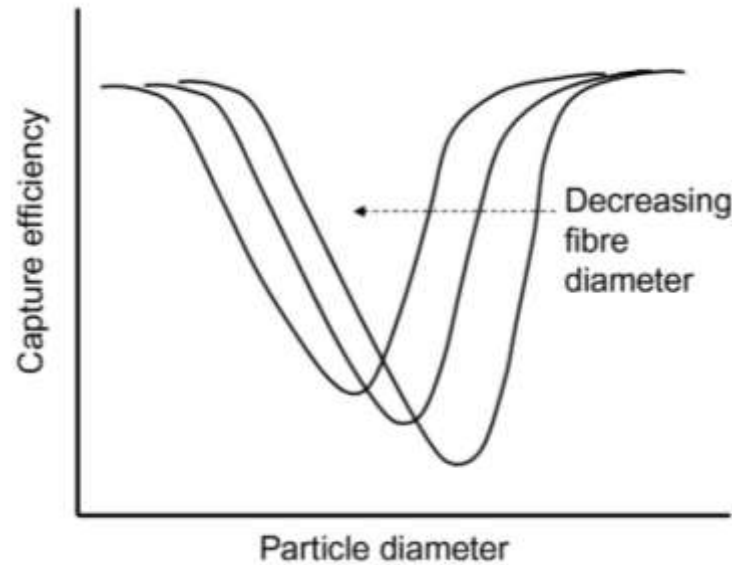
Figure 2. 2 Particle capture efficiency as a function of particle size and microfiber size [27].

2.3.2 Conventional Fibrous Filters

Conventional fibrous filters generally consist of non-woven microfibrous (few microns to tens of microns) membranes made of fiberglass or polymers such as polypropylene (PP) and polyesters, which are extensively used in applications that require air quality control, especially in industrial and residential HVAC systems, hospitals, automotive cabins and breathing apparatus [8]. These filters are usually classified into four categories: primary, mid efficiency, mid-high efficiency and high efficiency particulate arrestance (HEPA) filters (Table 2.1). The first three types of filters usually demonstrate lower filtration efficiencies and are generally used to remove larger dust particles in the range of 1-10 µm [8, 28]; they are, however, not effective for the removal of submicron particles including ultrafine particles. Alternatively, HEPA filters, which possess smaller fiber diameters (few microns) and higher fiber packing density, are able to achieve at least 95-99.97 % filtration efficiency for both micron and submicron particles [28]. Nonetheless, the high fiber packing density would significantly increase the resistance of the medium to airflow,

causing higher energy consumption (Table 2.1). Thus, the trade-off between filtration efficiency and ΔP still remains a challenge in the air filtration industry.

Table 2. 1 Classification of the different types of commercial air filters [28].

Class	Particle size	Efficiency under working velocity (%)	Initial ΔP under working velocity (Pa)	Corresponding air filter type in European standards
Primary filter	PM_{10}	0-20	Below 30	G1, G2, G3
	$PM_{2.5}$	0-12		
	$PM_{1.0}$	0-10		
Mid efficiency filter	PM_{10}	20-40	Below 50	G4, M5, M6
	$PM_{2.5}$	12-30		
	$PM_{1.0}$	10-15		
Mid-high efficiency filter	PM_{10}	40-70	Below 100	F7, F8, F9
	$PM_{2.5}$	30-65		
	$PM_{1.0}$	15-60		
High efficiency particulate arrestance (HEPA) filter	PM_{10}	70-about 100	Below 300	Above H10 (H10 included)
	$PM_{2.5}$	65-about 100		
	$PM_{1.0}$	60-about 100		

2.3.3 Development in Nanofibrous Mat (NFM) Filters

To address the trade-off between filtration efficiency and ΔP, many researchers have proposed the addition of a thin layer of nanofibrous mat (NFM) to significantly improve the ultrafine filtration performance of microfibrous filters. Nanofibers, which are commonly produced via melt-blowing or electrospinning, are endowed

with finer fiber diameters and larger specific surface area that could greatly enhance the filtration efficiency with a slight increase in ΔP when combined with a microfibrous filter [15, 29-32]. Furthermore, the nanometer-size fibers could help to enhance the diffusion and interception capture of ultrafine particles while the slip flow effect of nanofibers may lower airflow resistance to some extent, resulting in a smaller increase in pressure drop of the composite filters [33-36]. For example, Wang et. al demonstrated that the addition of poly(lactic) acid (PLA) nanofibers to PLA microfibers could greatly enhance the filtration efficiency (98.64% to 99.999%) for 75 nm particles with a significantly large ΔP of 683.2 Pa at a face velocity of 14.1 cm/s [30]. Tang et. al also revealed that a thin laminated nanofibrous layer on a MERV 14 electret filter could help to improve the filtration efficiency of 50 nm particles from 60% to 80%, which is accompanied with a relatively high ΔP of 175 Pa at a high face velocity of 25 cm/s [31]. Nevertheless, the improved efficiency of ultrafine particles is often achieved via the addition of more nanofibers on the microfiber substrate (higher fiber packing density), which would often result in the elevation of ΔP, offsetting the benefits of the high filtration efficiency.

Besides adopting the composite filter approach, several other methods that solely employ NFMs as filters have also been reported for improving the filtration efficiency for ultrafine particles. For example, Zhang et. al. reported a polyamide-6 nanofiber/net membrane filter that can achieve 99.995% filtration efficiency for ultrafine particles, which is accompanied with a high ΔP of 101 Pa at a relatively low face velocity of ~5.3 cm/s [37]. Li et. al also fabricated poly(ether sulfone) hollow nanofibers for capturing ultrafine particles, and they attained the $PM_{0.1}$ efficiency of > 99.995% but simultaneously encountered a relatively high pressure drop of 55-56 Pa at a low face velocity of 2.6 cm/s [38]. In general, nanofibrous filters could exhibit higher filtration efficiency than their microfibrous counterparts due to their much larger specific surface area that increase diffusion and interception capture [11-12, 39-40]. However, in NFMs, the nanofibers are packed in roughly parallel planes. Thus, the high efficiency removal of ultrafine particles is still accompanied with a surge in air

resistance across the filters due to their high fiber packing densities, which is not energy-efficient for filtration applications.

Apart from the trade-off between filtration efficiency and ΔP, the rapid deposition of particles on the NFM filter is more pronounced than that of microfibrous filters, owing to the finer diameters and smaller pore size of the 2D mats/membranes [41]. Due to the compact and dense structures of fibrous mats/membranes, the effective filtration area typically occurs only on the surface and the adsorbed particles will eventually accumulate to form a thick layer, a process known as cake filtration [42]. In other words, depth filtration does not occur effectively within the filter, limiting the loading capacity of NFMs. The formation of the cake would eventually clog up the pores of the filter, reducing the filtration efficiency and causing the ΔP to increase significantly, which diminishes the lifetime of NFM filters. Therefore, besides addressing the trade-off between filtration efficiency and ΔP, there is an urgent need to develop a new kind of filter with anti-clogging features that could make the filters more durable.

2.4 Three-Dimensional (3D) Air Filtration

2.4.1 Concept of 3D Air Filtration

More recently, to address the aforementioned issues, three-dimensional (3D) aerogels have also been employed as air filters. This new kind of 3D filter possesses superior qualities such as ultrahigh porosity and ultralow density. Unlike conventional filters that are compact and dense, the ultrahigh porosity of 3D aerogels could facilitate lesser drag force experienced by the filter while the large internal volume could promote diffusion capture of ultrafine particles (longer residence time), alleviating the trade-off between filtration efficiency and ΔP. Furthermore, the highly porous structure of aerogels could improve the clogging issues experienced by conventional mat/membrane-based fibrous filters. Rather than undergoing surface filtration, the large volume of voids within the aerogel structure can provide for depth filtration of particles, which could make them more clog-resistant and

increase the loading capacity, thus extending the lifetime of these filters[43]. Generally, aerogel filters can be classified under two categories: fibrous aerogels and non-fibrous aerogels.

2.4.2 Development in Nanofibrous Aerogel (NFA) Filters

To overcome the tradeoff between filtration efficiency and pressure drop, the concept of three-dimensional (3D) nanofibrous filters, in which the nanofibers are more loosely packed and oriented more randomly than that in the 2D NFMs, has been proposed based on simulation studies [33, 44-46]. The larger internal volume of the "3D" filter could provide longer residence time to ultrafine particles, increasing the probability of diffusion capture on nanofibers, while the higher porosity of the 3D filter, combined with the slip flow effect for nanofibers [33-36], could lead to a smaller pressure drop across the filter. Various methods have been reported for fabrication of 3D nanofibrous macrostructures for different applications [47]. Some of these reported "3D" nanofibrous macrostructures have pseudo 3D morphologies consisting of several layers of 2D nanofibrous mats, and hence are still fairly denser [48-50]. Some electrospinning techniques, such as liquid collection followed by freeze-drying and self-assembly of fibrous stacks are able to achieve highly porous 3D macrostructures [51-53], which could, however, easily collapse due to the absence of strong inter-fiber interactions, making them unsuitable for practical applications. In the case of air filtration, airflow-induced compression force may cause highly porous 3D filters to collapse into much denser ones, restricting their application as air filters.

In response to the poor structural stabilities of these highly porous NFAs, many researchers have reported various approaches to introduce inter-fiber chemical and/or physical cross-links to improve the robustness of NFAs. For instance, Qian et. al reported a novel polyimide (PI) aerogel filter with thermally induced cross-links, which demonstrated no deformation even after 1000 loading-unloading fatigue cycles. Moreover, the PI NFA filter exhibited 99.9% filtration efficiency for $PM_{2.5}$, accompanied with a reasonable ΔP of 177 Pa, at a high face velocity of 20.5 cm/s [10].

Feng et. al also reported a kymene-assisted cross-linked cellulose aerogel with improved robustness and flexibility [54]. In addition, Deuber et. al also used a thermal cross-linking procedure to render their pullulan/poly(vinyl alcohol) (Pul/PVA) blend 3D NFA filters with improved mechanical stability. They also attempted to investigate the potential of NFAs as deep-bed filters, revealing the synergistic effects of ultrahigh porosity and ultralow density of NFAs can promote much higher dust loadings than nanofibrous membranes (NFMs) without compromising the filter performance, which extends the service life of these 3D filters [43]. However, it is also worth noting that although thermal cross-linking has emerged as a more facile and cheaper method, many researchers have also reported annealing-induced shrinkage of the porous materials, especially at relatively high heat treatment temperatures (> 500°C), which could induce pore size reduction or even pore structural change of the porous materials [55-57]. In addition, conventional choices of polymeric nanofibers and/or the cross-linking agents employed are typically made of petrochemicals or synthetic chemicals generated from non-renewable precursors that are harmful to the environment, which hampers their practical applications. Therefore, there is a need to identify a more economically viable and environmentally benign cross-linking agent or process that could make 3D NFA filters more robust and durable, while at the same time largely reduce the negative effect of the cross-linking process on the morphology of the NFAs so that high filtration efficiency and low ΔP can be achieved simultaneously.

2.4.3 Development in Non-Fibrous Aerogel Filters

On the other hand, non-fibrous aerogels have also emerged as potential alternatives to replace conventional fibrous filters. Differently from NFAs, the reported non-fibrous aerogel consists of aligned micrometer-sized hollow channels, which are typically prepared via unidirectional freezing of the precursor solution/suspension followed by freeze-drying [58]. In brief, a temperature gradient is created between the bottom and top of the solution/suspension, inducing the upward spurt of ice-crystals that could act as templates to generate the aligned hollow pores. The larger the

temperature gradient, the faster the growth of the ice-crystals, facilitating the formation of smaller pores. Similar to NFAs, the large internal volume of the non-fibrous aerogel could promote diffusion capture of ultrafine particles while the hollow through-pores could facilitate a smaller drag force experienced by the filter. For example, Zhang et. al prepared a graphene-oxide/modified tourmaline nanoparticle aerogel with aligned porous architectures (40-100 µm) that exhibited high $PM_{2.5}$ efficiency of incense particles (95.1%) with a low $\Delta P < 40$ Pa, which further confirms the synergistic benefits of such porous structures to overcome the trade-off between efficiency and ΔP [59]. Furthermore, recent works on cross-flow filtration also demonstrated that aligned hollow channels could achieve much lower ΔP values that are only one-fifth of that of normal filtration mode [60-61]. In addition, simulation studies have also suggested that cross-flow filtration removed particles based on size-dependent trajectory segregation, where smaller particles are deposited on the walls of the filter media while the larger ones travel continuously along the air flow, thereby signifying that the diffusion capture of ultrafine particles could be enhanced by introducing hollow channels [62]. However, since the reported aligned hollow fibers possess relatively large inner diameters (> 500 µm), the filtration efficiency calculated based on the before and after test concentrations at two ends of the hollow fibers were fairly low. Therefore, although these unconventional non-fibrous aerogels have been explored as alternatives to fibrous filters, the filtration mechanism of these materials have not yet been investigated and the starting materials used stem from non-renewable resources, which are not environmentally sustainable. Thus, besides addressing the issue of material renewability, it is crucial to conduct a systematic study on the filtration mechanism of aerogels with smaller aligned pore channels to further assess the potential of these materials in the field of air filtration.

On top of all the benefits that aligned hollow through-pores can offer, it is also important to highlight the potential of the concomitant clog-resistant feature of these non-fibrous aerogels. Since the pores are hollow and significantly larger than that of fibrous filters[59], it may take a longer time for particles to accumulate and block the

pores entirely, which could render the filters a longer service life and higher loading capacity. So far, there is no reported work on the anti-clogging features of non-fibrous aerogels. Hence, it is also crucial to assess the extent of anti-clogging properties that could be offered by such unique aligned porous architectures.

2.5 Bridging the Gap

In summary, 3D aerogel filters (fibrous and non-fibrous) exhibit great potential to be used as the next generation of air filters for ultrafine particles due to the synergistic effect of their ultrahigh porosities and ultralow densities that may overcome the trade-off between efficiency and ΔP. Nonetheless, several key performance parameters such as the mechanical robustness, material renewability, biodegradability and production cost still remain a challenge, which could hamper their practical applications. Furthermore, the filtration mechanism and clog-resistant properties of non-fibrous aerogels are not well understood, with only one reported work thus far. Hence, this PhD study will focus on the preparation of sustainable robust aerogel filters through more environmentally benign fabrication methods and adopt the use of renewable materials as well as investigate the respective filtration mechanism through the designs introduced in Chapter 1.

References

1.   Betha, R.; Behera, S. N.; Balasubramanian, R., 2013 Southeast Asian Smoke Haze: Fractionation of Particulate-Bound Elements and Associated Health Risk. *Environmental Science & Technology* **2014,** *48* (8), 4327-4335.

2.   Wang, X.; Chen, J.; Cheng, T.; Zhang, R.; Wang, X., Particle number concentration, size distribution and chemical composition during haze and photochemical smog episodes in Shanghai. *Journal of Environmental Sciences* **2014,** *26* (9), 1894-1902.

3.   Kwasny, F.; Madl, P.; Hofmann, W., Correlation of air quality data to ultrafine particles (UFP) concentration and size distribution in ambient air. *Atmosphere* **2010,** *1* (1), 3-14.

4.   Tiwari, M.; Sahu, S. K.; Bhangare, R. C.; Yousaf, A.; Pandit, G. G., Particle size distributions of ultrafine combustion aerosols generated from household fuels. *Atmospheric Pollution Research* **2014,** *5* (1), 145-150.

5.   Zhang, Q.; Jiang, X.; Tong, D.; Davis, S. J.; Zhao, H.; Geng, G.; Feng, T.; Zheng, B.; Lu, Z.; Streets, D. G., Transboundary health impacts of transported global air pollution and international trade. *Nature* **2017,** *543* (7647), 705.

6.   Ostro, B.; Hu, J.; Goldberg, D.; Reynolds, P.; Hertz, A.; Bernstein, L.; Kleeman, M. J., Associations of mortality with long-term exposures to fine and ultrafine particles, species and sources: results from the California Teachers Study Cohort. *Environmental health perspectives* **2015,** *123* (6), 549.

7.   Brincat, J.-P.; Sardella, D.; Muscat, A.; Decelis, S.; Grima, J. N.; Valdramidis, V.; Gatt, R., A review of the state-of-the-art in air filtration technologies as may be applied to cold storage warehouses. *Trends in Food Science & Technology* **2016,** *50*, 175-185.

8.   Liu, G.; Xiao, M.; Zhang, X.; Gal, C.; Chen, X.; Liu, L.; Pan, S.; Wu, J.; Tang, L.; Clements-Croome, D., A review of air filtration technologies for sustainable and healthy building ventilation. *Sustainable Cities and Society* **2017,** *32* (Supplement C), 375-396.

9.   Zhang, R.; Liu, C.; Hsu, P.-C.; Zhang, C.; Liu, N.; Zhang, J.; Lee, H. R.; Lu, Y.; Qiu, Y.; Chu, S.; Cui, Y., Nanofiber Air Filters with High-Temperature Stability

for Efficient PM2.5 Removal from the Pollution Sources. *Nano Letters* **2016,** *16* (6), 3642-3649.

10.   Qian, Z.; Wang, Z.; Chen, Y.; Tong, S.; Ge, M.; Zhao, N.; Xu, J., Superelastic and ultralight polyimide aerogels as thermal insulators and particulate air filters. *Journal of Materials Chemistry A* **2018,** *6* (3), 828-832.

11.   Liu, C.; Hsu, P. C.; Lee, H. W.; Ye, M.; Zheng, G.; Liu, N.; Li, W.; Cui, Y., Transparent air filter for high-efficiency PM2.5 capture. *Nat Commun* **2015,** *6*, 6205.

12.   Wang, C.; Wu, S.; Jian, M.; Xie, J.; Xu, L.; Yang, X.; Zheng, Q.; Zhang, Y., Silk nanofibers as high efficient and lightweight air filter. *Nano Research* **2016,** *9* (9), 2590-2597.

13.   Li, J.; Zhang, D.; Yang, T.; Yang, S.; Yang, X.; Zhu, H., Nanofibrous membrane of graphene oxide-in-polyacrylonitrile composite with low filtration resistance for the effective capture of PM2. 5. *Journal of membrane science* **2018,** *551*, 85-92.

14.   Huang, X.; Jiao, T.; Liu, Q.; Zhang, L.; Zhou, J.; Li, B.; Peng, Q., Hierarchical electrospun nanofibers treated by solvent vapor annealing as air filtration mat for high-efficiency PM2. 5 capture. *Science China Materials* **2019,** *62* (3), 423-436.

15.   Podgorski, A.; Bałazy, A.; Gradoń, L., Application of nanofibers to improve the filtration efficiency of the most penetrating aerosol particles in fibrous filters. *Chemical Engineering Science* **2006,** *61* (20), 6804-6815.

16.   Wang, Z.; Zhang, J. S., Characterization and performance evaluation of a full-scale activated carbon-based dynamic botanical air filtration system for improving indoor air quality. *Building and Environment* **2011,** *46* (3), 758-768.

17.   Sundarrajan, S.; Tan, K. L.; Lim, S. H.; Ramakrishna, S., Electrospun nanofibers for air filtration applications. *Procedia Eng* **2014,** *75*, 159-163.

18.   Jensen, M. M., Inactivation of airborne viruses by ultraviolet irradiation. *Appl. Environ. Microbiol.* **1964,** *12* (5), 418-420.

19.   Jeong, J.; Sekiguchi, K.; Sakamoto, K., Photochemical and photocatalytic degradation of gaseous toluene using short-wavelength UV irradiation with TiO2 catalyst: comparison of three UV sources. *Chemosphere* **2004,** *57* (7), 663-671.

20.   Lin, W.-Y.; Chang, Y.-Y.; Lien, C.-T.; Kuo, C.-W., Separation characteristics of submicron particles in an electrostatic precipitator with alternating electric field corona charger. *Aerosol Science and Technology* **2011,** *45* (3), 393-400.

21.   Boelter, K. J.; Davidson, J. H., Ozone generation by indoor, electrostatic air cleaners. *Aerosol science and technology* **1997,** *27* (6), 689-708.

22.   Zhu, M.; Han, J.; Wang, F.; Shao, W.; Xiong, R.; Zhang, Q.; Pan, H.; Yang, Y.; Samal, S. K.; Zhang, F., Electrospun nanofibers membranes for effective air filtration. *Macromolecular Materials and Engineering* **2017,** *302* (1), 1600353.

23.   Chuanfang, Y., Aerosol filtration application using fibrous media—an industrial perspective. *Chinese journal of chemical Engineering* **2012,** *20* (1), 1-9.

24.   Ramskill, E. A.; Anderson, W. L., The inertial mechanism in the mechanical filtration of aerosols. *Journal of Colloid Science* **1951,** *6* (5), 416-428.

25.   Zhu, C.; Lin, C.-H.; Cheung, C. S., Inertial impaction-dominated fibrous filtration with rectangular or cylindrical fibers. *Powder technology* **2000,** *112* (1-2), 149-162.

26.   Hinds, W. C., *Aerosol technology: properties, behavior, and measurement of airborne particles*. John Wiley & Sons: 1999.

27.   Sparks, T.; Chase, G., Section 2-Filter Media. *Filters and Filtration Handbook (Sixth Edition)* **2016**, 55-115.

28.   Sparks, T.; Chase, G., Section 7 - Filter Selection, Process Design, Testing, Optimization and Troubleshooting Guidelines. In *Filters and Filtration Handbook (Sixth Edition)*, Sparks, T.; Chase, G., Eds. Butterworth-Heinemann: Oxford, 2016; pp 383-413.

29.   Leung, W. W.-F.; Hung, C.-H.; Yuen, P.-T., Effect of face velocity, nanofiber packing density and thickness on filtration performance of filters with nanofibers coated on a substrate. *Separation and purification technology* **2010,** *71* (1), 30-37.

30.   Wang, Z.; Pan, Z., Preparation of hierarchical structured nano-sized/porous poly (lactic acid) composite fibrous membranes for air filtration. *Applied Surface Science* **2015,** *356*, 1168-1179.

31.   Tang, M.; Chen, S.-C.; Chang, D.-Q.; Xie, X.; Sun, J.; Pui, D. Y., Filtration efficiency and loading characteristics of PM2. 5 through composite filter media consisting of commercial HVAC electret media and nanofiber layer. *Separation and Purification Technology* **2018,** *198*, 137-145.

32.   Barhate, R. S.; Ramakrishna, S., Nanofibrous filtering media: Filtration problems and solutions from tiny materials. *Journal of Membrane Science* **2007,** *296* (1–2), 1-8.

33.   Sambaer, W.; Zatloukal, M.; Kimmer, D., 3D modeling of filtration process via polyurethane nanofiber based nonwoven filters prepared by electrospinning process. *Chemical Engineering Science* **2011,** *66* (4), 613-623.

34.   Graham, K.; Ouyang, M.; Raether, T.; Grafe, T.; McDonald, B.; Knauf, P. In *Polymeric nanofibers in air filtration applications*, Fifteenth Annual Technical Conference & Expo of the American Filtration & Separations Society, Galveston, Texas, 2002; pp 9-12.

35.   Zhao, X.; Wang, S.; Yin, X.; Yu, J.; Ding, B., Slip-Effect Functional Air Filter for Efficient Purification of PM 2.5. *Scientific reports* **2016,** *6*, 35472.

36.   Hung, C.-H.; Leung, W. W.-F., Filtration of nano-aerosol using nanofiber filter under low Peclet number and transitional flow regime. *Separation and purification technology* **2011,** *79* (1), 34-42.

37.   Zhang, S.; Liu, H.; Yu, J.; Luo, W.; Ding, B., Microwave structured polyamide-6 nanofiber/net membrane with embedded poly (m-phenylene isophthalamide) staple fibers for effective ultrafine particle filtration. *Journal of Materials Chemistry A* **2016,** *4* (16), 6149-6157.

38.   Li, M.; Feng, Y.; Wang, K.; Yong, W. F.; Yu, L.; Chung, T.-S., Novel hollow fiber air filters for the removal of ultrafine particles in PM2. 5 with repetitive usage capability. *Environmental Science & Technology* **2017,** *51* (17), 10041-10049.

39.   Chen, X.; Xu, Y.; Liang, M.; Ke, Q.; Fang, Y.; Xu, H.; Jin, X.; Huang, C., Honeycomb-like polysulphone/polyurethane nanofiber filter for the removal of organic/inorganic species from air streams. *Journal of hazardous materials* **2018**.

40.   Bulejko, P.; Dohnal, M.; Pospíšil, J.; Svěrák, T., Air filtration performance of symmetric polypropylene hollow-fibre membranes for nanoparticle removal. *Separation and Purification Technology* **2018,** *197*, 122-128.

41.   Al-Otoom, A. Y., Prediction of the collection efficiency, the porosity, and the pressure drop across filter cakes in particulate air filtration. *Atmospheric Environment* **2005,** *39* (1), 51-57.

42.   Leung, W. W.-F.; Choy, H.-F., Transition from depth-to-surface filtration for a high-efficiency, high-skin effect, nanofiber filter under continuous nano-aerosol loading. *Chemical Engineering Science* **2018,** *182*, 67-76.

43.   Deuber, F.; Mousavi, S.; Federer, L.; Hofer, M.; Adlhart, C., Exploration of ultralight nanofiber aerogels as particle filters: capacity and efficiency. *ACS applied materials & interfaces* **2018,** *10* (10), 9069-9076.

44.   Sambaer, W.; Zatloukal, M.; Kimmer, D., 3D air filtration modeling for nanofiber based filters in the ultrafine particle size range. *Chemical Engineering Science* **2012,** *82* (Supplement C), 299-311.

45.   Hosseini, S.; Tafreshi, H. V., Modeling permeability of 3-D nanofiber media in slip flow regime. *Chemical Engineering Science* **2010,** *65* (6), 2249-2254.

46.   Li, P.; Wang, C.; Zhang, Y.; Wei, F., Air Filtration in the Free Molecular Flow Regime: A Review of High-Efficiency Particulate Air Filters Based on Carbon Nanotubes. *Small* **2014,** *10* (22), 4543-4561.

47.   Xu, J.; Liu, C.; Hsu, P.-C.; Liu, K.; Zhang, R.; Liu, Y.; Cui, Y., Roll-to-roll transfer of electrospun nanofiber film for high-efficiency transparent air filter. *Nano letters* **2016,** *16* (2), 1270-1275.

48.   Pham, Q. P.; Sharma, U.; Mikos, A. G., Electrospun poly (ε-caprolactone) microfiber and multilayer nanofiber/microfiber scaffolds: characterization of scaffolds and measurement of cellular infiltration. *Biomacromolecules* **2006,** *7* (10), 2796-2805.

49.   Wang, W.; Itoh, S.; Matsuda, A.; Ichinose, S.; Shinomiya, K.; Hata, Y.; Tanaka, J., Influences of mechanical properties and permeability on chitosan nano/microfiber mesh tubes as a scaffold for nerve regeneration. *Journal of Biomedical Materials Research Part A* **2008,** *84A* (2), 557-566.

50.   Wang, W.; Itoh, S.; Konno, K.; Kikkawa, T.; Ichinose, S.; Sakai, K.; Ohkuma, T.; Watabe, K., Effects of Schwann cell alignment along the oriented electrospun chitosan nanofibers on nerve regeneration. *Journal of Biomedical Materials Research Part A* **2009,** *91* (4), 994-1005.

51.   Yao, Q.; Cosme, J. G.; Xu, T.; Miszuk, J. M.; Picciani, P. H.; Fong, H.; Sun, H., Three dimensional electrospun PCL/PLA blend nanofibrous scaffolds with significantly improved stem cells osteogenic differentiation and cranial bone formation. *Biomaterials* **2017,** *115*, 115-127.

52.   Sun, B.; Long, Y.-Z.; Yu, F.; Li, M.-M.; Zhang, H.-D.; Li, W.-J.; Xu, T.-X., Self-assembly of a three-dimensional fibrous polymer sponge by electrospinning. *Nanoscale* **2012,** *4* (6), 2134-2137.

53.   Bonino, C. A.; Efimenko, K.; Jeong, S. I.; Krebs, M. D.; Alsberg, E.; Khan, S. A., Three-dimensional electrospun alginate nanofiber mats via tailored charge repulsions. *Small* **2012,** *8* (12), 1928-1936.

54.   Feng, J.; Nguyen, S. T.; Fan, Z.; Duong, H. M., Advanced fabrication and oil absorption properties of super-hydrophobic recycled cellulose aerogels. *Chemical Engineering Journal* **2015,** *270*, 168-175.

55.   Li, L.; Hu, T.; Sun, H.; Zhang, J.; Wang, A., Pressure-sensitive and conductive carbon aerogels from poplars catkins for selective oil absorption and oil/water separation. *ACS applied materials & interfaces* **2017,** *9* (21), 18001-18007.

56.   Meador, M. A. B.; Alemán, C. R.; Hanson, K.; Ramirez, N.; Vivod, S. L.; Wilmoth, N.; McCorkle, L., Polyimide aerogels with amide cross-links: a low cost alternative for mechanically strong polymer aerogels. *ACS applied materials & interfaces* **2015,** *7* (2), 1240-1249.

57.   Pakula, T.; Trznadel, M., Thermally stimulated shrinkage forces in oriented polymers: 1. Temperature dependence. *Polymer* **1985,** *26* (7), 1011-1018.

58.   Gutiérrez, M. C.; Ferrer, M. L.; del Monte, F., Ice-templated materials: Sophisticated structures exhibiting enhanced functionalities obtained after unidirectional freezing and ice-segregation-induced self-assembly. *Chemistry of Materials* **2008,** *20* (3), 634-648.

59.   Zhang, S.; Sun, J.; Hu, D.; Xiao, C.; Zhuo, Q.; Wang, J.; Qin, C.; Dai, L., Large-sized graphene oxide/modified tourmaline nanoparticle aerogel with stable honeycomb-like structure for high-efficiency PM 2.5 capture. *Journal of Materials Chemistry A* **2018,** *6* (33), 16139-16148.

60.   Wang, L.-Y.; Liya, E. Y.; Lai, J.-Y.; Chung, T.-S., Developing ultra-high gas permeance PVDF hollow fibers for air filtration applications. *Separation and Purification Technology* **2018,** *205*, 184-195.

61.   Wang, L.-Y.; Yong, W. F.; Liya, E. Y.; Chung, T.-S., Design of high efficiency PVDF-PEG hollow fibers for air filtration of ultrafine particles. *Journal of Membrane Science* **2017,** *535*, 342-349.

62.   Sibanda, V.; Greenwood, R.; Seville, J.; Ding, Y.; Iyuke, S., Predicting particle segregation in cross-flow gas filtration. *Powder Technology* **2010,** *203* (3), 419-427.

Chapter 3

Experimental Methodology

In this chapter, the selection of all the materials used in this thesis study is presented, and the rationale for choosing these materials is elaborated. The methods used to fabricate the aerogels (i.e., electrospinning and unidirectional freezing) are explained, and why these methods are appropriate for the fabrication of aerogels for air filtration applications are justified. For the filtration test, the reasons for selecting the model haze particles are rationalized, and the underlying principles of conventional particle detection techniques used to detect the model haze particles are explained. Fundamental theories and working principles of all the characterization techniques carried out in this PhD study are also presented, and how these techniques are relevant for the respective studies are explained.

3.1 Rationale for Material Selection

In the previous chapter, the concept of 3D filtration was introduced to address the trade-off relationship between filtration efficiency and ΔP of fibrous filter media. In order to realize 3D air filtration, aerogels, which are three-dimensional porous materials, have been introduced to be potential 3D air filter materials in the form of NFAs (fibrous) or aerogels with aligned micrometer-sized channels (non-fibrous). Therefore, in this PhD study, poly(lactic) acid stereocomplex (PLLA/PDLA-SC) and regenerated cellulose from cellulose acetate (CA) were chosen as the main starting materials to fabricate the NFAs, while lignin was chosen as the building blocks of the non-fibrous aerogels. To improve the mechanical robustness of the aerogels, graphene in the form of graphene-oxide (GO) and lignin were used as reinforcement agents for designs 2 and 3, respectively, as introduced in Chapter 1. The rationales behind choosing the above mentioned materials for the aerogel preparations are elaborated below.

3.1.1 PLLA/PDLA-SC Nanofibers

Poly(lactic) acid (PLA) is a commonly used bioplastic [1-3] and could be easily electrospun into nanofibers [4-6]. Furthermore, PLA is an environmental-friendly biodegradable polymer that is generated from renewable resources. Besides, the L and D stereoisomers of PLA - poly(L-lactic acid) (PLLA) and poly(D-lactic acid) (PDLA) – possess complementary helical conformations that could interlock each other by stereoselective interactions, forming a stable composite known as a stereocomplex (PLLA/PDLA-SC). It has been widely reported that PLLA and PDLA are able to crystalize in SC form [7]. Its trigonal unit cell of R3c contains 3 formula units per chain, and in the unit cell there are totally 3 pairs of parallel PLLA and PDLA chains with 3_1-helix conformation. Such packing structure facilitates the formation of the three-dimensional network of intermolecular non-conventional hydrogen bonding, leading to its excellent mechanical properties [8-11]. Thus, the spontaneous   stereocomplexation   between   PLLA/PDLA   blend   electrospun

nanofibers have been employed to agglutinate the fibers at touching points, which could enhance the robustness of the 3D NFAs.

3.1.2 Lignin/GO

Lignin is a typical by-product from the paper industry and bio-refineries, which is low cost and widely available in nature [12-13]. It is one of the main structural components of terrestrial plants and is one of the most abundant biomass, thus making it a suitable precursor for fabricating aerogels with potentially minimal environmental footprint. Moreover, studies have shown that lignin lacks cytotoxicity towards living cells, positioning them as environmentally benign materials that could be transformed into value-added products [14-16]. In the experiment, lignin is used as building blocks to fabricate aerogels with aligned hollow pores, providing the aerogels with reasonable structural rigidity. Furthermore, the abundant functional groups present in lignin could facilitate cross-linking reactions to take place during thermal treatment, which may enhance the overall robustness of the aerogel. Besides, the various functional groups present in lignin may promote particle adsorption due to favorable dipole-dipole interactions. However, thermal treatment is known to introduce shrinkage of material [17-18], which may cause the pore size to reduce and increase the ΔP of the aerogel filter. Therefore, a small fraction of graphene could be introduce into the cell walls to reduce the volume shrinkage of the aerogels during the cross-linking process. Graphene normally consists of large stacks of sheets [19], which may facilitate the anchoring of graphene layers along the cell wall during freezing. The anchored graphene sheets could effectively reinforce the cell walls and prevent shrinking when subjected to heat. Hence, the size of the aligned pores could be maintained to ensure low ΔP. In order to incorporate graphene layers into the aerogel cell walls, graphene-oxide (GO) aqueous suspension was used followed by reduction via thermal treatment during the aerogel annealing process. Therefore, both lignin and GO are employed to prepare robust and highly efficient aerogel filters.

3.1.3 Cellulose/Lignin

Cellulose, an important structural component found mainly in plants, is a popular choice of raw material in various applications (e.g. coatings, textiles, papers and sorbents) [20-23] due to its low cost, high abundancy, renewability and biodegradability. It is a biopolymer that typically exists in the form of microfibrils, nanocrystals, nanowhiskers or interconnected networks of nanofibers [24]. In particular, cellulose can also be electrospun into uniform and continuous nanofibers with various desired diameters [25-26], which could offer high specific surface area for PM adsorption. Moreover, the ether and hydroxyl functional groups may also promote strong dipole-dipole or hydrogen bonding interactions with polar organic compounds. However, it remains a challenge to directly electrospin cellulose due to its poor solubility in most electrospinning solvents. Nonetheless, the problem of electrospinnability can be solved through the derivatization of cellulose, which greatly improves the solubility of cellulose in good electrospinning solvents and eventually regenerated cellulose nanofibers can be obtained through a simple hydrolysis step [25]. Thus, in the experiment, cellulose acetate (CA) is first electrospun into nanofibers and subsequently deacetylated to form cellulose nanofibers, which are then used to fabricate the NFAs. Meanwhile, since lignin is also a type of hyperbranched natural macromolecules, a very small amount of lignin was also employed as a molecular cross-linking agent to further reinforce the NFA structure and minimize the aerogel shrinkage during the thermal annealing treatment. As such, the smaller pore contraction could help to minimize the increase in ΔP. Furthermore, with current emphases placed on sustainable living, the work based on cellulose and lignin as the starting materials may prove to be more economically viable and environmentally benign.

3.2 Rationale for the Selected Aerogel Fabrication Methods

In this study, there are two methods adopted to fabricate the aerogels. The first method is to electrospin the nanofibers into a liquid collector and freeze-dry the

fibers in a mold to create the 3D structure [27]. The second method is to prepare a solution/suspension of the starting materials and use the unidirectional freezing method to self-assemble the materials into 3D structures with oriented pores [28-29], followed by freeze-drying. This section will cover the rationales behind choosing these two methods and how are they appropriate to prepare aerogels for air filtration applications, as well as the basic working principles of these methods.

3.2.1 Electrospinning

In the previous chapter, it was revealed that nanofibers could enhance the filtration efficiency of PM as well as the slip flow effect. There are several ways to prepare nanofibers such as template-assisted synthesis [30], phase separation [31], melt spinning [32], multicomponent spinning [33] and electrospinning [27, 34]. Amongst these methods, electrospinning has emerged as the more popular choice due to its ease of processing, simplicity, versatility and low-cost. Especially, electrospinning is also capable of producing uniform and continuous nanofibers, which is vital for the spontaneous formation of fiber entanglements that lead to an interconnected porous macrostructure. Such porous macrostructures create tortuous channels and, when combined with the high specific surface area of nanofibers, could enhance the PM adsorption and achieve high filtration efficiency. Furthermore, for the PLLA/PDLA blend system, in order to fabricate a thin nanofibrous layer, electrospinning offers a good and accurate control over the layer thickness. Thus, in this study, electrospinning is the ideal nanofiber fabrication method to tailor the filtration performance of NFAs for various filtration applications.

The schematic diagram of a typical electrospinning setup is shown in Figure 3.1, which generally consist of a high voltage supply, spinneret, feed solution and a grounded collector. In brief, the feed solution will be fed through a needle at a desired feed rate, and an applied voltage connecting to the spinneret and grounded collector will generate an electric field, which causes charge built-ups at the spinneret needle tip, causing the solution droplet to form a Taylor cone [35]. When the applied voltage

exceeds a certain threshold value, the electrostatic repulsion of the accumulated charges overcomes the surface tension of the solution droplet, generating a charged polymer jet that elongates towards the collector, evaporating the solvent in the process and forming the nanofibers. The fiber diameter and morphology can be fine-tuned simply by adjusting the solution, processing or ambient parameters [27, 34].
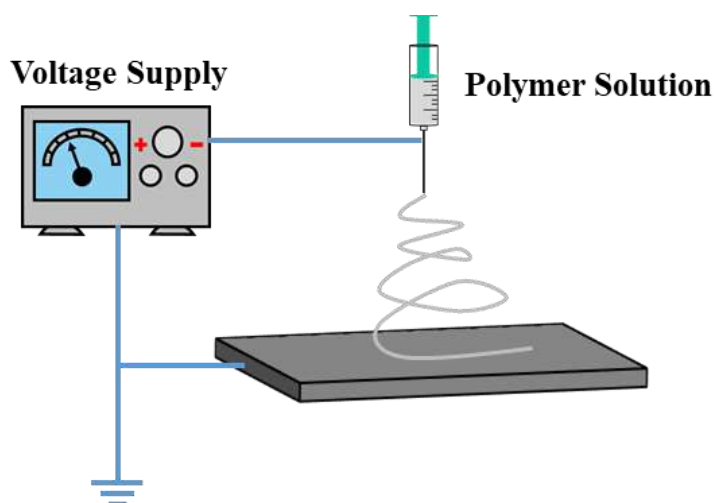
Figure 3. 1 Schematic diagram and digital image of the electrospinning setup.

3.2.2 Unidirectional Freezing

In the previous chapter, besides employing 3D air filters with interconnected porous structures, it was revealed that other novel microstructural designs may also prove to be highly-efficient in promoting the capture of ultrafine particles. In particular, Zhang et. al have shown that non-fibrous aerogels with preferably aligned micrometer-sized pores could promote the diffusion capture of ultrafine particles [36]. Such microstructures are inspired by that of natural wood, which is comprised of vertically aligned tubular channels, and there are several reported methods capable of mimicking such highly-ordered spatial organization such as anodic etching [37], templating [38], extrusion [39] and unidirectional freezing [28, 40]. Amongst these methods, unidirectional freezing, also known as the ice-templating process, stands out due to its ease of processing, high efficiency and applicability to a wide range of materials.

Most importantly, the size of the pore channels can be tailored down to the micrometer-scale, in which the size range is sufficiently small such that ultrafine particles can be captured effectively via diffusion, while at the same time, large enough to ease the airflow. Furthermore, the ice-templating method uses water as the solvent, paving way for a more environmentally benign approach. In addition, complex hierarchical nano/microstructures can also be realized through unidirectional freezing simply by adjusting the material size/compositions of the solution/suspension and freezing rate. Thus, unidirectional freezing is the most-fitting method in order to facilely fabricate aerogels (fibrous or non-fibrous) with preferably aligned pores that can achieve high filtration efficiency and low ΔP simultaneously.

In this study, unidirectional freezing was adopted to fabricate the lignin/GO aerogels (design 2) and cellulose/lignin NFAs (design 3). In brief, the formation of the aligned micrometer-sized pores are due to the temperature-gradient-induced upward spurt of ice crystals during the rapid freezing process followed by a suitable drying process such as freeze-drying to remove the ice. The schematic diagram in Figure 3.2 depicts the typical ice-templating process, which was used to prepare the non-fibrous lignin aerogels. The typical coolant used is liquid nitrogen ($-196^{o}C$) and the temperature gradient is created by using a conductive metal base at the bottom while the solution is casted in an insulated teflon cylindrical jacket.
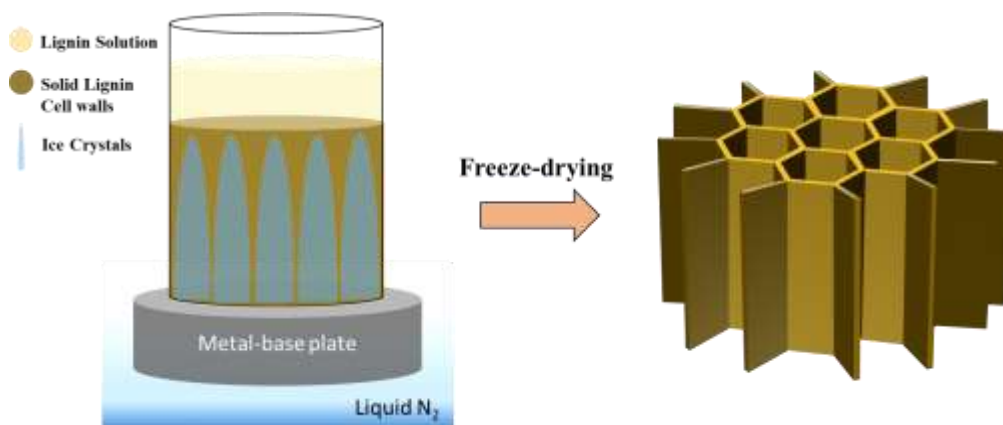
Figure 3. 2 Schematic diagram of the unidirectional freezing method to prepare aerogels with aligned porous architectures.

3.3 Air Filtration Test

In order to assess the filtration performance of our aerogel filters, we designed a filtration testing setup and the schematic diagram of the setup is shown in Figure 3.3. In general, the model haze particles were generated and the $PM_{2.5}$ concentration was controlled by diluting with air in the mixing chamber, down to a concentration equivalent to a hazardous pollution level of ~300 µg/m^3 according to WHO guidelines. The amount of particles are detected by particle sizer instruments and the filtration efficiency can be calculated by comparing the upstream and downstream particle number concentrations of the aerogel filters. The ΔP was measured by taking the pressure difference before and after the filters using a pressure gauge meter. The filtration tests were performed following the two international standards: GB/T 14295-1993, air filters, 2009-06-01; ANSI/ASHRAE standard 52.2-2012 – method of testing general ventilation air-cleaning devices for removal efficiency by particle size.
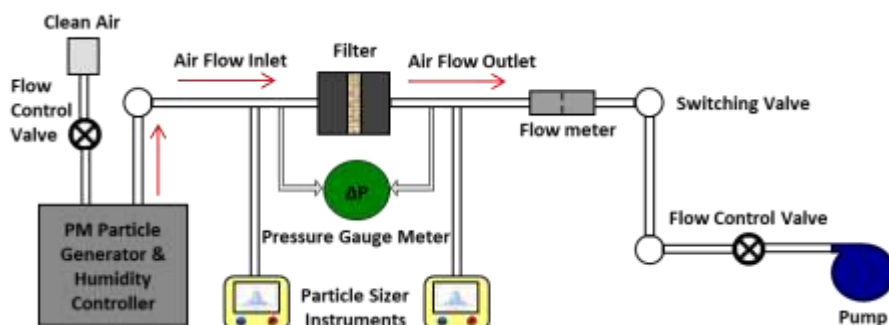
Figure 3. 3 Schematic diagram of the filtration setup used.

3.3.1 Selection of Model Haze Particles

As mentioned previously in both Chapters 1 and 2, studies have shown that airborne PM mainly consists of particles in the ultrafine region, consisting large amounts of organic/inorganic compounds with trace amounts of metals [41]. Therefore, in order to provide a credible overview of the filtration efficiencies of the aerogel filters, the model haze particles used should be carefully selected to accurately simulate the haze particles in terms of the chemical composition and particle size. In this study, we used two types of model haze particles: incense and di(2-ethylhexyl) sebacate (DEHS) particles.

<u>Incense</u>

Studies have shown that incense smoke is comprised of quasi-liquid aerosol particles consisting of volatile organic compounds (VOCs) such as toluene, benzene and xylenes, as well as aldehydes and polycyclic aromatic hydrocarbons (PAHs) [42]. Since the types of organic/inorganic compounds found in incense smoke are closely related to actual haze particles generated by the burning of biomass [41, 43], the adsorption of incense smoke could provide a credible overview of the filtration efficiencies of the filters investigated in this work. To generate incense model haze particles, commercially available incense was burnt and the smoke released was directly used in the filtration test. The mass and number size distributions are presented in Figure 3.4. From the distribution curves, it is found that the particle size

of incense smoke varies in a wide range with majority of the particles being smaller than 0.5 µm. Ultrafine particles ($PM_{0.1}$, i.e., < 0.1 µm) constitute about 22-27% of the total particle mass, whereas the number percentage of $PM_{0.1}$ is approximately 60-70%. This difference can be attributed to the very small mass of the ultrafine particles, which does not contribute significantly to the total mass despite their large quantity in terms of number. Thus, the number size distribution is also a good fit to simulate the actual haze, which is also largely made up of ultrafine particles [44-47].
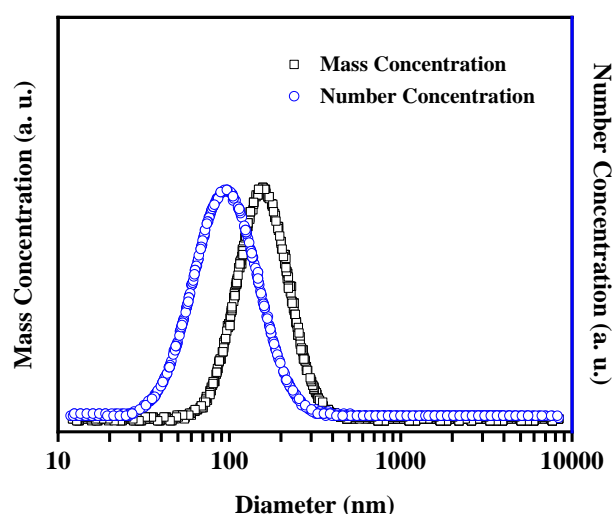
Figure 3. 4 Mass and number size distribution of incense model haze particles.

DEHS

For the second model haze particle system, owing to its polar organic chemistry, DEHS was chosen as the test aerosol. The DEHS particles can be generated using an aerosol generator (TOPAS, SLG 250) with a monodisperse distribution and the schematic diagram of the generator is shown in Figure 3.5a. In brief, NaCl droplets are formed in an atomizer and then dried in a diffusion dryer to generate small NaCl crystals (10-100 nm) that serve as condensation nuclei for vaporized DEHS aerosol to re-condense in a controlled manner to yield monodisperse DEHS aerosols. The size of the aerosol is dependent on the available DEHS vapor per NaCl nucleus,

which can be controlled by simply adjusting the temperature of the saturator or diluting the saturator flow. Depending on the droplet diameter, the lifetime of DEHS particles can range from hours to days, exhibiting excellent stability. As shown in Figure 3.5b, monodisperse distributions of 0.1, 0.3, 0.5 and 1.0 µm can be achieved successfully.
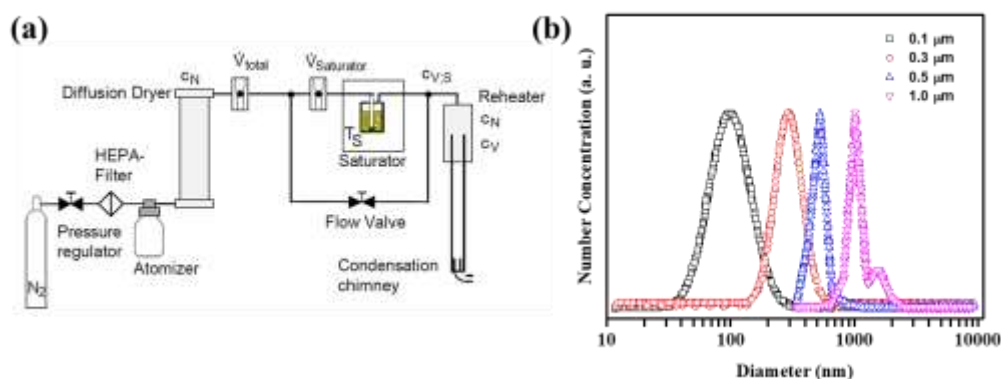
Figure 3. 5 (a) Schematic diagram of the aerosol generation process (image from TOPAS). (b) The number size distributions of various particle sizes used in this study.

3.3.2 Particle Detection Techniques

To detect the amount of particles, particle sizer equipment was employed to accurately measure the number/mass concentration. In this study, two particle counters with different particle detection techniques were used: an optical particle sizer spectrometer that operates on the principle of single particle counting (OPS 3330, TSI Instruments Ld) and a condensation particle counter that incorporates the scanning mobility particle size (SMPS) measurement technique (Nanoscan SMPS 3910, TSI Instruments Ld).

Figure 3.6 shows the typical sample flow path in the OPS. The sample is first passed through the inlet and a sheath flow is generated from a pump to confine the sample particles within the center stream as well as prevent contamination of the optics. The

beam shaping optics then helps to focus and concentrate the laser beam onto the particle beam, creating a viewing volume. Within this volume, particle pulses would be picked up by an elliptical mirror and directed to the photodetector, and eventually the particles will be sized and binned into 16 different channels accordingly. However, since the OPS operates by counting individual pulses in the viewing volume, large concentrations could result in coincidence, leading to poorer counting efficiency and incorrect sizing of the particles. Hence, the particle number detection of the OPS is limited to 3000 #/cm^3. Furthermore, the particle size detection limits of the OPS lies between 0.3 to 10 µm, with only 50% detection efficiency for 0.3 µm particles. Therefore, in this study, the OPS is mainly employed to detect particles with sizes > 0.3 µm.
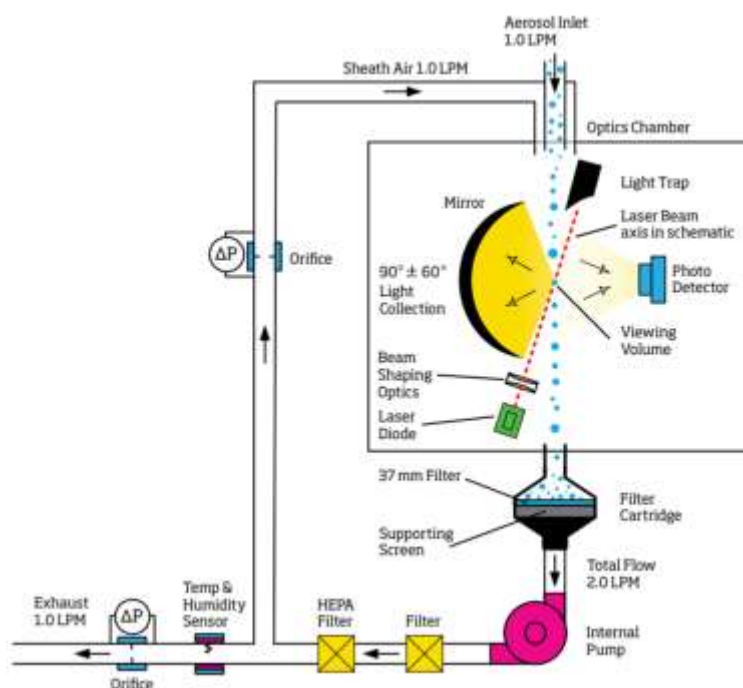
Figure 3. 6 Schematic diagram of the sample flow path in the OPS 3330 (image from TSI).

To make up for the limitation of the OPS, the Nanoscan SMPS 3910 was employed to detect particles with sizes between 0.01 to 0.42 µm, especially for the ultrafine particles. The schematic diagram in Figure 3.7 illustrates the particle detection

process that occurs inside the Nanoscan. Differently, the Nanoscan detects particles via the SMPS particle detection technique. The sample is first pass through the inlet and into a unipolar charger that ensures the particles achieve a consistent charge state. The particles are then introduced into the electric field of a radial differential mobility analyzer (RDMA), where they are classified based on their electrical mobility. Subsequently, the particles are directed into the condenser of a condensation particle counter (CPC), where they are grown through the condensation of isopropyl alcohol (IPA) to sizes large enough to be picked up by the detector. The advantage of this particle detection technique allows for accurate detection of particles at both high and low concentrations, with the particle number detection limit ranging from 100 to 1000000 $\#/cm^3$. Nonetheless, concentrations of larger particles (> 0.42 µm) cannot be measured via the SMPS technique due to multiple charges per particle that may give rise to different particle sizes with the same electrical mobility, resulting in inaccurate measurements. Hence, in this study, the Nanoscan is largely used to detect particles with sizes ≤ 0.3 µm.
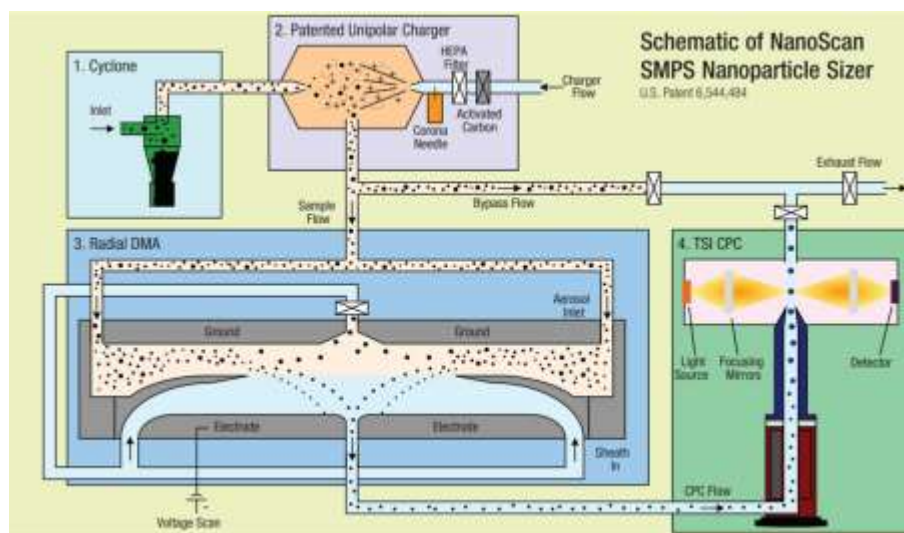
Figure 3. 7 Schematic diagram of the particle detection process of the Nanoscan SMPS 3910 (image from TSI).

3.4 Characterization Techniques

Several characterization techniques were adopted to characterized the 3 different types of filter designs introduced in Chapter 1. This section will briefly cover the basic working principles of the main techniques and justify why are they appropriate for characterizing the various relevant materials. Although not covered in this section, SEM, XRD and FTIR were also employed in this work.

3.4.1 Thermogravimetric Analysis (TGA)

For the lignin/GO and cellulose/lignin aerogels, thermogravimetric analysis (TGA) was used to measure the weight change over time with increasing temperature, which could provide information such as the thermal stability, phase transitions and the amount of volatile components of the material. These information are vital in determining the appropriate annealing temperature as well as understanding the cross-linking mechanisms. Generally, the TGA test is performed by placing the sample on a platinum pan and ramping up the temperature at a constant rate inside a furnace to incur a thermal reaction. Depending on the type of chemical reaction, different types of atmospheres can be employed such as synthetic air or inert gases. In this work, in order to study the thermal stabilities and cross-linking mechanisms of our aerogel materials, a supply of purified nitrogen (99.9995%) at a flow rate of 60 mL/min was used to maintain an inert atmosphere.

3.4.2 Differential Scanning Calorimetry

Since PLLA and PDLA would crystallize into SC-form with a melting temperature 50°C higher than that of the homopolymers, differential scanning calorimetry (DSC) was used to confirm the presence of SC-form as well as to investigate the blending efficacy of the two enantiomers. During the melting process, heat exchange would take place between the polymers and the environment, causing enthalpy changes within the polymer system. DSC is used to measure these enthalpy changes of the

sample as a function of temperature, allowing the melting temperature (T_m) to be accurately determined. This measurement can be achieved simply by determining the difference in heat flow between the sample and a reference when the temperature is increased at the same constant rate. Since the temperature of both the sample and reference are kept the same, during the melting process, more heat will flow to the sample as compared to the reference due to the occurrence of an endothermic process.

3.4.3 Mechanical Test

In air filtration applications, the filters are constantly being subjected to compression force from the air flow, hence it is important to design the aerogel material such that the three-dimensional structure can be reinforced at inter-fiber junctions (NFAs). In order to verify the reinforcement within the aerogel filters, tensile and compression tests were performed using a mechanical tester. For the PLLA/PDLA blend system, tensile tests were carried out with a 10N load cell, which was used to obtain the apparent tensile stress-strain curves of electrospun mats as a result of the stereocomplex formation and the strain rate was set at 9.5×10^{-3} /s. It is worth noting that electrospun mats were chosen for the easy clamping of sample during the tensile tests. Each mat was cut into a standard dumbbell shape according to the sample dimensions stated in ASTM D638-V. The same mechanical tester was also used to perform compression tests on cylindrical-shaped samples of the NFAs, and the compression rate adopted was 1.9×10^{-3} /s. The apparent compression moduli of the aerogels could be estimated from the initial, relatively straight parts of the compression curves (strain < 20-30%).

References

1.   Vink, E. T.; Rabago, K. R.; Glassner, D. A.; Gruber, P. R., Applications of life cycle assessment to NatureWorks™ polylactide (PLA) production. *Polymer Degradation and stability* **2003,** *80* (3), 403-419.

2.   Sin, L. T., *Polylactic acid: PLA biopolymer technology and applications*. William Andrew: 2012.

3.   Nagarajan, V.; Mohanty, A. K.; Misra, M., Perspective on polylactic acid (PLA) based sustainable materials for durable applications: Focus on toughness and heat resistance. *ACS Sustainable Chemistry & Engineering* **2016,** *4* (6), 2899-2916.

4.   Casasola, R.; Thomas, N. L.; Trybala, A.; Georgiadou, S., Electrospun poly lactic acid (PLA) fibres: Effect of different solvent systems on fibre morphology and diameter. *Polymer* **2014,** *55* (18), 4728-4737.

5.   Miguel, S. P.; Figueira, D. R.; Simões, D.; Ribeiro, M. P.; Coutinho, P.; Ferreira, P.; Correia, I. J., Electrospun polymeric nanofibres as wound dressings: A review. *Colloids and surfaces B: Biointerfaces* **2018,** *169*, 60-71.

6.   Li, D.; Frey, M. W.; Baeumner, A. J., Electrospun polylactic acid nanofiber membranes as substrates for biosensor assemblies. *Journal of Membrane Science* **2006,** *279* (1-2), 354-363.

7.   Cartier, L.; Okihara, T.; Ikada, Y.; Tsuji, H.; Puiggali, J.; Lotz, B., Epitaxial crystallization and crystalline polymorphism of polylactides. *Polymer* **2000,** *41* (25), 8909-8919.

8.   Lin, T. T.; Liu, X. Y.; He, C., A DFT study on poly (lactic acid) polymorphs. *Polymer* **2010,** *51* (12), 2779-2785.

9.   Fundador, N. G. V.; Takemura, A.; Iwata, T., Structural Properties and Enzymatic Degradation Behavior of PLLA and Stereocomplexed PLA Nanofibers. *Macromolecular Materials and Engineering* **2010,** *295* (9), 865-871.

10.   Muiruri, J. K.; Liu, S.; Teo, W. S.; Kong, J.; He, C., Highly biodegradable and tough polylactic acid–cellulose nanocrystal composite. *ACS Sustainable Chemistry & Engineering* **2017,** *5* (5), 3929-3937.

11.   Li, Z.; Muiruri, J. K.; Thitsartarn, W.; Zhang, X.; Tan, B. H.; He, C., Biodegradable silica rubber core-shell nanoparticles and their stereocomplex for efficient PLA toughening. *Composites Science and Technology* **2018,** *159*, 11-17.

12.   Ragauskas, A. J.; Beckham, G. T.; Biddy, M. J.; Chandra, R.; Chen, F.; Davis, M. F.; Davison, B. H.; Dixon, R. A.; Gilna, P.; Keller, M., Lignin valorization: improving lignin processing in the biorefinery. *science* **2014,** *344* (6185).

13.   Calvo-Flores, F. G.; Dobado, J. A., Lignin as renewable raw material. *ChemSusChem* **2010,** *3* (11), 1227-1235.

14.   Lee, J. G.; Larive, L. L.; Valsaraj, K. T.; Bharti, B., Binding of lignin nanoparticles at oil–water interfaces: an ecofriendly alternative to oil spill recovery. *ACS applied materials & interfaces* **2018,** *10* (49), 43282-43289.

15.   Stiefel, S.; Schmitz, A.; Peters, J.; Di Marino, D.; Wessling, M., An integrated electrochemical process to convert lignin to value-added products under mild conditions. *Green Chemistry* **2016,** *18* (18), 4999-5007.

16.   Upton, B. M.; Kasko, A. M., Strategies for the conversion of lignin to high-value polymeric materials: review and perspective. *Chemical reviews* **2015,** *116* (4), 2275-2306.

17.   Pakula, T.; Trznadel, M., Thermally stimulated shrinkage forces in oriented polymers: 1. Temperature dependence. *Polymer* **1985,** *26* (7), 1011-1018.

18.   Trznadel, M.; Kryszewski, M., Thermal shrinkage of oriented polymers. *Journal of Macromolecular Science, Part C: Polymer Reviews* **1992,** *32* (3-4), 259-300.

19.   Zhu, Y.; Murali, S.; Cai, W.; Li, X.; Suk, J. W.; Potts, J. R.; Ruoff, R. S., Graphene and graphene oxide: synthesis, properties, and applications. *Advanced materials* **2010,** *22* (35), 3906-3924.

20.   Lavoine, N.; Desloges, I.; Bras, J., Microfibrillated cellulose coatings as new release systems for active packaging. *Carbohydrate polymers* **2014,** *103*, 528-537.

21.   Costa, S. M.; Mazzola, P. G.; Silva, J. C.; Pahl, R.; Pessoa Jr, A.; Costa, S. A., Use of sugar cane straw as a source of cellulose for textile fiber production. *Industrial Crops and Products* **2013,** *42*, 189-194.

22.   Osong, S. H.; Norgren, S.; Engstrand, P., Processing of wood-based microfibrillated cellulose and nanofibrillated cellulose, and applications relating to papermaking: a review. *Cellulose* **2016,** *23* (1), 93-123.

23.   Ifelebuegu, A. O.; Johnson, A., Nonconventional low-cost cellulose-and keratin-based biopolymeric sorbents for oil/water separation and spill cleanup: A review. *Critical Reviews in Environmental Science and Technology* **2017,** *47* (11), 964-1001.

24.   Liu, H.; Geng, B.; Chen, Y.; Wang, H., Review on the aerogel-type oil sorbents derived from nanocellulose. *ACS Sustainable Chemistry & Engineering* **2016,** *5* (1), 49-66.

25.   Frey, M. W., Electrospinning cellulose and cellulose derivatives. *Polymer Reviews* **2008,** *48* (2), 378-391.

26.   Ahn, Y.; Hu, D.-H.; Hong, J. H.; Lee, S. H.; Kim, H. J.; Kim, H., Effect of co-solvent on the spinnability and properties of electrospun cellulose nanofiber. *Carbohydrate polymers* **2012,** *89* (2), 340-345.

27.   Sun, B.; Long, Y. Z.; Zhang, H. D.; Li, M. M.; Duvail, J. L.; Jiang, X. Y.; Yin, H. L., Advances in three-dimensional nanofibrous macrostructures via electrospinning. *Progress in Polymer Science* **2014,** *39* (5), 862-890.

28.   Gutiérrez, M. C.; Ferrer, M. L.; del Monte, F., Ice-templated materials: Sophisticated structures exhibiting enhanced functionalities obtained after unidirectional freezing and ice-segregation-induced self-assembly. *Chemistry of Materials* **2008,** *20* (3), 634-648.

29.   Scotti, K. L.; Dunand, D. C., Freeze casting–A review of processing, microstructure and properties via the open data repository, FreezeCasting. net. *Progress in Materials Science* **2018,** *94*, 243-305.

30.   Yan, J.; Wang, Q.; Wei, T.; Jiang, L.; Zhang, M.; Jing, X.; Fan, Z., Template-assisted low temperature synthesis of functionalized graphene for ultrahigh volumetric performance supercapacitors. *Acs Nano* **2014,** *8* (5), 4720-4729.

31.   Liu, X.; Ma, P. X., Phase separation, pore structure, and properties of nanofibrous gelatin scaffolds. *Biomaterials* **2009,** *30* (25), 4094-4103.

32.   Hassan, M. A.; Yeom, B. Y.; Wilkie, A.; Pourdeyhimi, B.; Khan, S. A., Fabrication of nanofiber meltblown membranes and their filtration properties. *Journal of Membrane Science* **2013,** *427*, 336-344.

33.   Soltani, I.; Macosko, C. W., Influence of rheology and surface properties on morphology of nanofibers derived from islands-in-the-sea meltblown nonwovens. *Polymer* **2018,** *145*, 21-30.

34.   Xue, J.; Wu, T.; Dai, Y.; Xia, Y., Electrospinning and electrospun nanofibers: methods, materials, and applications. *Chemical reviews* **2019,** *119* (8), 5298-5415.

35.   Taylor, G. I., Disintegration of water drops in an electric field. *Proceedings of the Royal Society of London. Series A. Mathematical and Physical Sciences* **1964,** *280* (1382), 383-397.

36.   Zhang, S.; Sun, J.; Hu, D.; Xiao, C.; Zhuo, Q.; Wang, J.; Qin, C.; Dai, L., Large-sized graphene oxide/modified tourmaline nanoparticle aerogel with stable honeycomb-like structure for high-efficiency PM 2.5 capture. *Journal of Materials Chemistry A* **2018,** *6* (33), 16139-16148.

37.   Lee, Y.; Park, S. H.; Kim, K. B.; Lee, J. K., Fabrication of hierarchical structures on a polymer surface to mimic natural superhydrophobic surfaces. *Advanced materials* **2007,** *19* (17), 2330-2335.

38.   Kresge, C.; Leonowicz, M.; Roth, W. J.; Vartuli, J.; Beck, J., Ordered mesoporous molecular sieves synthesized by a liquid-crystal template mechanism. *nature* **1992,** *359* (6397), 710-712.

39.   Liang, Z.; Pei, Y.; Chen, C.; Jiang, B.; Yao, Y.; Xie, H.; Jiao, M.; Chen, G.; Li, T.; Yang, B., General, Vertical, Three-Dimensional Printing of Two-Dimensional Materials with Multiscale Alignment. *ACS nano* **2019,** *13* (11), 12653-12661.

40.   Zhang, C.; Mcadams, D. A.; Grunlan, J. C., Nano/Micro-Manufacturing of Bioinspired Materials: a Review of Methods to Mimic Natural Structures. *Advanced Materials* **2016,** *28* (30), 6292-6321.

41.   See, S. W.; Balasubramanian, R.; Wang, W., A study of the physical, chemical, and optical properties of ambient aerosol particles in Southeast Asia

during hazy and nonhazy days. *Journal of Geophysical Research: Atmospheres* **2006,** *111* (D10), n/a-n/a.

42.   Lin, T.-C.; Krishnaswamy, G.; Chi, D. S., Incense smoke: clinical, structural and molecular effects on airway disease. *Clinical and Molecular Allergy* **2008,** *6* (1), 3.

43.   See, S. W.; Balasubramanian, R.; Rianawati, E.; Karthikeyan, S.; Streets, D. G., Characterization and source apportionment of particulate matter≤ 2.5 μm in Sumatra, Indonesia, during a recent peat fire episode. *Environmental science & technology* **2007,** *41* (10), 3488-3494.

44.   Betha, R.; Behera, S. N.; Balasubramanian, R., 2013 Southeast Asian Smoke Haze: Fractionation of Particulate-Bound Elements and Associated Health Risk. *Environmental Science & Technology* **2014,** *48* (8), 4327-4335.

45.   Wang, X.; Chen, J.; Cheng, T.; Zhang, R.; Wang, X., Particle number concentration, size distribution and chemical composition during haze and photochemical smog episodes in Shanghai. *Journal of Environmental Sciences* **2014,** *26* (9), 1894-1902.

46.   Kwasny, F.; Madl, P.; Hofmann, W., Correlation of air quality data to ultrafine particles (UFP) concentration and size distribution in ambient air. *Atmosphere* **2010,** *1* (1), 3-14.

47.   Tiwari, M.; Sahu, S. K.; Bhangare, R. C.; Yousaf, A.; Pandit, G. G., Particle size distributions of ultrafine combustion aerosols generated from household fuels. *Atmospheric Pollution Research* **2014,** *5* (1), 145-150.

Chapter 4

Highly porous polymer nanofibrous areogels cross-linked via spontaneous inter-fiber stereocomplexation and their potential for capturing ultrafine airborne particles

In this chapter, the fabrication of stable, highly porous PLLA/PDLA blend nanofibrous aerogels (NFAs) cross-linked via spontaneous inter-fiber stereocomplexation and their potential as air filters for capturing ultrafine particles are reported. It is revealed that the extent of cross-linking can be easily controlled by adjusting the molecular weights of the polymers and their ratio. It was also verified via compression tests that the PLLA/PDLA blend NFAs exhibit significantly higher compressive resistance than their PLLA counterparts, demonstrating the effectiveness of the cross-linking. When combined with a layer of HEPA filter to form a composite filter, the NFAs show the potential to significantly improve the filtration efficiency for ultrafine particles with a slight increase in pressure drop (ΔP). The results suggest that the small increase in ΔP is largely due to the high porosity of the NFAs and the slip flow effect of nanofibers, while the enhanced filtration efficiency could be attributed to the greater thickness of the NFAs that leads to increased residence time of the ultrafine particles. This unique approach to spontaneously cross-link electrospun nanofibers may also be applied to other stereocomplex systems or used for applications in other fields.

*This chapter was published substantially as reference: **Ma, X. Y. D.**; Ang, J. M.; Zhang, Y.; Zeng, Z.; Zhao, C.; Chen, F.; Ng, B. F.; Wan, M. P.; Wong, S.-C.; Li, Z., Highly porous polymer nanofibrous aerogels cross-linked via spontaneous inter-fiber stereocomplexation and their potential for capturing ultrafine airborne particles. *Polymer* **2019,** *179*, 121649.

4.1 Introduction

As introduced in Chapter 2, ultrafine particles make up a large portion of airborne PM and their harmful impacts can be detrimental to human health [1-3]. Thus, it is necessary to develop air filtration technologies to improve the air quality of the environment. 2D fibrous filters have emerged as the popular choice of air filters due to their low production cost, high efficiency and ease of fabrication [4-6]. It is widely reported that ultrafine particles are trapped in fibrous media mainly via the diffusion mechanism, which largely relies on the strong Brownian behavior of these small particles to impinge onto the fiber surface [7-8]. However, improved diffusion capture of ultrafine particles is often achieved with higher fiber packing density [9-13], which would give rise to a surge in ΔP that causes high energy consumption. Thus, there exists a trade-off relationship between filtration efficiency and ΔP. In order to address this problem, the concept of 3D air filtration using nanofibrous aerogel (NFA) filters was introduced [14-16]; the large internal volume of NFAs could enhance the diffusion capture of ultrafine particles while at the same time, the high porosity could ease the airflow and reduce ΔP. Several techniques have been reported in attempts to fabricate "3D" nanofibrous macrostructures [17-22]. Nonetheless, due to the absence of strong inter-fiber interactions, such NFAs often have poor structural integrity and weak mechanical properties that could result in the collapse of the structure into denser ones when subjected to compressive forces of the airflow. Therefore, it is necessary to develop a facile cross-linking approach to reinforce the 3D structure at fiber touching points, such that highly robust NFA filters can be fabricated for the efficient removal of ultrafine particles.

In Chapter 3, we mentioned that polylactic acid (PLA) is a well-known synthetic polymer capable of forming a polymer stereocomplex, which is a stable composite of two stereoregular polymers (PLLA and PDLA) with complementary helical conformations that can interlock each other by stereoselective interactions. Studies have shown that the PLLA/PDLA stereocomplex (PLLA/PDLA-SC) exhibited superior thermal and mechanical properties to their homopolymer counterparts [23-27].

When L and D stereoisomers are present in the same system, stereocomplexation may occur in solutions or molten state [28]. Both solution-spun and melt-spun PLLA/PDLA blend fibers [29-31], including electrospun nanofibers [32-33], have been reported to show improved properties, such as significantly enhanced tensile strength and Young's modulus, compared with corresponding PLA fibers. Recently, Jing et. al also reported that annealing electrospun PLLA/PDLA blend nanofibrous mats below the melting temperature could induce the formation of fiber junctions, leading to more robust nanofibrous mats [33]. Since as-spun electrospun nanofibers are frequently at a slightly wet state, an interesting question is whether the as-spun nanofibers can form inter-fiber junctions spontaneously without thermal or other form of stimuli. So far, the question has not been addressed although the spontaneous formation of inter-fiber junctions may greatly improve the structural stability of nanofibrous macrostructures, benefiting their applications in many fields.

To address the aforementioned issues, in this work, for the first time the stereocomplexation approach was demonstrated to spontaneously create fiber junctions in highly porous 3D NFAs formed by PLLA/PDLA blend nanofibers. Differently, in this work PLLA/PDLA-SC fiber junctions were spontaneously formed in the NFA fabrication process, which, combined with the favorable mechanical properties of the PLLA/PDLA blend fibers, could enhance the compression resistance of the highly porous NFAs and prevent them from collapsing in applications. To demonstrate the usefulness of this approach, a highly porous PLLA/PDLA-SC NFA, which could act as a 3D filter, was combined with a HEPA filter. Herein, the composite filter was revealed to exhibit enhanced filtration efficiency for ultrafine particles with only a slight increase in pressure drop. This simple approach also provides a new generic route for fabrication of highly porous yet stable NFAs.

4.2 Experimental

4.2.1 Materials

PLLA with a weight-average molecular weight (M_w) of 9.12×10^4 g/mol was purchased from Nature Works, Ltd., USA. PLLA with higher M_w (1.20×10^5 g/mol and 1.50×10^5 g/mol) and PDLA with M_w of 3.98×10^4 g/mol were purchased from Changchun Foliaplast, Bio-Tech Co., Ltd, China. Dichloromethane and N,N-dimethylformamide were obtained from Fisher Scientific, Singapore. Tetrabutylammonium chloride and tertiary-butanol were purchased from Sigma-Aldrich Pte Ltd, Singapore. All chemicals were used as received. High-efficiency air filtration materials were supplied by Fushun Shunhua Auto Parts Manufacturing Co Ltd, China.

4.2.2 Preparation of PLLA/PDLA Blend Solution for Optimization

PLLA (9.18×10^4 g/mol) and PDLA with a ratio of 1:1 was dissolved in dichloromethane at various concentrations (8, 10, 13 wt%) and left to stir for 2 h under room conditions, followed by the addition of N,N-dimethylformamide. The DCM/DMF ratio was fixed at 8:2 for the 8 and 13wt% PLLA/PDLA blend solution while the DCM/DMF ratio was varied from 6:4 to 9:1 for the 10wt% solution. PLLA with higher M_w (1.20×10^5 and 1.50×10^6 g/mol) were also used to prepare 10wt% PLLA/PDLA blend solutions (ratio 1:1) to study the M_w effect on the gelation time.

4.2.3 Fabrication of 3D Electrospun NFA

10 wt% PLLA/PDLA-SC solutions were prepared by first dissolving the blend of PLLA/PDLA in dichloromethane with varied weight ratios (1:1, 3:7, 7:3). The solutions were left to stir under room temperature for 2 h followed by the addition of N,N-dimethylformamide with a fixed DCM/DMF ratio (8:2, w/w). 10wt% of PLLA solution was also prepared as a reference. 0.5 wt% (relative to total polymer weight) tetrabutylammonium chloride (TBAC) was added to each solution to

improve the conductivity for electrospinning. The electrospinning was carried out at the feed rate of 0.7mL/h, voltage of 17kV and working distance of 15 cm. The electrospun fibers were collected on a wire mesh submerged in tertiary butanol and then left to freeze in a refrigerator followed by freeze-drying to obtain thin layers of 3D NFAs. The electrospun fibers were also directly collected in ethanol and freeze-dried in a mold to obtain cylindrical-shaped NFAs for density and mechanical measurements. PLLA and PLLA/PDLA-SC nanofibrous mats were also electrospun directly onto wire mesh as reference samples.

4.2.4 Characterization

The morphology of the nanofibrous filters was studied with a field emission scanning electron microscopy (FESEM, JEOL 6340) at an acceleration voltage of 5kV. The densities of the aerogels were estimated by evaluating the weighed mass and measured dimensions of the cylindrical-shaped aerogels. Porosity was estimated from the ratio between the densities of the NFAs and bulk PLA polymer (Porosity = $1 - \rho_{NFA} / \rho_{polymer}$; ρ_{PLA} = 1.210-1.430 g cm^{-3}, ρ_{glass} = 2.6 g cm^{-3}). A tensile tester (Instron 5567) with a 10N load cell was used to obtain apparent tensile stress-strain curves of as-spun PLLA and PLLA/PDLA-SC electrospun mats and the strain rate was set at 9.5×10^{-3} /s. Each mat was cut into a standard dumbbell shape according to sample dimensions stated in ASTM D638-V. The same Instron machine was also used to perform compression tests on the cylindrical-shaped samples and the compression rate adopted was 1.9×10^{-3} /s. An X-ray diffractometer (XRD, Bruker D8 Discover) with Cu Kα (λ = 0.15406 nm) radiation and differential scanning calorimetry (DSC, TA instruments Q10) were used to verify the formation of PLLA/PDLA-SC within the nanofibers.

4.2.5 Filtration test

As mentioned in Chapter 3, in this study, the model haze particles were generated and the PM$_{2.5}$ concentration was controlled by diluting with air in the mixing

chamber, down to a concentration equivalent to a hazardous pollution level of ~300 $\mu g/m^3$. The model haze particles were created via two ways that is either through the burning of incense or an aerosol generator (SLG 250, TOPAS), which utilizes diethylhexyl sebacate (DEHS) as the aerosol particles. The particle concentration was measured with an optical particle sizer (OPS 3330, TSI Instruments Ld) and a condensation particle counter (NanoScan SMPS 3910, TSI Instruments Ld), while the filtration efficiency can be calculated by comparing the upstream and downstream particle number concentrations of the aerogel filters. The pressure drop was measured using a differential pressure gauge (Digital Manometer, Bluewind Laboratory Pte Ltd). The face velocity used in the filtration testing was 10 cm/s and measured by an air velocity meter (Airflow instruments velocity meter TA430, TSI Instruments Ld). Stability tests were carried out under a constant compressive force (face velocity = 10 cm/s) for 24h at relative humidity (RH) of 60% and 90%. Unless otherwise stated, the humidity was 60% RH for all filtration tests.

4.3 Results and Discussion

4.3.1 PLLA/PDLA Stereocomplexation in Blend Solution

Since stereocomplexation can occur in solution- or molten- states, in this work, it can occur within the PLLA/PDLA blend and during the electrospinning process. Under certain favorable conditions, the stereocomplexation could cause gelation of the as-prepared PLLA/PDLA blend solutions [34-35]. Gelation would result in the formation of non-uniform beaded fibers, which could lead to poor mechanical properties. Hence, solution parameters of the PLLA/PDLA blend solution, such as the solvent ratio and molecular weight of the polymers have to be optimized to prolong the onset of gelation of the blend solutions.

Generally, the purpose of using a binary solvent in a PLLA/PDLA blend system is to precipitate the stereocomplex and by doing so, promotes the intermolecular interactions responsible for the formation of stable stereocomplex crystals [35]. However, stereocomplexation would result in the gelation of the blend, which

interferes with the electrospinning process. Therefore, the solvent ratio of the binary solvent should be optimized to prepare a stable PLLA/PDLA blend solution for electrospinning. To study the effects of solvent ratio on the gelation, DCM/DMF ratio was varied from 6:4 to 9:1, while keeping the total PLLA/PDLA concentration at 10 wt%. DCM is a good solvent for dissolving the PLLA/PDLA blend but a poor solvent for electrospinning due to its poor conductivity and low boiling point. On the other hand, DMF is a poor solvent to dissolve the blend but a good electrospinning solvent (high conductivity and boiling point). Hence, the higher the DMF ratio used, thinner and smoother nanofibers can be obtained. However, when the DCM/DMF ratios of 6:4 and 7:3 were used, it was found that the gelation of PLLA/PDLA blend solution occurred within tens of minutes to an hour (due to stereocomplexation), which made it impossible to spin a substantial amount of fibers enough to fabricate the NFAs. Alternatively, when DCM/DMF ratio of 9:1 was used, the onset of gelation for the PLLA/PDLA blend solution took a much longer time (up to several hours) but the spinneret needle tip often gets blocked due to the high evaporation rate of DCM. Thus, the optimum DCM/DMF ratio was determined to be 8:2, at which sufficient time for electrospinning is provided to obtain thin and smooth nanofibers for fabricating the NFAs.

The effects of molecular weight of PLLA and PDLA on the gelation time was also investigated. It was found that this polymer system is very sensitive to the change in molecular weight and these changes can in turn affect the spinnability of the PLLA/PDLA blend solution as well as the morphology of the nanofibers. When PLLA with higher M_w are used (1.20×10^5 and 1.50×10^6 g/mol), the gelation time of the solution, as a result of the stereocomplex formation, becomes too short and there is insufficient time to collect a substantial amount of electrospun nanofibers. Furthermore, the onset of gelation for the PLLA/PDLA blend solution increases with increasing M_w, which could be attributed to the strong polymer chain entanglements. On the other hand, by incorporating PLLA of lower molecular weight (9.18×10^4 g/mol) into the blend solution, the onset of gelation can be delayed up to several hours. Nonetheless, it is worthy to note that polymer with very low M_w would also

lead to the formation of beaded fibers. Therefore, in the subsequent studies, PLLA with M_w of 9.18×10^4 g/mol was chosen to prepare the PLLA/PDLA blend solution for the electrospinning process.

4.3.2 Evidence for Inter-fiber PLLA/PDLA Stereocomplexation

With the optimized PLLA/PDLA blend solution parameters determined, highly porous NFAs were fabricated by liquid collection of electrospun PLLA and PLLA/PDLA blend nanofibers followed by feeze-drying (Figure 4.1). Since PLLA and PDLA could form stereocomplex in solutions, we hypothesized that when wet electrospun PLLA/PDLA blend nanofibers come into contact in fiber collection and freeze-drying processes, spontaneous stereocomplexation would take place between PLLA and PDLA chains on the neighboring fiber surface, resulting in the agglutination of the nanofibers, as illustrated in Figure 4.2a. To verify this hypothesis, morphologies of the NFAs were examined under FESEM (Figures 4.2b and c). As seen in Figures 4.2b and c, no severe bundling of fibers was observed in the PLLA NFA, although slight bundling was observed probably because the bio-synthesized PLLA used in this work contained a very small amount of D-stereoisomers and hence inter-fiber stereocomplexation may still occur to a small extent. By contrast, the NFA made from the blend with PLLA/PDLA weight ratio of 5/5 (PLLA/PDLA-5/5) shows larger fiber junctions consisting of several fibers due to the higher extent of inter-fiber stereocomplexation (Figures 4.2d and e). It is expected that the fiber junctions could act as cross-linking points to improve compression resistance of the NFA, which combined with the higher modulus of PLLA/PDLA-SC crystals within the fibers (Figure 4.2a), could help highly porous morphology of the NFA be better retained in applications. XRD and DSC studies show that PLLA/PDLA-5/5 nanofibers exhibit distinct XRD and DSC melting peaks corresponding to PLLA/PDLA-SC, whereas these peaks do not appear for PLLA nanofibers (Figure 4.3). However, we are unable to distinguish between inter-fiber stereocomplex and that formed within the fibers. Thus another strategy was designed

to further verify the spotaneous inter-fiber stereocomplexation, which is elaborated below.
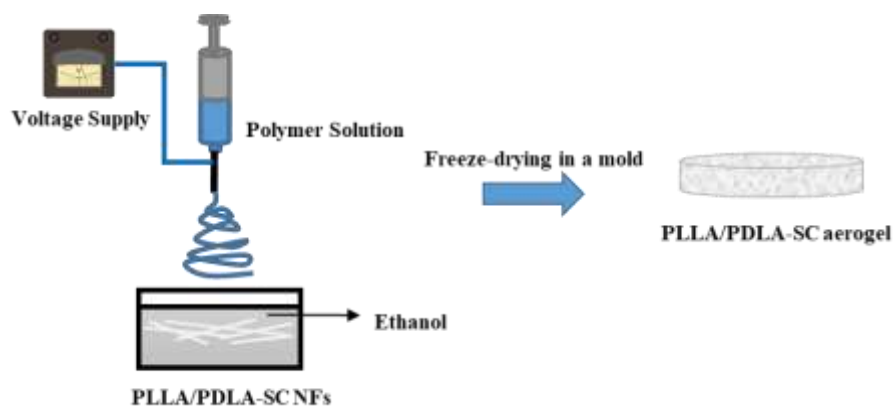
Figure 4. 1 Schematic diagram of the electrospinning setup used to fabricate 3D PLLA/PDLA-SC NFAs.
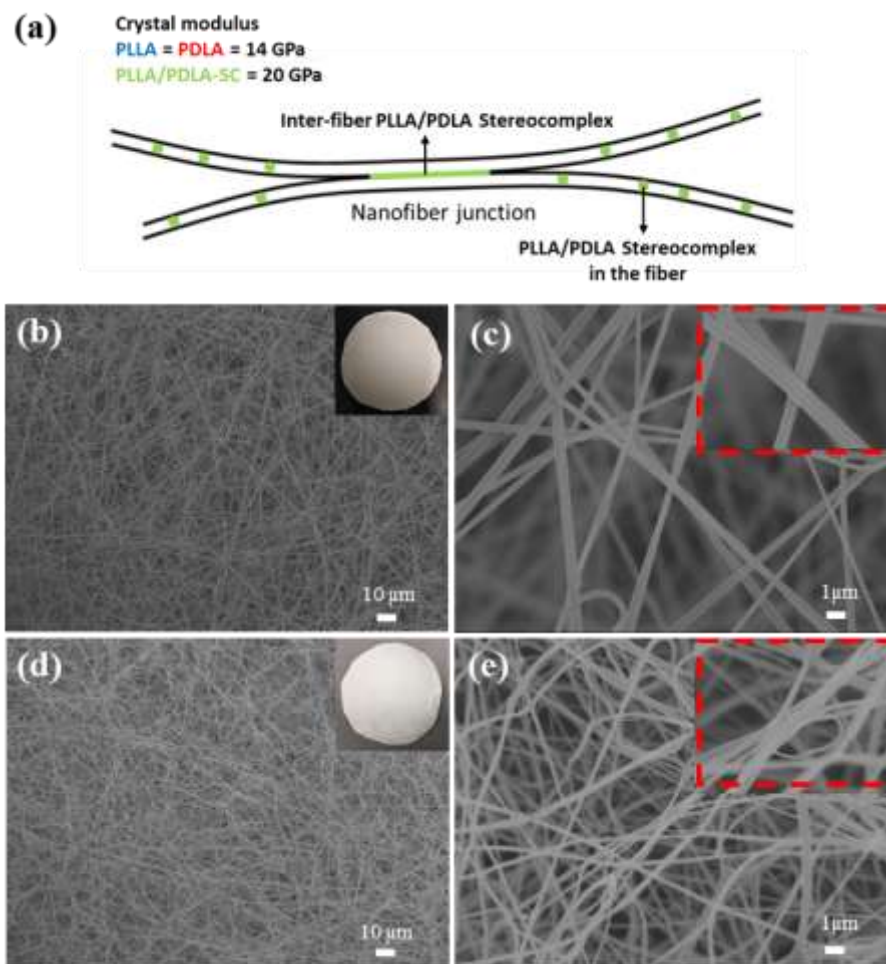
Figure 4. 2 (a) A schematic illustrating inter-fiber stereocomplexation-induced agglutination of nanofibers and the crystal moduli of PLLA, PDLA and PLLA/PDLA-SC [36]. FESEM micrographs of (b, c) PLLA and (d, e) PLLA/PDLA-5/5 NFAs. The insets in (b) and (d) are the digital pictures of PLLA and PLLA/PDLA-SC NFAs supported on wire mesh, respectively.
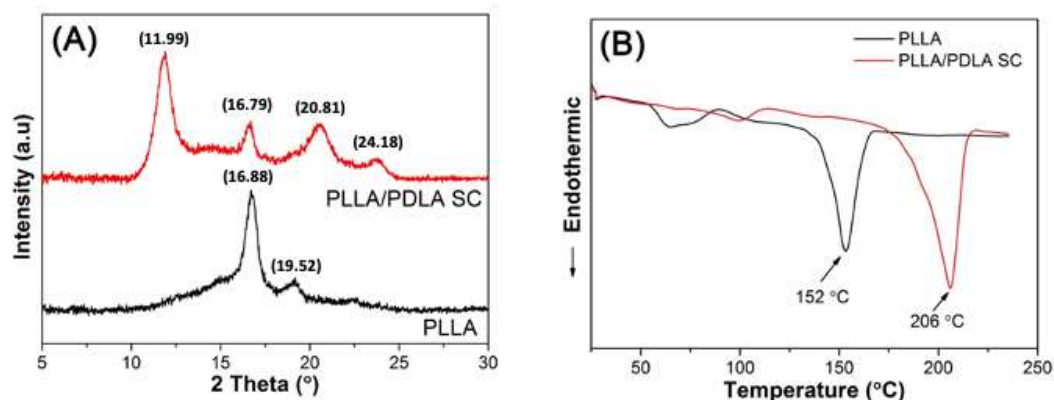
Figure 4. 3 Crystallinity behavior and thermal stability analysis of electrospun PLLA and PLLA/PDLA SC nanofibrous structure by (a) XRD and (b) DSC.

The extent of inter-fiber stereocomplexation may be related to the number of free chain ends on the nanofiber surface because with free ends, chain segments on a fiber surface could adjust their conformations more easily to form stereocomplex with appropriate chain segments on a neighboring fiber surface. Hence, if there are more free chain ends available for cross-linking via stereocomplexation, the cross-linking density will increase, which may enhance the robustness of the NFAs but at the same time, reduce their specific surface area slightly due to fiber merging. A lower-molecular-weight polymer (shorter chains) has more chain ends per unit mass than the corresponding higher-molecular-weight polymer, implying that the extent of inter-fiber stereocomplexation may be influenced by the molecular weights of the two stereoisomers. Thus, to further verify the spontaneous cross-linking via stereocomplexation, we mixed a high-molecular-weight (9.12×10^4 g mol^{-1}) PLLA with a low-molecular-weight (3.98×10^4 g mol^{-1}) PDLA, and the PLLA/PDLA mass ratio was varied from 7/3 to 3/7. The influence of the composition on the extent of inter-fiber stereocomplexation is shown in Figure 4.4. The PLLA/PDLA-7/3 NFA displays very limited agglutination of fibers (Figure 4.4a), which is due to its higher content of high-molecular-weight PLLA and hence lower density of free chain ends, giving rise to a smaller extent of inter-fiber stereocomplexation. By contrast, the PLLA/PDLA-3/7 NFA, which is comprised of a higher content of lower-molecular-weight PDLA, has higher density of free chain ends, resulting in a greater extent of

inter-fiber stereocomplexation and strong inter-fiber junctions, i.e., larger bundles of several fibers are formed (Figure 4.4b). This observation provides further evidence for the formation of fiber junctions via inter-fiber complexation. Moreover, it allows us to control the morphology of PLLA/PDLA blend NFAs easily.
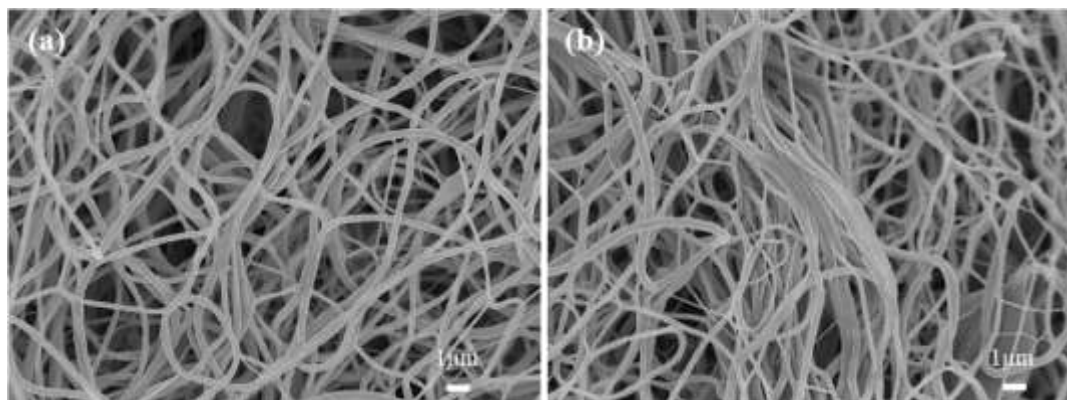
Figure 4. 4 FESEM micrographs of (a) PLLA/PDLA-7/3, and (b) PLLA/PDLA-3/7 NFAs.

4.3.3 Effects of Inter-fiber Stereocomplexation on Mechanical Behaviors

In order to demonstrate that the inter-fiber stereocomplexation can lead to effective cross-linking, tensile tests were carried out on as-spun PLLA and PLLA/PDLA-5/5 nanofibrous mats, which are much denser than NFAs, to facilitate easy clamping of the samples. It should also be highlighted that the nanofibrous mats prepared for tensile tests were electrospun without the addition of TBAC, such that the fiber diameters are generally larger. The morphologies of the mats were observed under FESEM before and after the tests, as presented in Figure 4.5. It is worth noting that the tensile curves presented in Figure 4.5e could not provide the actual tensile properties of the materials but rather the apparent tensile strength and elongation at break, which were calculated based on the overall dimensions of the electrospun nanofibrous samples. The poor inter-fiber interactions in the PLLA mats cause initially 2D randomly oriented nanofibers to align along the tensile force applied (Figure 4.5a and b), leading to a large apparent strain before fiber breakage (Figure

4.5e, PLLA curve), and such morphological change is irreversible. On the contrary, the strong fiber junctions due to inter-fiber stereocomplexation hinders the fiber aligning along the tensile force, leading to the breakage of the PLLA/PDLA-5/5 mats at a much smaller apparent elongation (Figure 4.5e, PLLA/PDLA SC curve) with the random morphology well retained after the tensile test (Figure 4.5c and d). The above results, although not quantitative, show that the fiber junctions formed via inter-fiber stereocomplexation is sufficiently strong to retain the morphology of the as-spun PLLA/PDLA-5/5 mats under tensile force.
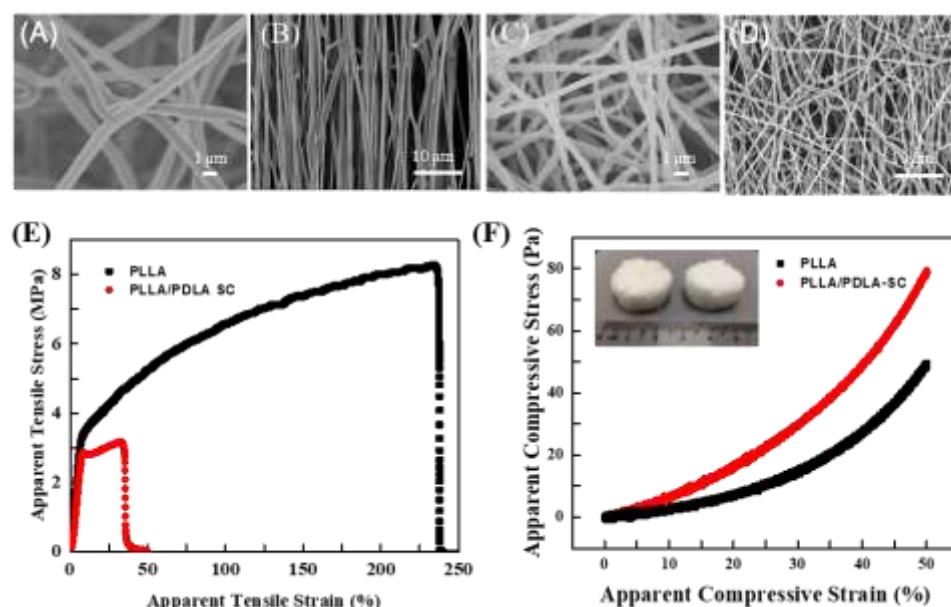
Figure 4. 5 FESEM micrographs of electrospun nanofibrous mats of (a, b) PLLA and (c, d) PLLA/PDLA-5/5 before and after tensile tests. (e) Typical apparent tensile curves of PLLA and PLLA/PDLA-5/5 electrospun nanofibrous mats. (f) Typical apparent compression stress-strain curves of PLLA and PLLA/PDLA-5/5 NFAs. The inset in (f) is the digital picture of the PLLA (left) and PLLA/PDLA-5/5 (right) NFAs used in the compression tests.

Compression tests were also performed on the highly porous NFAs to evaluate their compression resistance. The aerogel heights before compression are also provided in Table 4.1 and all aerogels are subjected to 50 % strain. The apparent stress-strain

curves in Figure 4.5f show that the apparent compression stress of PLLA/PDLA-5/5 NFA is much lower than that of PLLA NFA at relatively low strains (<50%). The apparent compression moduli of the PLLA and PLLA/PDLA-5/5 NFA could be estimated from the initial, relatively straight parts of the compression curves (strain <20%). It shows that the apparent compression modulus of PLLA/PDLA-5/5 NFA (~0.90 Pa) is much greater than that of PLLA NFA (~0.40 Pa). Since the PLLA and PLLA/PDLA-5/5 NFA samples used in compression tests have similar fiber diameters and porosities (Table 4.2), it is believed that both the stronger fiber junctions formed via inter-fiber stereocomplexation and stiffer nanofibers caused by stereocomplexation within the fibers contribute to the enhanced compressive resistance of the PLLA/PDLA-5/5 NFA, demonstrating its potential for 3D air filtration.

Table 4. 1 Dimensions of the tested cylindrical samples for compression tests.

Sample	Height (mm)
PLLA NFA	10.43± 0.86
PLLA/PDLA-5/5 NFA	10.91± 1.35

Table 4. 2 The average fiber diameter, estimated density and porosity of PLLA and PLLA/PDLA-5/5 NFAs, PLLA/PDLA-5/5 electrospun mats and the reference HEPA filer.

Samples	Average fiber diameter (nm)	NFA density (mg/cm^3)	NFA Porosity (%)
PLLA NFA	349±89	3.29±0.35	99.8

PLLA/PDLA-5/5 NFA	287±93	2.48±0.15	99.8
PLLA/PDLA-5/5 Mats	236±83	96.00±7.54	92.1-93.3
HEPA	3400±1730	275.5	89.4

*PLLA/PDLA-5/5 mats are used for filtration test. The mats used for tensile test are not listed in this table.

4.3.4 Performance in Capturing Ultrafine Airborne Particles and Pressure Drop

The filtration efficiencies and pressure drops of the NFAs and reference samples were studied using model haze particles generated via burning of incense. As mentioned in Chapter 3, the reason for choosing incense as the model haze particles is due to the comparable size distribution and chemical composition of incense to the actual haze caused by biomass burning [1, 37-38]. The overall concentration of the pollutant particles (all < 2.5 µm) in the model gas is above 300 µg/m^3, which lies in the hazardous range under WHO guidelines.

Firstly, the filtration efficiency of a type of commercial HEPA filter material (denoted as HEPA) composed of micron-sized fibers was tested as a reference. The morphology of HEPA is presented in Figure 4.6, and the corresponding mean fiber diameter and estimated density are given in Table 4.1. Figure 4.7a shows filtration efficiencies of the filters composed of 1 layer (HEPA-1), 2 layers (HEPA-2), 3 layers (HEPA-3) of the HEPA filter, respectively. Generally, the overall filtration efficiency increases with the number of layers. HEPA-1 shows a low efficiency of 98.01% for PN$_{0.1}$. It is also worth noting that the filtration efficiency that is based on mass concentration tends to undermine the small particle size, hence the number concentration will be be a more precise factor to determine the filtration efficiency.

HEPA-2 and HEPA-3 display significantly higher $PN_{0.1}$ efficiencies of 99.24% and 99.65%, respectively. However, this improvement in filtration efficiency is accompanied by a proportional surge in pressure drop due to the amplified resistance to airflow (Figure 4.7b).
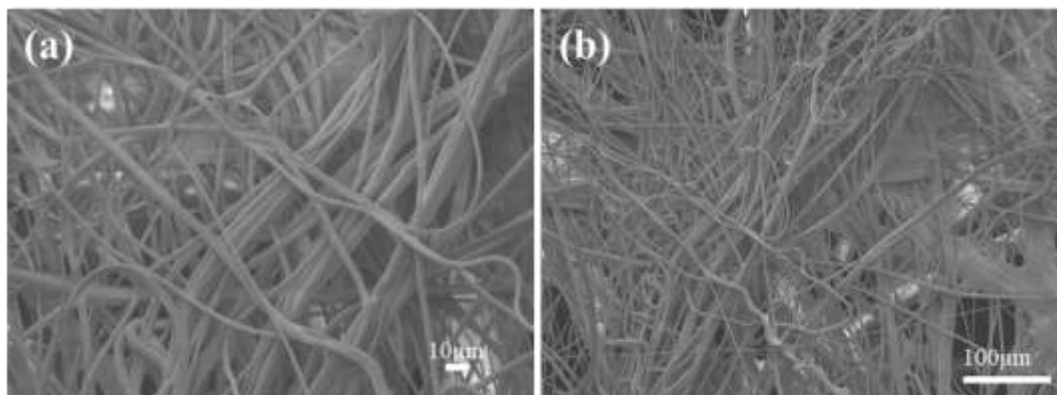
Figure 4. 6 FESEM micrographs of a typical reference commercial filter.

In air filtration industry, thin layers of nanofibrous mats have been integrated with commercial microfibrous filters. The purpose is to utilize their higher specific surface area and smaller pore sizes of the nanofibrous mats to increase diffusion and interception capture of sub-micron particles. Thus, in order to demonstrate the potential of the highly porous PLLA/PDLA-5/5 NFA for capturing ultrafine particles and overcoming the tradeoff between filtration efficiency and pressure drop, an electrospun PLLA/PDLA-5/5 nanofibrous mat with roughly the same mass was also prepared as a reference and the average basis weights are shown in Table 4.3. As shown in Table 4.1, the PLLA/PDLA-5/5 NFA has much higher porosity than the PLLA/PDLA-5/5 mat. The morphological difference between the two nanofibrous materials is further investigated using FESEM and the representative images of PLLA/PDLA-5/5 mat are shown in Figure 4.8. The nanofibers in the mats are observed to be stretched out and there is not much contrast between the topmost and bottom fibers due to their more compact packing. Differently, only the nanofibers on top can be clearly observed in the NFA and the nanofibers beneath look slightly fuzzy as their positions are significantly lower than the top layer, suggesting a looser

morphology. HEPA-1 was combined with a layer of PLLA/PDLA-5/5 electrospun mat and a layer of PLLA/PDLA-5/5 NFA, respectively, to form composite filters (HEPA-1-PLLA/PDLA-5/5 mat and HEPA-1-PLLA/PDLA-5/5 NFA). In Figure 4.7a and Table 4.4, we can see that the $PN_{0.1}$ and $PN_{0.5}$ filtration efficiencies of the two composite filters are noticeably higher than that of HEPA-1 and HEPA-2, and marginally higher than that HEPA-3. The typical average mass concentration (PM) and number concentration (PN), before and after filtration for HEPA-1 can be found in Table 4.5. It is intriguing that HEPA-1-PLLA/PDLA-5/5 NFA displays a higher $PN_{0.1}$ removal efficiency (99.83%) than HEPA-3 (99.65%), with pressure drop of the former (74.67 Pa) is almost half that of HEPA-3 (139.00 Pa) at a relatively high face velocity of 10 cm/s, which clearly shows that the 3D filter possesses superior filtration performance for ultrafine particles without sacrificing much of the pressure drop. The typical average PM and PN before and after filtration can be found in Table 4.6. As compared with HEPA-1, the $PM_{0.1}$ and $PN_{0.1}$ of the composite filter are significantly lower than that of HEPA-1, with the $PN_{0.1}$ value (9.79 x 10^2 #/cm^3) one tenth of the $PN_{0.1}$ of HEPA-1 (9.42 x 10^3 #/cm^3), which clearly demonstrated the high removal efficiency of ultrafine particles of the composite filter. The relatively low pressure drop exhibited by the PLLA/PDLA-5/5 NFA can be attributed to its ultrahigh porosity and slip flow effect on the nanofibers. Interestingly, when HEPA-1 is combined with the nanofibrous mat and highly porous NFA, the composite filters exhibit different filtration performance. HEPA-1-PLLA/PDLA-5/5 NFA possesses a higher removal efficiency for $PN_{0.1}$ and lower pressure drop as compared to HEPA-1-PLLA/PDLA-5/5 mat. This suggests significantly different filtration mechanisms for the nanofibrous mat and highly porous NFA. Despite being nanoporous, the mats are much denser, compromising the porosity, which results in large pressure drop and hence high energy consumption across the filter. Differently, in the NFA, the nanofibers are packed less compactly together, creating a highly porous filter and hence significantly reducing pressure drop. As illustrated in Figure 4.7ci, assuming that both the nanofibrous mat and highly porous NFA contain the same amount of fibers with similar fiber diameters, the NFA possesses a greater thickness. This is crucial in capturing ultrafine particles because residence time of these particles in

the filter is greatly increased and therefore, the likelihoods of these particles being adsorbed onto the fiber surface through Brownian motion will be greater, as illustrated in the schematic diagram in Figure 4.7cii.
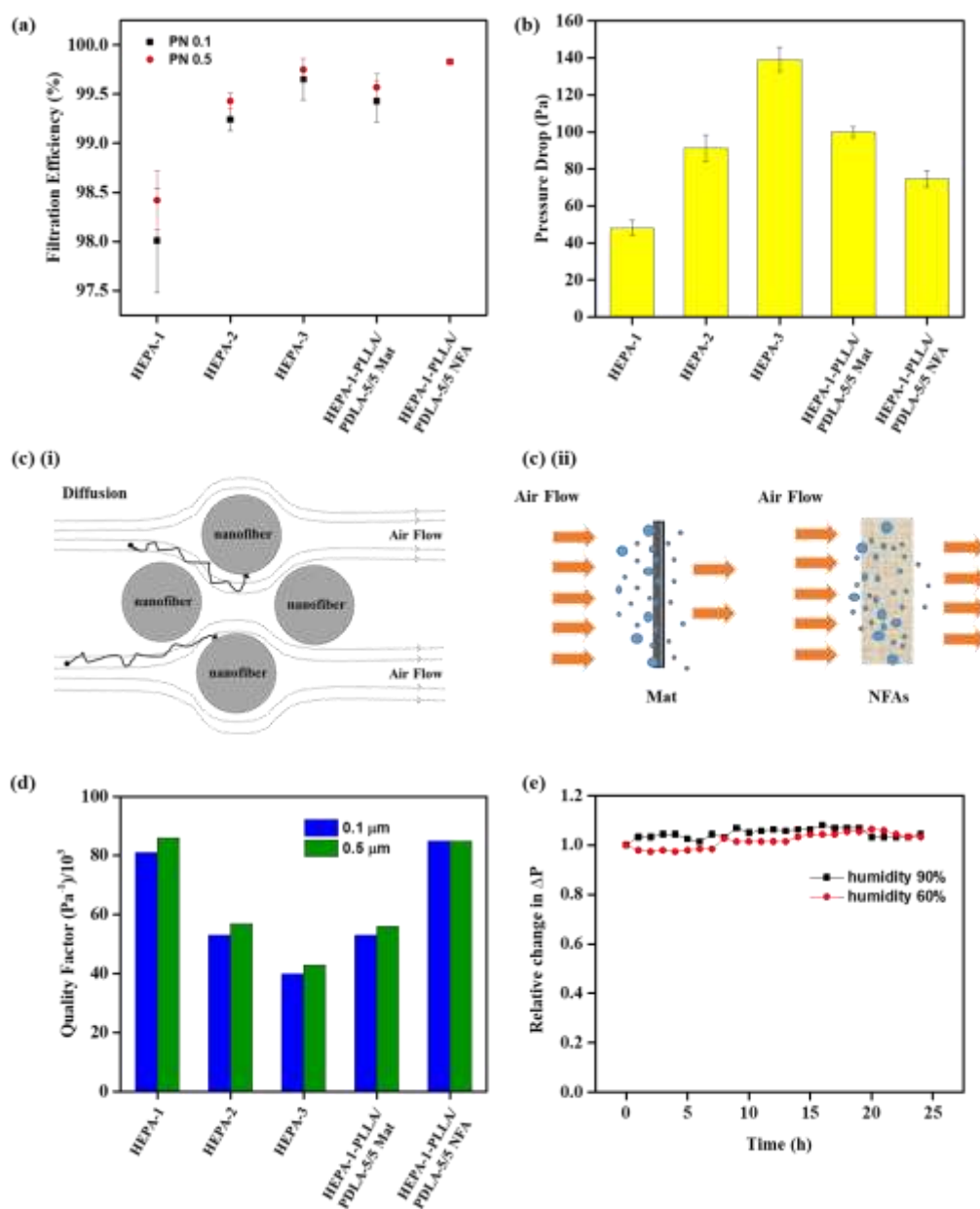
Figure 4. 7 (a) Filtration efficiencies, (b) pressure drop of different layers of HEPA filters and the combination of one layer of HEPA (HEPA-1) with PLLA/PDLA-5/5 mat and NFAs filters, respectively, using incense as aerosol particles (for HEPA-1-PLLA/PDLA-5/5 NFA, the points for $PN_{0.1}$ and $PN_{0.5}$ almost overlap). (c) Schematic

diagrams of (i) filtration diffusion mechanism and (ii) particle residence within the mat and NFAs filters. (d) Quality factor of different layers of HEPA filters and composite filters for $PN_{0.1}$ and $PN_{0.5}$ incense aerosol particles. (e) Relative change in pressure drop of PLLA/PDLA-5/5 NFA filter over a duration of 24 h under 60% and 90% RH conditions.

Table 4. 3 Average basis weight of the 1 layer commercial filter, PLLA/PDLA-5/5 Mat and PLLA/PDLA-5/5 NFA.

Sample	Average basis weight (g/m^2)
HEPA-1	102.62±0.84
PLLA/PDLA-5/5 Mat	1.65±0.26
PLLA/PDLA-5/5 NFA	1.75±0.02
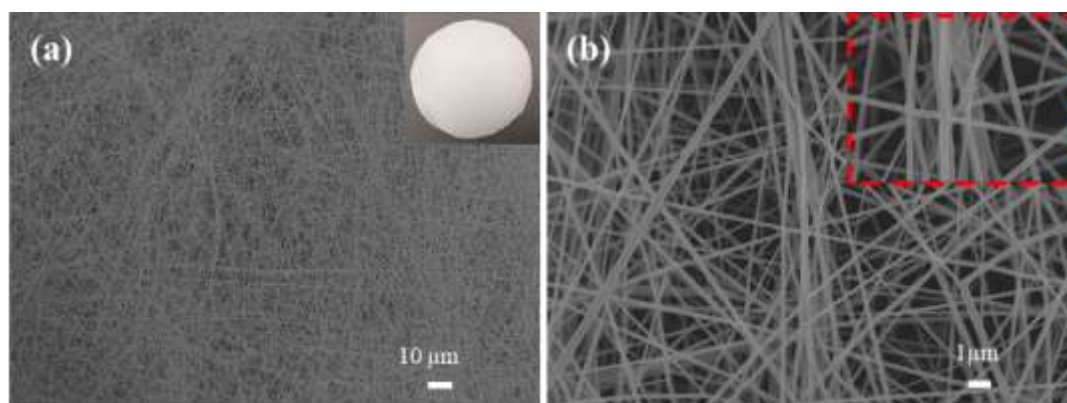
Figure 4. 8 (a, b) FESEM images of PLLA/PDLA-5/5 mat at different magnifications. Inset in (a) is the digital picture of the PLLA/PDLA-5/5 mat supported on wire mesh. Inset in (b) is the magnified image of agglutinated fibers of PLLA/PDLA-5/5 mat.

Table 4. 4 Filtration efficiencies and pressure drops of different layers of reference commercial filters, PLLA/PDLA-5/5 mat and NFA. The face velocity employed is 10 cm/s.

Filter	$PN_{0.1}$ filtration efficiency (%)	$PN_{0.5}$ filtration efficiency (%)	Pressure drop (Pa)
HEPA-1	98.01±0.53	98.42±0.30	48.17±4.25
HEPA-2	99.24±0.11	99.43±0.08	91.25±7.04
HEPA-3	99.65±0.21	99.75±0.11	139.00±6.73
HEPA-1-PLLA/PDLA-5/5 Mat	99.43±0.21	99.57±0.14	97.25±2.75
HEPA-1-PLLA/PDLA-5/5 NFA	99.83±0.00	99.83±0.01	74.67±4.54

Table 4. 5 Typical average PM and PN values before and after filtration of 1 layer commercial HEPA filter.

PM ($\mu g/m^3$) / PN (#/cm^3)	Before	After
PM 0.1	6.38 x 10	1.32
PM 0.5	3.93 x 10^2	3.34
PM 1.0	3.94 x 10^2	3.34
PN 0.1	2.47 x 10^5	9.42 x 10^3
PN 0.5	4.28 x 10^5	1.14 x 10^4
PN 1.0	4.28 x 10^5	1.14 x 10^4

Table 4. 6 Typical average PM and PN values before and after filtration of HEPA-1-PLLA/PDLA-5/5 NFA.

PM ($\mu g/m^3$) / PN (#/cm^3)	Before	After
PM 0.1	8.02×10	1.00×10^{-1}
PM 0.5	3.77×10^2	4.25×10^{-1}
PM 1.0	3.79×10^2	4.35×10^{-1}
PN 0.1	5.73×10^5	9.79×10^2
PN 0.5	7.69×10^5	1.32×10^3
PN 1.0	7.69×10^5	1.32×10^3

The quality factors (QF) of the filters discussed above are further analyzed for different particle sizes, as shown in Figure 4.7d. QF is defined as $-\ln (1-E)/\Delta P$), where E and ΔP denote the filtration efficiency and pressure drop across the filter, respectively. This parameter is used to assess the overall filtration performance of filters. With the synergistic combination of a high $PN_{0.1}$ removal efficiency and low pressure drop, the HEPA-1-PLLA/PDLA-5/5 NFA exhibits the highest $QF_{0.1}$ compared with the commercial filters (one, two and three layers, respectively) and HEPA-1-PLLA/PDLA-5/5 Mat. It clearly demonstrates the potential of the NFA as filter materials to overcome the tradeoff between filtration efficiency and pressure drop for ultrafine particles. It is also worth noting that the PLLA/PDLA-5/5 NFA layer in the composite filter has very low specific mass (1.75 g/m^2) as compared with that of the one-layer HEPA filter (HEPA-1, 106.62 g/m^2), as shown in Table S1. For 0.5 µm particles, the $QF_{0.5}$ of HEPA-1-PLLA/PDLA-5/5 NFA (85.4×10^{-3} Pa^{-1}) is marginally comparable to that of HEPA-1 (86.1×10^{-3} Pa^{-1}).

The PLLA/PDLA-5/5 NFA was further subjected to long-term stability test under two different humidity conditions - 60% and 90% RH (Figure 4.7e). The changes in the relative pressure drop is minimal under both humidity conditions, implying that the nanofibrous structure is very stable under damp conditions probably because the inter-fiber stereocomplex is hydrophobic in nature. This shows diverse potential of this nanofibrous macrostructure as filter materials. Additionally, HEPA-1-PLLA/PDLA-5/5 NFA could achieve consistently high filtration efficiency accompanied with a stable and low pressure drop despite being subjected to relatively long-term filtration tests under relatively high concentrations (~600-800 $\mu g \, m^{-3}$) of hazardous particles (incense aerosol). Over a duration of 24 h, the filtration efficiency is only changed from the initial value of 99.83% to 99.78% at the end.

To verify and understand the improved performance of HEPA-1-PLLA/PDLA-5/5 NFA composite filter, filtration tests were also carried out with 0.1 µm and 0.5 µm DEHS aerosol particles generated using an aerosol generator (TOPAS SLG 250), which simulate the organic haze particles generated by burning biomass [37-38]. The number distribution of these model particles are shown in Figure 4.9a. The curves show reasonably sharp peaks, indicating relatively narrow size distributions around the desired aerosol sizes. In Figure 4.9b, it is evident that the filtration efficiency of HEPA-1-PLLA/PDLA-5/5 NFA for 0.1 µm DEHS particles is much higher than that of HEPA-1, significantly higher than that of HEPA-2 but lower than that of HEPA-3. This trend is slightly different from that of the filtration efficiencies for incense particles. This may be due to the complex chemistry of the organic compounds generated by burning incense [37], which may be more easily adsorbed on a filter material comprising of organic material such as PLA-SC used in this work. A similar trend is also observed for the filtration efficiency for 0.5 µm DEHS particles. It is interesting to note that the filtration efficiency of the composite filter for 0.5 µm DEHS particles is significantly higher than that obtained from the tests carried out with burning incense, which is due to significantly more DEHS particles having diameters close to 0.5 µm, which increases the probability of being captured via

impaction and interception. Additionally, as seen in Chapter 3 and Figure 4.9a, the size distribution of incense particles tends to be broader than that of 0.1 µm DEHS particles, and from the distribution curves, it can be concluded that the aerosols generated by incense burning consists of a larger proportion of ultrafine particles. As a result, the higher removal efficiency of incense particles implies that the NFA has great potential in the capture of ultrafine particles.
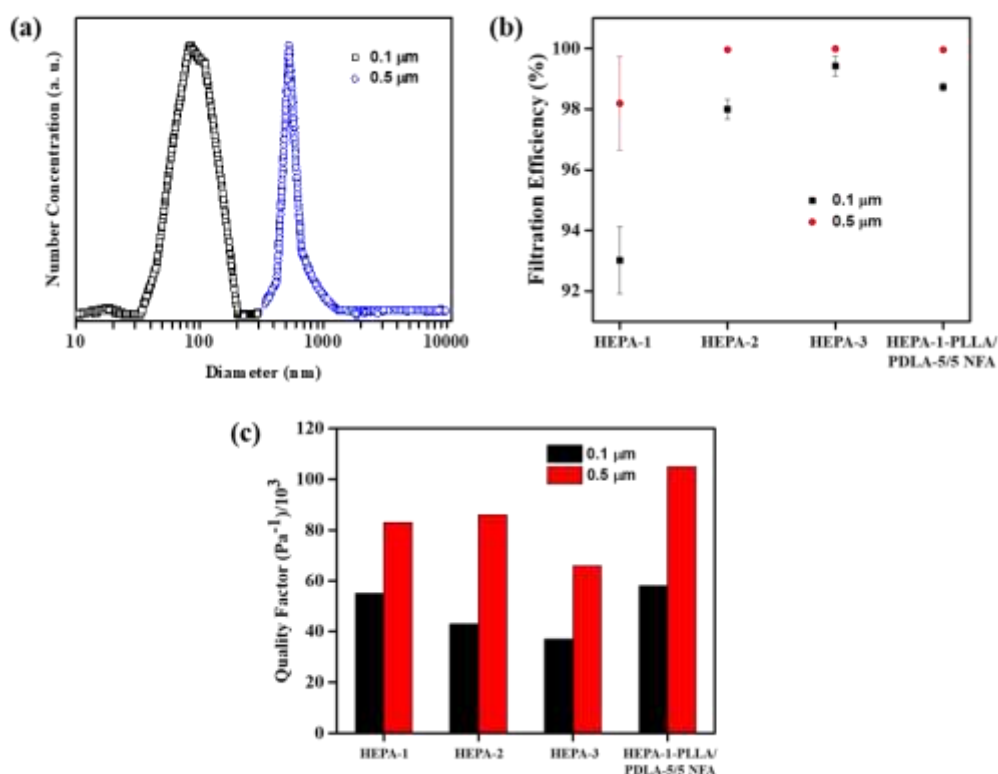
Figure 4. 9 (a) Typical size distribution curves of the DEHS aerosol particles based on number concentration. (b) Filtration efficiencies and (c) quality factors of the filters made of different layers of HEPA and HEPA-1-PLLA/PDLA-5/5 NFA.

To further evaluate the performance of the HEPA-1-PLLA/PDLA-5/5 NFA composite filter, the QF for 0.1 µm and 0.5 µm DEHS particles were calculated. The results are presented in Figure 4.9c. It is evident that the composite filter outperforms HEPA-1, HEPA-2 and HEPA-3 for both 0.1 µm (55.2×10^{-3} Pa^{-1}) and 0.5 µm (104.8

x 10^{-3} Pa^{-1}) particles. Therefore, the addition of the NFA layer to a HEPA filter indeed provides significant benefits to the filter performance.

4.4 Conclusion

In this chapter, we have verified that when PLLA/PDLA blend nanofibers come into contact, spontaneous inter-fiber stereocomplexation could take place, leading to the formation of inter-fiber junctions. The cross-linking induced by the spontaneous inter-fiber stereocomplexation could be easily controlled by adjusting the mass ratio of high-molecular-weight PLLA to low-molecular-weight PDLA in the blend. The cross-linked NFAs show significantly improved compression resistance. However, the aerogels were still quite delicate to touch and deformed permanently when compressed. Moreover, the limited working range of molecular weights further restricts the use of PLA with higher molecular weights that could give rise to stronger inter-fiber stereocomplexation due to stronger chain entanglements. Therefore, new strategies to improve the inter-fiber cross-linking should be considered in order to realize the potential of this approach to prepare robust NFAs. Nevertheless, this simple strategy may also be applicable to other stereoisomer systems for fabrication of highly porous yet stable NFAs.

Additionally, a composite filter with high filtration efficiency for ultrafine particles and relatively low pressure drop was fabricated by combining a HEPA filter with a thin layer of the cross-linked NFA. This shows the potential to improve the PN$_{0.1}$ filtration efficiency of conventional HEPA filters with only a slight increase in pressure drop. It is believed that nanofibers may play a part in enhancing the slip flow effect, whereas the pressure drop is further reduced due to the high porosity of the NFA. Meanwhile, at the same mass the highly porous NFA possesses a greater thickness than electrospun nanofibrous mats, giving ultrafine particles longer residence time in the NFA and hence the probability of these particles being adsorbed onto the fiber surface through Brownian motion is much larger. It shows that highly porous NFAs exhibit great potential to be used as an auxiliary layer on HEPA filters

for the high-efficiency removal of ultrafine particles in various applications. The cross-linked 3D NFAs may also find applications in many other fields, such as for biomedical applications.

References

1.   See, S. W.; Balasubramanian, R.; Wang, W., A study of the physical, chemical, and optical properties of ambient aerosol particles in Southeast Asia during hazy and nonhazy days. *Journal of Geophysical Research: Atmospheres* **2006,** *111* (D10), n/a-n/a.

2.   Ostro, B.; Hu, J.; Goldberg, D.; Reynolds, P.; Hertz, A.; Bernstein, L.; Kleeman, M. J., Associations of mortality with long-term exposures to fine and ultrafine particles, species and sources: results from the California Teachers Study Cohort. *Environmental health perspectives* **2015,** *123* (6), 549.

3.   Li, N.; Georas, S.; Alexis, N.; Fritz, P.; Xia, T.; Williams, M. A.; Horner, E.; Nel, A., A work group report on ultrafine particles (American Academy of Allergy, Asthma & Immunology): Why ambient ultrafine and engineered nanoparticles should receive special attention for possible adverse health outcomes in human subjects. *Journal of Allergy and Clinical Immunology* **2016,** *138* (2), 386-396.

4.   Brincat, J.-P.; Sardella, D.; Muscat, A.; Decelis, S.; Grima, J. N.; Valdramidis, V.; Gatt, R., A review of the state-of-the-art in air filtration technologies as may be applied to cold storage warehouses. *Trends in Food Science & Technology* **2016,** *50*, 175-185.

5.   Hassan, M. A.; Yeom, B. Y.; Wilkie, A.; Pourdeyhimi, B.; Khan, S. A., Fabrication of nanofiber meltblown membranes and their filtration properties. *Journal of Membrane Science* **2013,** *427*, 336-344.

6.   Liu, G.; Xiao, M.; Zhang, X.; Gal, C.; Chen, X.; Liu, L.; Pan, S.; Wu, J.; Tang, L.; Clements-Croome, D., A review of air filtration technologies for sustainable and healthy building ventilation. *Sustainable Cities and Society* **2017,** *32* (Supplement C), 375-396.

7.   Chuanfang, Y., Aerosol filtration application using fibrous media—an industrial perspective. *Chinese journal of chemical Engineering* **2012,** *20* (1), 1-9.

8.   Zhu, M.; Han, J.; Wang, F.; Shao, W.; Xiong, R.; Zhang, Q.; Pan, H.; Yang, Y.; Samal, S. K.; Zhang, F., Electrospun nanofibers membranes for effective air filtration. *Macromolecular Materials and Engineering* **2017,** *302* (1), 1600353.

9.   Sparks, T.; Chase, G., Section 7 - Filter Selection, Process Design, Testing, Optimization and Troubleshooting Guidelines. In *Filters and Filtration Handbook (Sixth Edition)*, Sparks, T.; Chase, G., Eds. Butterworth-Heinemann: Oxford, 2016; pp 383-413.

10.   Leung, W. W.-F.; Hung, C.-H.; Yuen, P.-T., Effect of face velocity, nanofiber packing density and thickness on filtration performance of filters with nanofibers coated on a substrate. *Separation and purification technology* **2010,** *71* (1), 30-37.

11.   Kuo, Y.-Y.; Bruno, F. C.; Wang, J., Filtration performance against nanoparticles by electrospun nylon-6 media containing ultrathin nanofibers. *Aerosol science and technology* **2014,** *48* (12), 1332-1344.

12.   Wang, Z.; Pan, Z., Preparation of hierarchical structured nano-sized/porous poly (lactic acid) composite fibrous membranes for air filtration. *Applied Surface Science* **2015,** *356*, 1168-1179.

13.   Zhang, S.; Liu, H.; Yu, J.; Luo, W.; Ding, B., Microwave structured polyamide-6 nanofiber/net membrane with embedded poly (m-phenylene isophthalamide) staple fibers for effective ultrafine particle filtration. *Journal of Materials Chemistry A* **2016,** *4* (16), 6149-6157.

14.   Sambaer, W.; Zatloukal, M.; Kimmer, D., 3D modeling of filtration process via polyurethane nanofiber based nonwoven filters prepared by electrospinning process. *Chemical Engineering Science* **2011,** *66* (4), 613-623.

15.   Sambaer, W.; Zatloukal, M.; Kimmer, D., 3D air filtration modeling for nanofiber based filters in the ultrafine particle size range. *Chemical Engineering Science* **2012,** *82* (Supplement C), 299-311.

16.   Hosseini, S.; Tafreshi, H. V., Modeling permeability of 3-D nanofiber media in slip flow regime. *Chemical Engineering Science* **2010,** *65* (6), 2249-2254.

17.   Pham, Q. P.; Sharma, U.; Mikos, A. G., Electrospun poly (ε-caprolactone) microfiber and multilayer nanofiber/microfiber scaffolds: characterization of scaffolds and measurement of cellular infiltration. *Biomacromolecules* **2006,** *7* (10), 2796-2805.

18.   Wang, W.; Itoh, S.; Matsuda, A.; Ichinose, S.; Shinomiya, K.; Hata, Y.; Tanaka, J., Influences of mechanical properties and permeability on chitosan nano/microfiber mesh tubes as a scaffold for nerve regeneration. *Journal of Biomedical Materials Research Part A* **2008,** *84A* (2), 557-566.

19.   Wang, W.; Itoh, S.; Konno, K.; Kikkawa, T.; Ichinose, S.; Sakai, K.; Ohkuma, T.; Watabe, K., Effects of Schwann cell alignment along the oriented electrospun chitosan nanofibers on nerve regeneration. *Journal of Biomedical Materials Research Part A* **2009,** *91* (4), 994-1005.

20.   Yao, Q.; Cosme, J. G.; Xu, T.; Miszuk, J. M.; Picciani, P. H.; Fong, H.; Sun, H., Three dimensional electrospun PCL/PLA blend nanofibrous scaffolds with significantly improved stem cells osteogenic differentiation and cranial bone formation. *Biomaterials* **2017,** *115*, 115-127.

21.   Sun, B.; Long, Y.-Z.; Yu, F.; Li, M.-M.; Zhang, H.-D.; Li, W.-J.; Xu, T.-X., Self-assembly of a three-dimensional fibrous polymer sponge by electrospinning. *Nanoscale* **2012,** *4* (6), 2134-2137.

22.   Bonino, C. A.; Efimenko, K.; Jeong, S. I.; Krebs, M. D.; Alsberg, E.; Khan, S. A., Three-dimensional electrospun alginate nanofiber mats via tailored charge repulsions. *Small* **2012,** *8* (12), 1928-1936.

23.   Fundador, N. G. V.; Takemura, A.; Iwata, T., Structural Properties and Enzymatic Degradation Behavior of PLLA and Stereocomplexed PLA Nanofibers. *Macromolecular Materials and Engineering* **2010,** *295* (9), 865-871.

24.   Buescher, J. M.; Margaritis, A., Microbial biosynthesis of polyglutamic acid biopolymer and applications in the biopharmaceutical, biomedical and food industries. *Critical reviews in biotechnology* **2007,** *27* (1), 1-19.

25.   Monticelli, O.; Putti, M.; Gardella, L.; Cavallo, D.; Basso, A.; Prato, M.; Nitti, S., New Stereocomplex PLA-Based Fibers: Effect of POSS on Polymer Functionalization and Properties. *Macromolecules* **2014,** *47* (14), 4718-4727.

26.   Li, Z.; Muiruri, J. K.; Thitsartarn, W.; Zhang, X.; Tan, B. H.; He, C., Biodegradable silica rubber core-shell nanoparticles and their stereocomplex for efficient PLA toughening. *Composites Science and Technology* **2018,** *159*, 11-17.

27.   Muiruri, J. K.; Liu, S.; Teo, W. S.; Kong, J.; He, C., Highly biodegradable and tough polylactic acid–cellulose nanocrystal composite. *ACS Sustainable Chemistry & Engineering* **2017,** *5* (5), 3929-3937.

28.   Tsuji, H.; Mohan, R., Research advances in macromolecules. *Thiruvanathapuram, India* **2000,** *1*, 25.

29.   Pan, G.; Xu, H.; Mu, B.; Ma, B.; Yang, Y., A clean approach for potential continuous mass production of high-molecular-weight polylactide fibers with fully stereo-complexed crystallites. *Journal of Cleaner Production* **2018,** *176*, 151-158.

30.   Pan, G.; Xu, H.; Mu, B.; Ma, B.; Yang, J.; Yang, Y., Complete stereo-complexation of enantiomeric polylactides for scalable continuous production. *Chemical Engineering Journal* **2017,** *328*, 759-767.

31.   Saini, P.; Arora, M.; Kumar, M. R., Poly (lactic acid) blends in biomedical applications. *Advanced drug delivery reviews* **2016,** *107*, 47-59.

32.   Kurokawa, N.; Hotta, A., Thermomechanical properties of highly transparent self-reinforced polylactide composites with electrospun stereocomplex polylactide nanofibers. *Polymer* **2018**.

33.   Jing, Y.; Zhang, L.; Huang, R.; Bai, D.; Bai, H.; Zhang, Q.; Fu, Q., Ultrahigh-performance electrospun polylactide membranes with excellent oil/water separation ability via interfacial stereocomplex crystallization. *Journal of Materials Chemistry A* **2017,** *5* (37), 19729-19737.

34.   Zhu, J.; Na, B.; Lv, R.; Li, C., Enhanced stereocomplex formation of high-molecular-weight polylactides by gelation in an ionic liquid. *Polymer international* **2014,** *63* (6), 1101-1104.

35.   Tsuji, H.; Hyon, S. H.; Ikada, Y., Stereocomplex formation between enantiomeric poly(lactic acid)s. 4. Differential scanning calorimetric studies on precipitates from mixed solutions of poly(D-lactic acid) and poly(L-lactic acid). *Macromolecules* **1991,** *24* (20), 5657-5662.

36.   Tsuji, H., Poly(lactide) stereocomplexes: formation, structure, properties, degradation, and applications. *Macromol Biosci* **2005,** *5* (7), 569-97.

37.   Lin, T.-C.; Krishnaswamy, G.; Chi, D. S., Incense smoke: clinical, structural and molecular effects on airway disease. *Clinical and Molecular Allergy* **2008,** *6* (1), 3.

38.   See, S. W.; Balasubramanian, R.; Rianawati, E.; Karthikeyan, S.; Streets, D. G., Characterization and source apportionment of particulate matter≤ 2.5 μm in Sumatra, Indonesia, during a recent peat fire episode. *Environmental science & technology* **2007,** *41* (10), 3488-3494.

Chapter 5

Robust Lignin-Based Aerogel Filters: High-Efficiency Capture of Ultrafine Airborne Particulates and the Mechanism

In this chapter, a new type of lignin-based honeycomb-like aerogel filters and their air filtration-related properties are reported. The aerogel filters are composed of aligned micrometer-sized pores and cross-linked lignin-based cell walls, prepared via a facile unidirectional ice-crystal-induced self-assembly from an aqueous solution followed by annealing at 300^oC. It is verified that with the cross-linking of lignin and reinforcement with a very small amount of graphene, the mechanical stiffness, thermal stability and humidity/water resistance of the aerogels could be significantly enhanced. The filtration results suggest that the abundant functional groups retained from lignin and the aligned pore channels could lead to high filtration efficiency for ultrafine particles accompanied with fairly low pressure drop. Moreover, these low-cost and renewable biomass-based filters also exhibit outstanding long-term filtration efficiency. Filtration tests with various particles sizes also revealed that the filtration mechanism of such aerogel filters is dominated by diffusion rather than impaction or interception mechanism. It is believed that the findings from this work would offer a new avenue for the design of novel high-performance air filters.

5.1 Introduction

The work presented in Chapter 4 has revealed the usefulness of reinforcing the 3D structure of NFAs via spontaneous inter-fiber stereocomplexation, which could greatly enhance the compressive resistance of the aerogel filter. The concept of 3D air filtration was also demonstrated to be effective in addressing the trade-off between filtration efficiency and ΔP. However, the overall mechanical integrity of the NFA is still relatively weak, which hampers their practical use. Furthermore, the gelation problem of the PLLA/PDLA blend restricts the range of polymer molecular weights that can be used. Such high sensitivity to molecular weight changes makes it slightly challenging to prepare and control the extent of cross-linking in the NFA. Additionally, despite PLA being a renewable resource, the production costs is also known to be relatively more expensive than that of conventional petrochemical-derived polymers. Filtration wise, though the NFA composite filter exhibit lower ΔP (74.67 Pa) than that of the NFM composite filter (97.25 Pa), the overall ΔP is still relatively high. Thus, the aforementioned issues should be addressed for the facile development of highly-efficient 3D filters that are more economically viable.

For instance, the limitations of stereocomplex-induced cross-linking could be overcome by employing a more facile and straightforward cross-linking method. It is widely known that cross-links are realized through the formation of covalent bonds or weak intermolecular interactions, which can be generally initiated via heat, pressure, pH changes, UV-irradiation, addition of chemicals or self-assembly[1-6]. Notably, compared with other cross-linking methods, thermal cross-linking has emerged as a more facile and cheaper method to reinforce the structures of aerogels by simply inducing chemical reactions at elevated temperatures [1, 7-8]. However, by adopting this method, many researchers have also reported annealing-induced shrinkage of the porous materials, especially at relatively high heat treatment temperatures (> 500°C), which could induce pore size reduction or even pore structural change of the porous materials [5, 9-10]. Thus, to adopt this cross-linking

method for the fabrication of aerogel filters, there is a need to introduce some reinforcing agent to minimize or even eliminate this shrinking phenomenon.

To keep production costs low, cheaper alternatives such as low-cost biomass-based products could be considered as the aerogel starting material. In Chapter 3, lignin, which is one of the most abundant biomass product, is introduced. Due to its low-cost and wide availability, lignin exhibits great potential to be employed as building blocks of aerogels. Additionally, the various organic functional groups of lignin may also promote the adsorption of PM, which could enhance the filtration efficiency of the 3D aerogel filter.

On the other hand, in order to keep ΔP low, the macro/microstructures of the aerogel could be designed such that the pores would not disrupt the airflow significantly, while at the same time, maintain a high filtration efficiency for ultrafine particles. As introduced in Chapter 2, a new type of non-fibrous honeycomb-like aerogel with aligned micrometer-sized channels has been reported [11]. Unlike the NFA filter that depends on the interconnected fibrous network to create tortuous channels for capturing PM, the honeycomb-like aerogel offers a large volume of aligned channels for the diffusion capture of ultrafine particles, while the hollow nature of the channels would ease the airflow and lead to significantly lower ΔP. This novel design of 3D filters could essentially alleviate the trade-off between filtration efficiency and ΔP. Simulation studies also suggest that the filtration mechanism of such aligned tubular structures would function on the principle of size-dependent trajectory segregation [12]. Nonetheless, so far only one work has been reported and there is still a lack of a systematic study to fully understand the underlying filtration mechanism. Furthermore, the materials employed are expensive and stems from non-renewable resources.

In this Chapter, building on from the suggestions raised above, we design a new type of lignin-based honeycomb-like aerogel filters with aligned micrometer-sized pores, prepared via a facile unidirectional ice-templating method. The results obtained

revealed that low-temperature annealing together with the addition of a small amount of graphene in the form of graphene oxide (GO) could help reinforce the 3D structure of the aerogel, minimizing the thermally-induced shrinkage. Our results suggest that the reduced volume shrinkage could be attributed to the sheet-like nature of GO that may facilitate the anchoring of GO onto cell walls of the honeycomb-like structure. Herein, we demonstrate that such honeycomb-like aerogels also exhibit excellent filtration efficiency for ultrafine particles at a low ΔP, as well as good long-term filtration performance, which outperform commercial fibrous filters including high-efficiency particulate arrestance (HEPA) filters. The unique filtration behavior for our honeycomb-like aerogels is also revealed based on the results of filtration tests using model particles of various sizes, which provides useful guidelines for further studies.

5.2 Experimental

5.2.1 Materials

Alkali lignin was purchased from Tokyo Chemical Industry Co. (USA, L0082, soft lignin). Graphene oxide was synthesized using the modified Hummer's method [13-14].

5.2.2 Preparation of Cross-linked Lignin-Based Aerogels

Lignin aqueous solutions of various concentrations were prepared by dissolving the alkali lignin in deionized water via magnetic stirring. The solutions were cast in a Teflon container with a metal base immersed in a cold source, such as liquid nitrogen or refrigerator (-20 °C), for unidirectional freezing. Unless specifically mentioned, the cold source is the liquid nitrogen with a temperature of -196 °C. In the freezing process, the temperature gradient between the top and bottom side of the solutions in the mold led to the formation of ice crystals at the bottom side and unidirectional growth of the crystals towards the top. Subsequently, the frozen samples were freeze-

dried in a freeze-drying vessel (-80 °C and 10 Pa) for around 24 h, and honeycomb-like lignin aerogels with aligned micron-sized pore channels and cell walls were obtained. The aerogels were then heated at a rate of 5 ℃/min in a tube furnace and annealed at the temperature of 300 ℃ for 2 h under argon atmosphere, leading to the cross-link of the aerogels. The lignin-based aerogels doped with graphene were prepared using the same procedure. In order to incorporate graphene layers into the aerogel cell walls, a GO aqueous suspension (prepared by modified Hummer's method as shown in our previous work [14], and the average lateral size of GO is around 10 μm) was mixed with lignin solutions for further freezing-drying process. The GO content in the lignin/GO mixture was fixed at 2.7 wt%. A wide range of densities of the aerogels was achieved by simply adjusting the water fraction of the initial aqueous suspensions. Also, various shapes or sizes of the honeycomb-like aerogels could be achieved by using various molds, satisfying a variety of application occasions. Unless mentioned, all the cross-linked samples were annealed at a temperature of 300 ℃ and the tested data were originated from these aerogels. The lignin-based aerogels were also annealed at 600 and 900 ℃ for 2 h, respectively, to make a comparison with the aerogel filters annealed at 300 ℃.

5.2.3 Characterization

Microstructural images of the honeycomb-like aerogels were obtained using a scanning electron microscope (SEM, JSM-7600F). The mechanical compressive curves were evaluated by a dynamic mechanical analyzer (DMA, TA Instruments Q800), and at least five samples were tested for each component. A thermogravimetric analyzer (TGA, TA Instrument Q500) was applied to realize the TGA curves. The experiment was carried out in nitrogen atmosphere. X-ray diffraction (XRD) patterns were attained by a specular reflection mode (Cu Kα radiation, PANalytical) at room temperature. The functional groups of the aerogels after drying treatment were characterized by FTIR (Spectrum One, PerkinElmer) spectroscopy. The porosities of the aerogels were estimated from the measured density of the aerogels and the corresponding bulk materials.

5.2.4 Filtration Test

In the testing process, the model haze particles were generated by burning incense. The PM particle concentration was controlled by diluting the incense smoke with air in a mixing chamber, down to a hazardous pollution level equivalent ($> 300 \, \mu g/m^3$). The particle concentration was measured simultaneously with a condensation particle counter (NanoScan SMPS 3910, TSI Instruments Ld) that could detect PM particles with sizes between 0.01 to 0.42 µm and an optical particle sizer (OPS 3330, TSI Instruments Ld) that could detect PM particle with sizes between 0.3 to 10 µm. The particle amount in airflow before and after the air inlet being covered by the filters was recorded by the particle counters, and the filtration efficiency was calculated through comparing the PM particle number before and after filters. The pressure drop was measured using a differential pressure gauge (Digital Manometer, Bluewind Laboratory Pte Ltd). The airflow to the filter was created by the use of an air pump, and the wind velocity was measured by the air velocity meter (Airflow instruments velocity meter TA430, TSI Instruments Ld). The wind velocity and humidity in the mixing chamber could both be adjusted, and unless specially mentioned, the face velocity and humidity used in the filtration testing was 5.3 cm/s and 60 %, respectively. To further study the filtration mechanism of the aerogels, aerosols of DEHS were generated with a Condensation Aerosol Generator (SLG 250, TOPAS GmbH). DEHS is a colourless liquid that is insoluble in water and commonly used for aerosol generation for filter testing. DEHS particles with size of 0.1, 0.2, 0.3, 0.5 and 1.0 µm were produced respectively by the generator.

5.3 Results and Discussion

The preparation process for the honeycomb-like aerogels is illustrated in Figure 5.1a-c. Briefly, unidirectional ice-crystal-induced self-assembly of lignin in an aqueous suspension leads to aligned cell walls, and a small amount of GO can be conveniently incorporated in the cell walls of the lignin-based aerogels (Figure 5.1a and b). By low-temperature (300 °C) annealing, cross-linked cell walls, which are composed of

annealed lignin (A-lignin) doped with a small fraction of GO-derived reduced graphene layers as reinforcement, can be obtained (Figure 5.1c). This results in excellent microstructural and macroscopic stabilities as well as outstanding mechanical strength of the A-lignin/graphene (A-lignin/G) composite aerogels, which can support a piece of metal of over two thousand times heavier without suffering significant plastic deformation (Figure 5.1d and e, Figure 5.2). Moreover, the lignin-based aerogels can be cross-linked at a low annealing temperature compared with the commonly used annealing temperature ($\geq$ 900 ℃) in traditional carbonization processes [14-17], which is instrumental in further lowering the cost. The assembly process leads to honeycomb-like texture formed by micrometer-sized isotropic pores in the cross sectional plane (Figure 5.1f) and aligned pore channels in the longitudinal direction (Figure 5.1g and h). The cross-linking process of the aerogels has minimal effects on the aligned pore channels, but leads to rougher surface and smaller thickness of cell walls (Figure 5.1g-j). Compressive stress-strain curves of the aerogels show the significant roles of initial concentration, cross-linking and the presence of graphene layers play in enhancing the mechanical strength of the aerogels (Figure 5.1k). Obviously, higher lignin concentrations contribute more building blocks to the resultant aerogels and hence give higher modulus. The low-temperature annealing-induced cross-linking and incorporation of a low fraction of graphene layers can also lead to significant mechanical enhancement of the aerogels, respectively. Furthermore, the thermal stability of the aerogels is also significantly enhanced via annealing, and it increases with the annealing temperature, as shown in Figure 5.1l.

Figure 5. 1 Schemes showing the fabrication process of the honeycomb-like aerogels: (a) unidirectional ice-crystal-induced self-assembly of the lignin/GO suspension, (b) lignin-based aerogels prepared by freeze-drying, (c) cross-linked lignin/graphene (A-lignin/G) aerogels obtained by low-temperature annealing. Photographs of (d) lignin/GO aerogel and (e) A-lignin/G aerogel (the inset show that lignin/GO aerogel is crushed and A-lignin/G aerogels is stable when they are supporting a metal over 2000 times heavier). (f) A SEM image showing porous microstructures of A-lignin/G aerogels with honeycomb-like texture in cross sectional plane. Porous microstructures in longitudinal plane of (g) lignin/GO and (h) A-lignin/G aerogels. Cell walls of (i) lignin/GO and (j) A-lignin/G aerogels. (k) Compressive curves of the aerogels prepared from suspensions of various lignin

concentrations. (l) Thermogravimetric analysis traces of the aerogels after annealing at different temperatures.
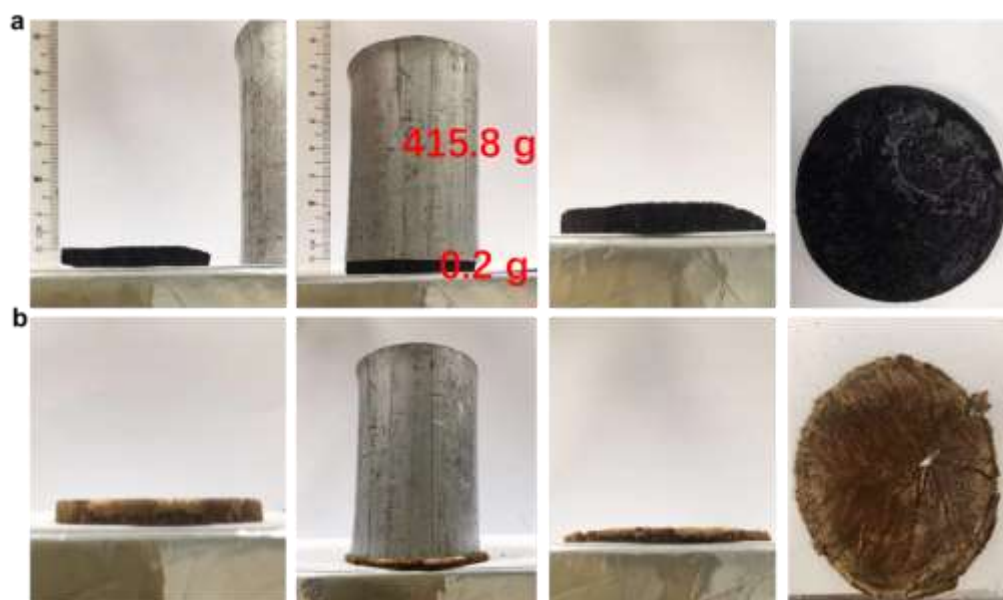
Figure 5. 2 The (a) A-lignin/G and (b) lignin/GO aerogels supporting a metal that is more than 2000 times heavier than the aerogels. The images show that the thickness of the A-lignin/G aerogel is not changed after supporting the metal but the lignin/GO aerogel is crushed, demonstrating the excellent mechanical strength of the cross-linked lightweight aerogels.

The thermogravimetric analysis (TGA)/differential thermal gravity (DTG) curves, X-ray diffraction (XRD) patterns, and Fourier transform infrared (FTIR) spectra of the honeycomb-like aerogels provide further evidence for the occurrence of cross-linking and its influence. Lignin consists of macromolecules with three-dimensional links among their methoxylated aromatic units. The TGA/DTG curves of lignin-based aerogels show three typical regions (Figure 5.1l) [14, 17]. The first weight loss stage in the temperature range from 40 to 100 °C corresponds to the evaporation of the water absorbed, which also implies the presence of plentiful hydrophilic functional groups in the aerogels. The weight loss at around 300 °C can be mainly attributed to the cleaving of alkyl and methoxy groups in the pyrolysis process, releasing methanol and phenolic compounds with hydroxyl group and alkyl groups.

At the temperatures above 600 °C, the decarbonylation reaction of alkyl side chains and significant reduction of functional groups could occur, facilitating the formation of amorphous carbon. Therefore, XRD patterns of the A-lignin-based aerogels annealed at 300 and 600 °C show a sharp peak at $2\theta = 22.5°$, which is similar to that of the lignin-based aerogels, while those annealed at 900 °C show a broad peak at $2\theta = \sim24.5°$ that corresponds to amorphous carbon (Figure 5.3a). FTIR studies (Figure 5.3b, Figure 5.4) further confirm the structural change of the lignin/GO composites caused by annealing. After annealing at 300 °C, the intensity of the C-H stretching band at around 2937 cm^{-1}, which corresponds to aromatic methoxyl groups as well as the methyl and methylene groups of side chains, is decreased significantly. This can be attributed to the reduction reactions of these groups. The bands at 1043-1073 cm^{-1}, which can be ascribed to C-O stretching, are also weakened, indicating the breakage of some C-O bonds. By contrast, the annealing at 600 °C results in the loss of many functional groups, causing a large intensity reduction of many bands. The band at 1639 cm^{-1} (C=C) indicates that there is still a significant amount of the aromatic rings retained in the structure. However, the band at around 1736 cm^{-1}, which is ascribed to C=O bonds, are not observed, implying that most of the C=O are cleaved. The FTIR spectrum of the aerogels after annealing at 900 °C shows a relatively flat curve with no obvious band, indicating that most of the functional groups have been converted to amorphous carbon. In short, the functional groups that can interact with PM particles are reduced with increased annealing temperature, and almost removed for the A-lignin-based aerogels annealed at 900 °C. In addition, higher annealing temperatures also lead to much lower product yields, and larger volume shrinkage of the aerogels because of the massive weight reduction of the lignin in the annealing process. The shrinkage can lead to the reduction of the filtration efficiency for ultrafine PM particles yet increase the ΔP (Figure 5.4c). Without annealing, the lignin-based aerogels show a higher ΔP and relatively lower filtration efficiency than the A-lignin-based aerogels annealed at 300 °C because the former have a lower porosity (Table 5.1) and smoother cell walls that are not beneficial for adsorption of PM particles. Furthermore, the uncross-linked lignin-based aerogels are too fragile to be used for filtration, which often results in sample

breaking down in the testing process. More importantly, the A-lignin-based aerogels can well retain its integrity after being immersed in water for more than 20 hours, while the lignin-based aerogels are dissolved immediately upon contacting with water (Figure 5.3, Figure 5.5). Therefore, the A-lignin-based aerogels are able to exhibit a stable ΔP in an extremely high-humidity environment of 95 % RH for over 20 hours. The excellent water/humidity resistance of the A-lignin-based aerogels render the aerogels suitable for high-humidity filtration environments.
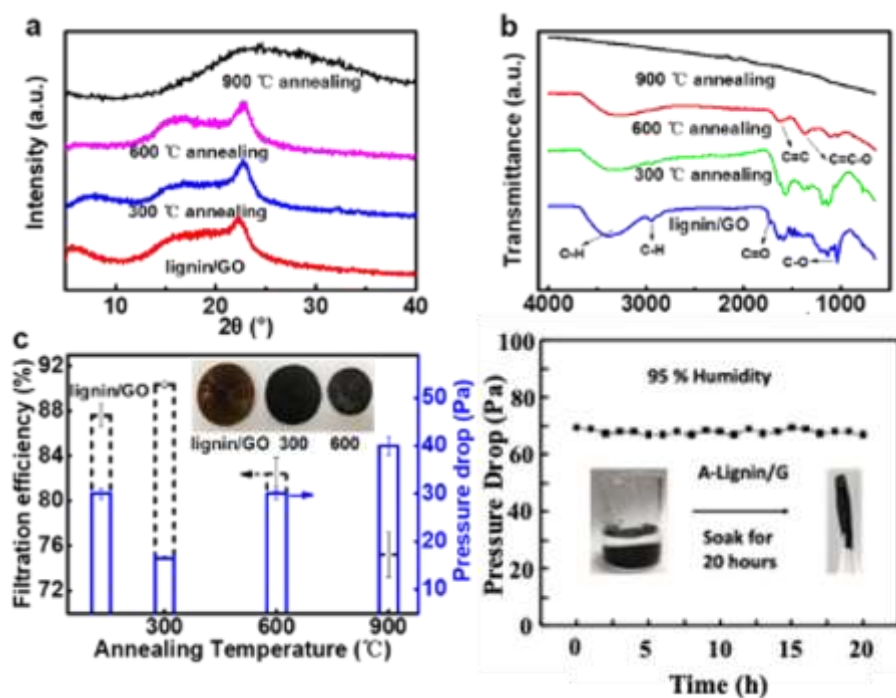
Figure 5. 3 (a) XRD patterns and (b) FTIR spectra of the aerogels before and after cross-linking at various temperatures; (c) filtration efficiency and pressure drop of the 3.6 mm-thick 5.0 w% A-lignin/G aerogels after annealing at various temperatures (the inset shows optical images of the samples annealed at various temperatures); (d) relative pressure drop (ΔP at a certain time/initial ΔP) for the A-lignin/G aerogels annealed at 300 ℃ under humidity of 95 % RH as a function of time (the inset shows the pictures of the aerogels soaked in water and after soaking for 20 hrs, demonstrating the water-resistance of the cross-linked lignin).
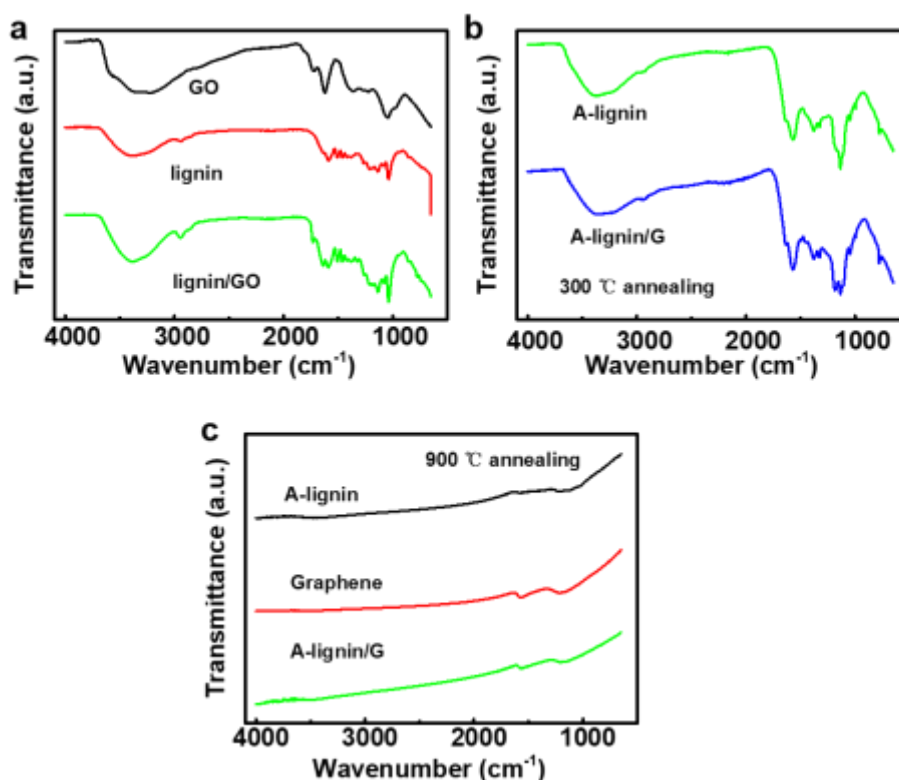
Figure 5. 4 FTIR of the aerogels (a) the GO, lignin and lignin/GO aerogels, (b) the A-lignin and A-lignin/G aerogels annealed at 300 °C, and (c) the A-lignin, Graphene, and A-lignin/G aerogels annealed at 900 °C.

Table 5. 1 Properties of the 5 wt% lignin-based aerogels. (Pore size is obtained from the SEM images and refers to the gap between adjacent cell walls)

Materials type of the aerogel	Lignin	Lignin/GO	A-lignin (300)	A-lignin/G (300)	A-lignin (900)
Density (mg/cm^3)	65.22	65.44	59.26	50.09	78.9
Porosity (%)	94.56	94.55	97.31	97.77	96.41
Pore size (µm)	20~40	20~40	16~35	20~36	11~20
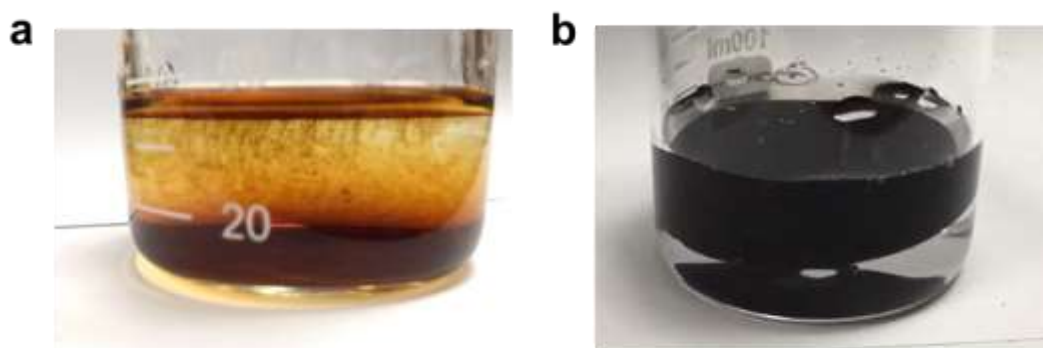
Figure 5. 5 Photos of the aerogels soaked in the water: (a) lignin-based aerogel that is dissolved in the water immediately and (b) A-lignin-based aerogel that keep stable for a long period of time.

The morphology of the aerogel also plays an important role on the filtration performance of honeycomb-like aerogels. Using the ice-templated freeze-drying method, the porosity, pore size, and cell wall thickness of the lignin-based aerogels can be easily adjusted by changing the processing parameters such as lignin concentration, graphene reinforcement and freezing temperature. Higher lignin concentration in the suspension can increase the amount of building blocks in the aerogels, contributing to higher density and lower porosity. Interestingly, the presence of a small amount of graphene leads to a lower density (higher porosity) for the A-lignin-based aerogels, which can be attributed to the mechanical enhancement of cell walls that result in a smaller volume shrinkage of the macroscopic aerogels (Figure 5.6a). Higher initial lignin concentration, which causes lower porosity of the aerogels, leads to higher filtration efficiency due to the presence of more functional groups in the A-lignin-based aerogels. Differently, the presence of graphene affects the filtration efficiency slightly but significantly reduces the ΔP (Figure 5.6b). For example, the ΔP values are 16.5 Pa and 32.9 Pa, respectively, for the A-lignin/G and A-lignin aerogels prepared from 5 wt% lignin-based suspension, while both show similar filtration efficiencies values of above 90 %. In addition to the smaller macroscopic shrinkage, the A-lignin/G aerogels with mechanically enhanced cell walls also show more aligned and regular pore channels than those of

the A-lignin aerogels (Figure 5.6c-d, Figure 5.7), which is beneficial for the flow of air molecules and the reduction of ΔP. Therefore, the ΔP can be lowered down to 5.5 Pa by adjusting the initial lignin concentration of the A-lignin-based aerogels, which is accompanied by a relatively high filtration efficiency of over 70 % for ultrafine particles. Moreover, it should also be mentioned that it may be possible to replace the GO with other types of reinforcements, such as exfoliated clay or recycled cellulose fibers, to improve the mechanical properties of the cell walls in the lignin aerogels, further lowering the cost of the air filters as well as making them more sustainable and biodegradable.

The filtration efficiency can also be increased significantly by increasing the thickness of the filters, which gives a slight increase of the ΔP due to the aligned pore channels (Figure 5.6e). The filtration efficiency reaches 96.5 %, an efficiency level comparable to that of the reference HEPA filter (over 95 %), while the ΔP is only 24 Pa for the honeycomb-like aerogels at a thickness of 4.2 mm. When the thickness of the A-lignin/G aerogels prepared from 5.0 wt% lignin suspension is increased to 8 mm, the efficiency reaches a value of 99.85 % at a low ΔP of 45 Pa. By controlling the lignin concentration or thickness of the aerogels, the efficiency and ΔP can be fine-tuned to satisfy various filtration applications. For example, the efficiency of the A-lignin/G aerogels prepared from 3.6 wt% lignin suspension can be adjusted to 99.97 % at a thickness of 12 mm and ΔP of 74 Pa.
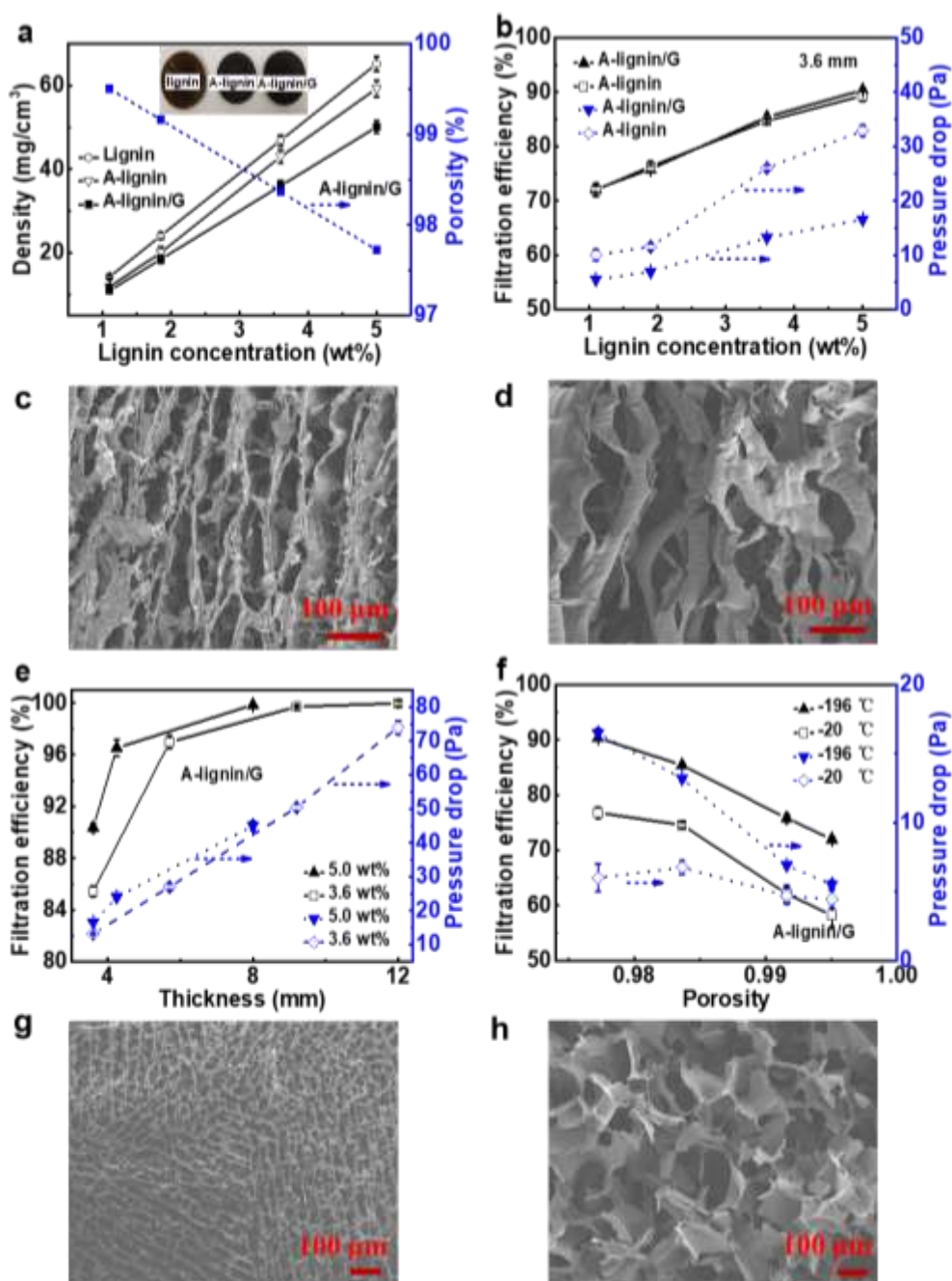
Figure 5. 6 (a) Density and porosity of the lignin-based aerogels prepared from suspensions of various lignin concentrations before and after cross-linking (the inset shows the optical images of the aerogels (from left to right: lignin, A-lignin, and A-lignin/G aerogels). (b) Filtration efficiency and pressure drop of the 3.6 mm-thick A-lignin and A-lignin/G aerogels prepared from suspensions of various lignin concentrations. SEM images showing microstructures of (c) A-lignin/G and (d) A-lignin aerogels. Filtration efficiency and pressure drop of (e) A-lignin/G (prepared

from 5 wt% lignin suspension) with various thicknesses, and (f) 3.6 mm-thick A-lignin/G aerogels prepared at different freezing temperatures. Microstructures of A-lignin/G prepared from 5.0 wt% lignin suspension frozen at (g) -20 ℃ and (h) -196 ℃. (A-lignin and A-lignin/G aerogels are annealed at 300 ℃).
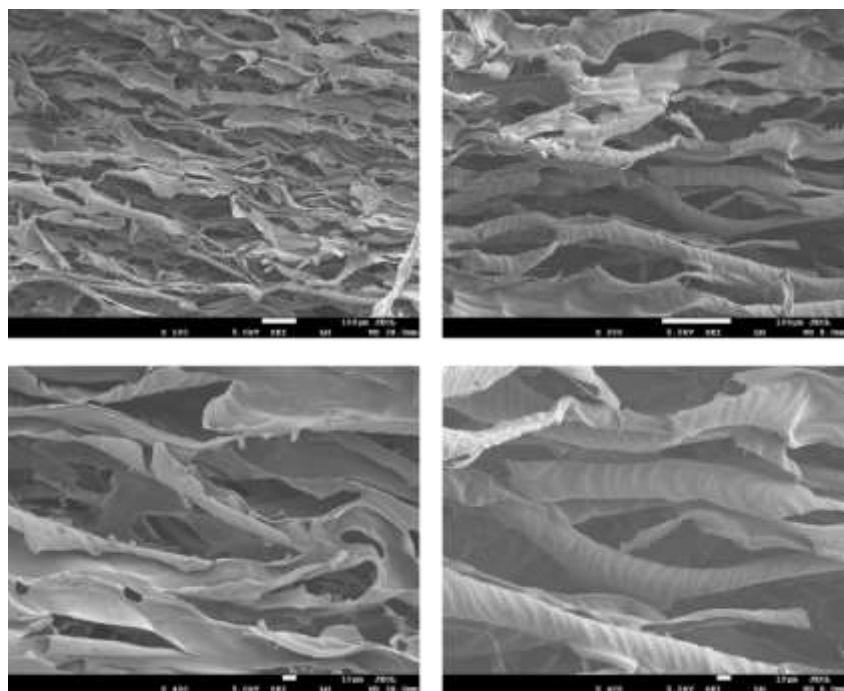
Figure 5. 7 SEM images of A-lignin aerogels derived from 3.65 wt% lignin and 300℃ annealing treatment.

The freezing temperature can also be controlled to adjust the microstructure of the aerogels, which gives rise to different filtration performance (Figure 5.6f). Higher freezing temperature such as -20 ℃ leads to less ice-crystal nuclei at the bottom of the suspension and hence thicker ice crystals [18-19]. The average pore size is obviously larger and the cell walls are thicker (Figure 5.6g and h, Figure 5.8). Therefore, the aerogels frozen at a higher temperature exhibit lower ΔP and filtration efficiency owing to the reduced overall amount of functional groups on the surface of thicker cell walls. It is also observed that aerogels prepared at a lower lignin concentration and different freezing temperatures show smaller difference in their ΔP values, which can be ascribed to their extremely high porosity. Moreover, it should be

mentioned that the filtration efficiency of the aligned porous aerogel filters prepared by freezing at -20 °C is still reasonably high with a fairly low pressure drop. This implies that a much higher freezing temperature than -196 °C may also give desired microstructures. In short, the high filtration efficiency for ultrafine particles and low ΔP of the honeycomb-like aerogels, as well as their tailorability through facile adjustment of porosity, pore size, cell wall thickness and filter thickness, make the aerogels very attractive for filtration applications.
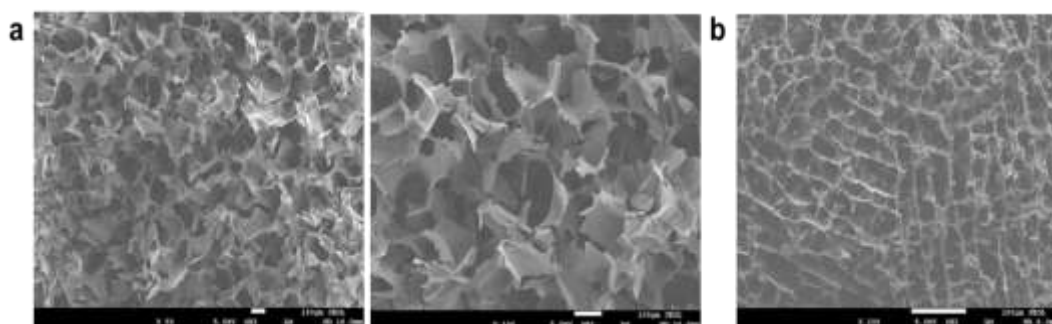
Figure 5. 8 SEM images of the wood-like A-lignin-based aerogels prepared from different frozen temperature: (a) -20 °C and (b) -196 °C.

Testing condition such as the wind velocity in the testing system can also affect the filtration performance, as shown in Figure 5.9a. Higher testing wind velocity results in higher air flow resistance and lower filtration efficiency. The filtration efficiency can be reduced from 99.85 to 99.62 % with a wind velocity increased from 5.3 to 14.1 cm/s due to the decreased residence time of air pollutants in the filters, and the ΔP is increased from 45 to 132 Pa. Figure 5.9b shows the comparison of the filtration performance in terms of filtration efficiency, ΔP, and calculated quality factor (QF) of the honeycomb-like aerogels with those of commercial filters, including high-efficiency air filters (H13 and H11), medium-efficiency filters (F7), and low-efficiency filters (G4), tested under the same condition (wind velocity is 10.0 cm/s). The quality factor (QF) is used to assess the overall filtration performance of the air filters, which can be calculated using equestion $QF = -(\ln(1-\eta))/\Delta P$, where η is the filtration efficiency [20-23]. The specifications of these reference filters are given in

Figure 5.10 and Table 5.2. Compared with G4, F7 and H11 filters, our aerogels can be tuned to achieve a higher filtration efficiency with a similar ΔP or a comparable filtration efficiency with a smaller ΔP, and hence a higher QF value. In comparison with H13 filters with a relatively high filtration efficiency (99.67 %) and ΔP (91 Pa), our aerogels exhibit filtration efficiency of 99.75 % at a ΔP of 90 Pa, thus a higher QF value is achieved. In addition, despite the much larger thickness (8-12 mm) of the honeycomb-like aerogels, their ΔP is significantly lower than or comparable to those of commercial filters or most air filters reported in literature. As discussed earlier, the aerogels with large thickness of 8 to 12 mm could exhibit ΔP of lower than 40 Pa at a wind velocity of 5.3 cm/s, which is in contrast to some reported fibrous filters such as thin polyacrylonitrile/silica nanofibrous membranes that has ΔP of 117 Pa at the wind velocity of 5.1 cm/s [24], bead-on-string poly(lactic acid) fibrous membranes with ΔP of 165 Pa at the wind velocity of 5.8 cm/s [25], and a 20-μm-thick polyamide nanofiber membrane with ΔP of 111 Pa at the wind velocity of 1.92 cm/s [26]. The excellent air permeability of our honeycomb-like aerogels can be ascribed to their highly porous structure and aligned pore channels.
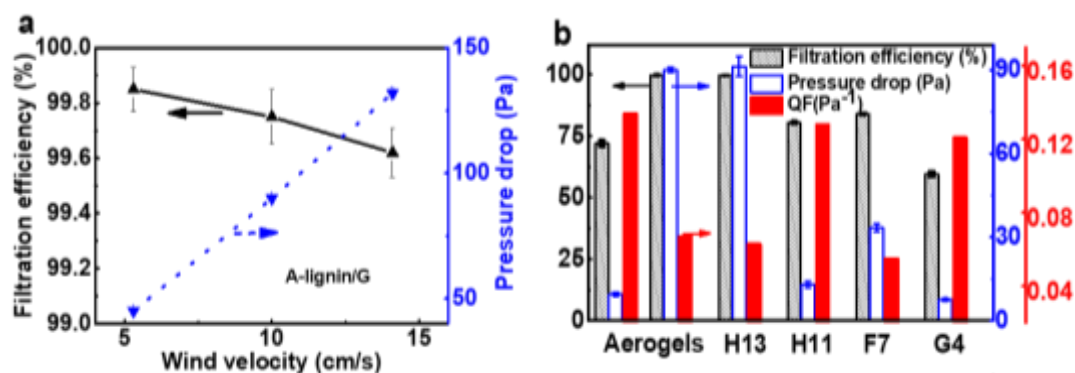
Figure 5. 9 (a) Filtration efficiency and pressure drop of 5.0 wt% A-lignin/G aerogels at a thickness of 8 mm under various wind velocities. (b) Comparison of the filtration efficiency, pressure drop, and QF of A-lignin/G aerogels (the left data is obtained from 1.1 wt% A-lignin/G aerogels at a thickness of 3.6 mm, and the right one is obtained from 5.0 wt% A-lignin/G aerogels at a thickness of 8 mm) and commercial air filters (H13, H11, F7 and G4) at wind velocity of 10.0 cm/s.
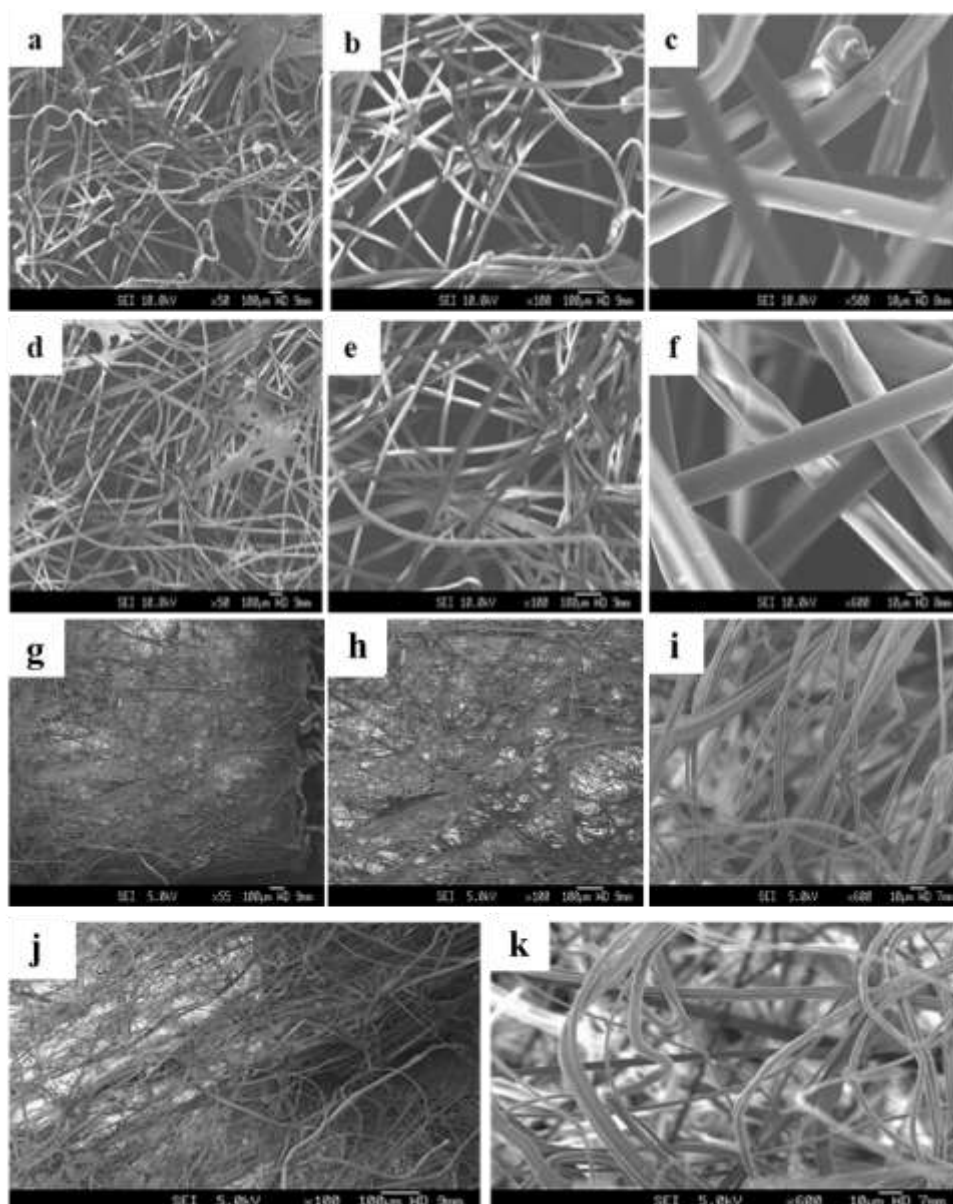
Figure 5. 10 SEM images of (a-c) G4, (d-f) F7, (g-i) H11, and (j-k) H13 filters.

Table 5. 2 Characterization results and filtration efficiency to ultrafine PM particles at a wind velocity of 10.0 cm/s.

Samples	Average diameter (µm)	Density (mg/cm³)	Thickness (mm)	Pressure drop (Pa)	Measured filtration efficiency
G4	22.75 ±3.20	28.8	3.6	7.5	59.5 %

F7	19.25±1.71	32.6	6.0	33.4	84.0 %
H11	4.67±3.06	159.7	0.45	13.0	80.2 %
H13	2.35±1.82	275.5	0.9	91.3	99.67 %

Figure 5.11a shows the filtration efficiencies of the honeycomb-like aerogel and H13 HEPA filters as a function of filtration time (up to 600 min). The unique morphological and surface chemistry characteristics of the lignin-based aerogels give rise to excellent filtration efficiency over a long period of time as the adsorption on lignin-based cell walls is mainly dependent on the affinity of the cell walls to the test particles that are composed of polar organic compounds. By contrast, although HEPA filters exhibit high filtration efficiency initially, the efficiency decays fairly fast, which is similar to that reported by Souzandeh et al [27]. The likely reason is that the deposited particles diminish the electrostatic effects of the HEPA filters that are made of glass fibers. Figures 5.11b and c show the morphology of the aerogels after the adsorption of the pollutant gas generated by burning incense. Apart from the well retained pore channels and cell walls, abundant adsorbed particles with similar size to that of the test particles are observed, showing the capability of the honeycomb-like aerogels for efficient adsorption of fine and ultrafine particles. From Figure 5.11b, we can also deduce that the adsorption on cell walls would not easily cause pore-clogging. By contrast, the high fiber packing density of HEPA filters may easily cause clogging of small pores [8, 27]. In short, the long-term filtration performance and clogging-resistant potential of our honeycomb-like aerogels make them appealing to high-capacity air filtration applications.
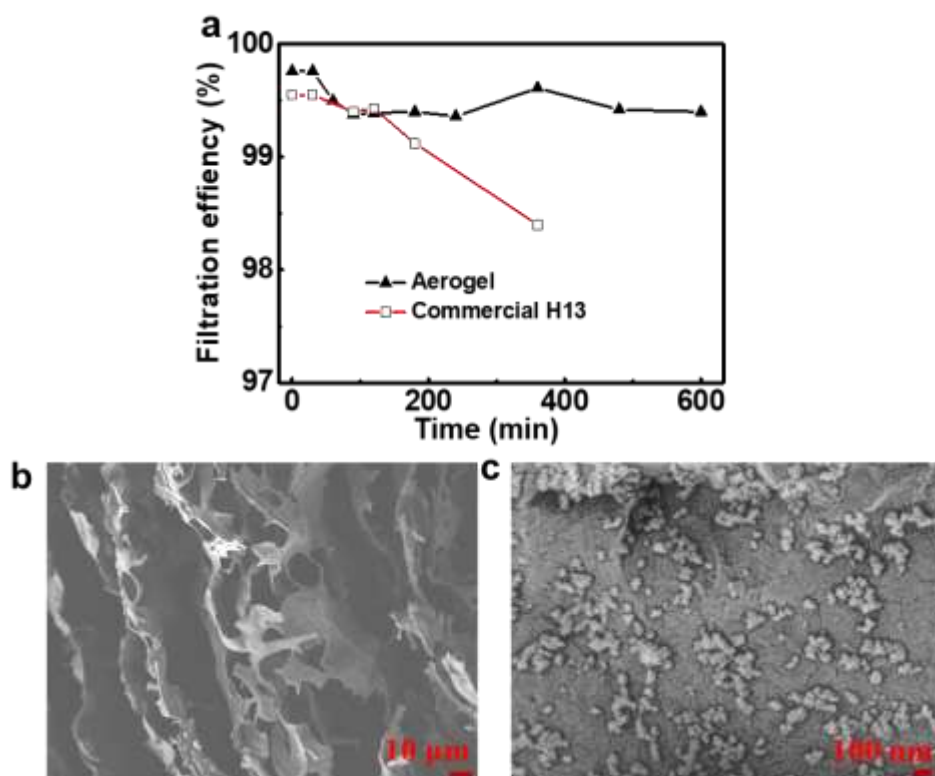
Figure 5. 11 (a) The filtration efficiency of the aerogels and H13 filters as a function of filtration time. The microstructure of the wood-like aerogels after adsorption of model pollutant particles: (b) the well retained pore channels and cell walls and (c) the adsorbed particles.

In order to better understand the filtration mechanism of this new class of aerogels, model particles with dominant size of 0.1, 0.2, 0.3, 0.5 and 1.0 µm are used in the filtration tests (Figure 5.12a). Obviously, the filtration efficiency behavior of the honeycomb-like aerogels is distinctly different from that of H13 HEPA filters (Figure 5.12b), which are made of randomly entangled microfibers [8, 27-28]. For the HEPA filters, the dominant filtration mechanism for ultrafine particles with size of ≤ 0.1 µm is diffusion. The ultralfine particles show significant Brownian diffusion (random motion caused by the collision with gas molecules), leading to its relatively high capture efficiency. However, the particles with size of ≥ 0.5 µm can also be captured easily because of interception and inertial impaction (the particles directly impinge onto the fibers instead of changing moving direction with the air flow). Thus

the particles with size of around 0.3 µm are the most penetrating ones for the conventional fibrous HEPA filters [29-31]. This is in general consistent with our tested results that the particles with sizes larger than 0.3 µm show significantly higher filtration efficiency than the 0.1-0.3 µm particles for HEPA filters. The roughly comparable efficiency for 0.1-0.3 µm particles is probably due to the use of organic model particles (less charged) in the tests. Unlike conventional fibrous filters that have random pores (Figure 5.10), our lignin-based aerogels have aligned pore channels with the lateral size of 20-40 µm. Thus, the filtration by the lignin-based aerogel filters is more dependent on diffusion mechanism, while the inertial impaction and interception play less important roles owing to the aligned pore channels. 0.1 µm particles tend to make random motion due to their collision with gas molecules, leading to a zig-zag motion path in the filter (Figure 5.12c). As a result, the probability of these particles interacting with the cell walls is high and therefore, the filtration efficiency for 0.1 µm particles is the highest. As the particle size increases, the particle mass and inertia increase, and hence the particles exhibit straighter and straighter motion path. Owing to the diminished diffusion mechanism, the probability of adsorption of relatively large particles on the walls of the aligned pores is lower, causing the decrease of filtration efficiency with increasing particle size in the range of 0.1-1.0 µm. Furthermore, it is observed that for the honeycomb-like aerogels with a relatively large thickness the filtration efficiency decreases only slightly with increasing particle size (in the range of 0.1-1.0 µm). For example, the filtration efficiency only reduce from 99.75 % for 0.1 µm particles to 99.16 % for 0.5 µm particles and 99.10 % for 1.0 µm particles. This may be attributed to the longer pore channels that could increase particle residence time and hence capture more particles with a relatively small degree of Brownian motion. Therefore, it can be concluded that excellent filtration efficiency for PM particles with a wide range of particle size can be achieved by adjusting the processing parameters in the preparation process. It is worth noting that the trend we observed for air filters with aligned channels, i.e., efficiency decreases with particle size, is supported by experimental and simulation work reported by Sibanda et al. for cross-flow filtration, which showed that that finer particles have higher tendency to be deposited on the

filter wall when the pore channels were "more opened" under low cross-flow ratios [12]. Thus, our results also demonstrate that microstructures of the filters can affect the filtration mechanism. The air filters with aligned channels can more effectively capture smaller particles in Brownian motion at a low pressure drop, improving quality factor of the filters. This work hence provides a new avenue for the design of high-performance air filters for applications where the targeted pollutant particles are smaller than 1 µm. They may also be combined with HEPA filters for improving filtration efficiency for ultrafine particles.
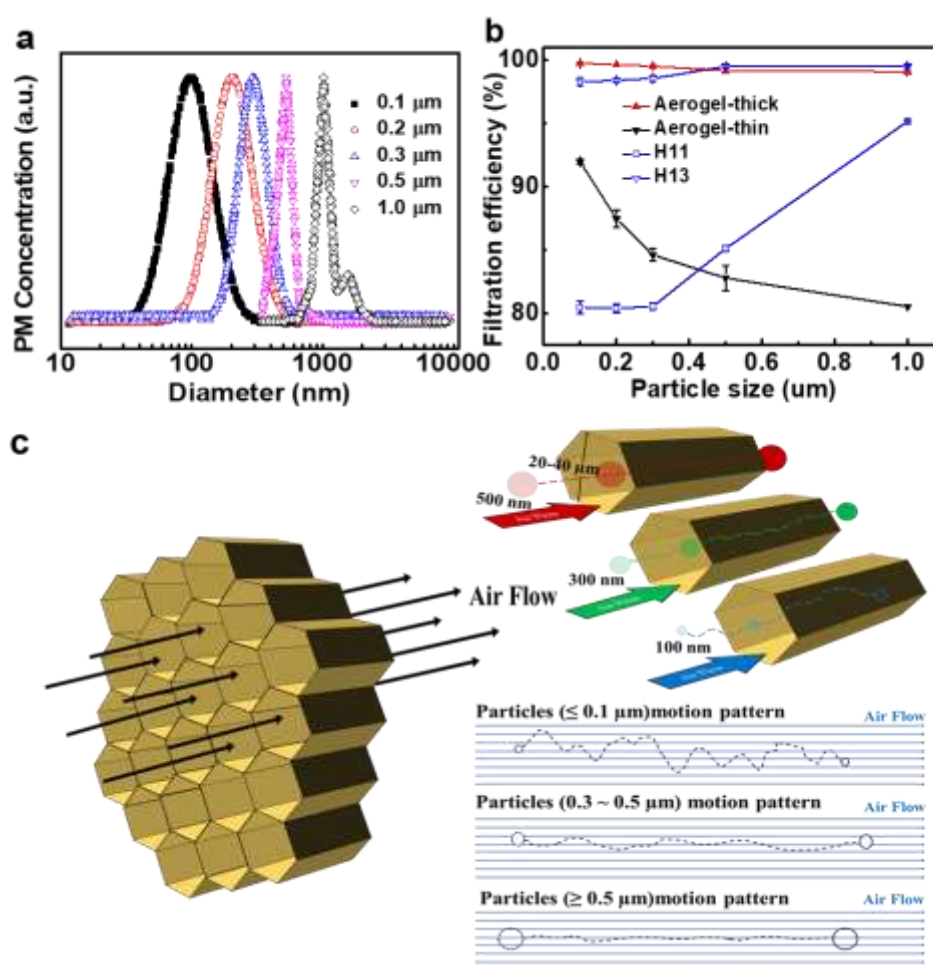
Figure 5. 12 (a) Size distribution curves of model pollutant particles generated from the aerosol generator with peaks at around 0.1, 0.2, 0.3, 0.5 and 1.0 μm, respectively. (b) Filtration efficiency of the wood-like aerogels (the thick and thin aerogels are 5.0 wt% A-lignin/G aerogels at a thickness of 8 and 3.8 mm, respectively) and HEPA

filters (H13 and H11) for the particles. (c) Schematics illustrating filtration mechanisms of the wood-like aerogels for particles of different sizes.

5. 4 Conclusion

In this chapter, a type of honeycomb-like aerogels with composite cell walls composed of cross-linked lignin and a small fraction of graphene, and aligned micrometer-sized pores are readily fabricated via facile unidirectional ice-crystal-induced self-assembly followed by low-temperature annealing. The specially designed aligned pore channels improve the ease of air flow, efficiently reducing the ΔP of the aerogels in filtration. The low-cost, readily available and renewable biomass, lignin, could be effectively cross-linked via annealing at 300 ℃, which significantly enhances mechanical strength, thermal stability and water/humidity resistance of the aerogels, while retaining abundant functional groups for adsorption of pollutant particles. Furthermore, the small amount of graphene layers doped in the cross-linked lignin enhance stiffness of the aerogels, reduce the volume shrinkage of the aerogels during the cross-linking process and improve the microstructures, ultimately reducing the pressure drop of the honeycomb-like aerogels and making the aerogels mechanically robust. In short, the microstructures of the aerogel filters, including their porosity, pore size, cell wall constituent and thickness, as well as their macroscopic shapes, can be easily adjusted to tune the filtration efficiency and pressure drop. On a side note, it should also be mentioned that the production of GO involves the use of expensive, harsh chemicals and that the lignin/G aerogel is not made of entirely sustainable materials. Cheaper and renewable alternatives may be considered in order to realize the potential of such aerogels for practical filtration purposes. Nevertheless, the filtration test results show that the aerogel filters exhibit a combination of outstanding long-term filtration efficiency for ultrafine particles and low pressure drop, which are better than that of commercial HEPA filters. Furthermore, through the filtration tests with particles of various sizes, a unique air filtration behavior is demonstrated for the aerogels, offering a new avenue for design of sustainable high-performance filters.

References

1.   Qian, Z.; Wang, Z.; Chen, Y.; Tong, S.; Ge, M.; Zhao, N.; Xu, J., Superelastic and ultralight polyimide aerogels as thermal insulators and particulate air filters. *Journal of Materials Chemistry A* **2018,** *6* (3), 828-832.

2.   Kim, H.-S.; Hwang, D.-K.; Kim, B.-Y.; Baik, M.-Y., Cross-linking of corn starch with phosphorus oxychloride under ultra high pressure. *Food chemistry* **2012,** *130* (4), 977-980.

3.   Andersen, A.; Krogsgaard, M.; Birkedal, H., Mussel-inspired self-healing double-cross-linked hydrogels by controlled combination of metal coordination and covalent cross-linking. *Biomacromolecules* **2017,** *19* (5), 1402-1409.

4.   Li, Y.; Shao, H.; Lv, P.; Tang, C.; He, Z.; Zhou, Y.; Shuai, M.; Mei, J.; Lau, W.-M., Fast preparation of mechanically stable superhydrophobic surface by UV cross-linking of coating onto oxygen-inhibited layer of substrate. *Chemical Engineering Journal* **2018,** *338*, 440-449.

5.   Meador, M. A. B.; Alemán, C. R.; Hanson, K.; Ramirez, N.; Vivod, S. L.; Wilmoth, N.; McCorkle, L., Polyimide aerogels with amide cross-links: a low cost alternative for mechanically strong polymer aerogels. *ACS applied materials & interfaces* **2015,** *7* (2), 1240-1249.

6.   Suzuki, M.; Hanabusa, K., Polymer organogelators that make supramolecular organogels through physical cross-linking and self-assembly. *Chemical Society Reviews* **2010,** *39* (2), 455-463.

7.   Jiang, S.; Hou, H.; Agarwal, S.; Greiner, A., Polyimide nanofibers by "Green" electrospinning via aqueous solution for filtration applications. *ACS Sustainable Chemistry & Engineering* **2016,** *4* (9), 4797-4804.

8.   Deuber, F.; Mousavi, S.; Federer, L.; Hofer, M.; Adlhart, C., Exploration of ultralight nanofiber aerogels as particle filters: capacity and efficiency. *ACS applied materials & interfaces* **2018,** *10* (10), 9069-9076.

9.   Li, L.; Hu, T.; Sun, H.; Zhang, J.; Wang, A., Pressure-sensitive and conductive carbon aerogels from poplars catkins for selective oil absorption and oil/water separation. *ACS applied materials & interfaces* **2017,** *9* (21), 18001-18007.

10.   Pakula, T.; Trznadel, M., Thermally stimulated shrinkage forces in oriented polymers: 1. Temperature dependence. *Polymer* **1985,** *26* (7), 1011-1018.

11.   Zhang, S.; Sun, J.; Hu, D.; Xiao, C.; Zhuo, Q.; Wang, J.; Qin, C.; Dai, L., Large-sized graphene oxide/modified tourmaline nanoparticle aerogel with stable honeycomb-like structure for high-efficiency PM 2.5 capture. *Journal of Materials Chemistry A* **2018,** *6* (33), 16139-16148.

12.   Sibanda, V.; Greenwood, R.; Seville, J.; Ding, Y.; Iyuke, S., Predicting particle segregation in cross-flow gas filtration. *Powder Technology* **2010,** *203* (3), 419-427.

13.   Marcano, D. C.; Kosynkin, D. V.; Berlin, J. M.; Sinitskii, A.; Sun, Z.; Slesarev, A.; Alemany, L. B.; Lu, W.; Tour, J. M., Improved synthesis of graphene oxide. *ACS nano* **2010,** *4* (8), 4806-4814.

14.   Li, H.; Yuan, D.; Tang, C.; Wang, S.; Sun, J.; Li, Z.; Tang, T.; Wang, F.; Gong, H.; He, C., Lignin-derived interconnected hierarchical porous carbon monolith with large areal/volumetric capacitances for supercapacitor. *Carbon* **2016,** *100*, 151-157.

15.   Si, Y.; Wang, X.; Yan, C.; Yang, L.; Yu, J.; Ding, B., Ultralight biomass-derived carbonaceous nanofibrous aerogels with superelasticity and high pressure-sensitivity. *Advanced Materials* **2016,** *28* (43), 9512-9518.

16.   Zeng, Z.; Zhang, Y.; Ma, X. Y. D.; Shahabadi, S. I. S.; Che, B.; Wang, P.; Lu, X., Biomass-based honeycomb-like architectures for preparation of robust carbon foams with high electromagnetic interference shielding performance. *Carbon* **2018,** *140*, 227-236.

17.   Cao, J.; Xiao, G.; Xu, X.; Shen, D.; Jin, B., Study on carbonization of lignin by TG-FTIR and high-temperature carbonization reactor. *Fuel processing technology* **2013,** *106*, 41-47.

18.   Zeng, Z.; Jin, H.; Chen, M.; Li, W.; Zhou, L.; Zhang, Z., Lightweight and anisotropic porous MWCNT/WPU composites for ultrahigh performance electromagnetic interference shielding. *Advanced Functional Materials* **2016,** *26* (2), 303-310.

19.   Zeng, Z.; Jin, H.; Chen, M.; Li, W.; Zhou, L.; Xue, X.; Zhang, Z., Microstructure design of lightweight, flexible, and high electromagnetic shielding porous multiwalled carbon nanotube/polymer composites. *Small* **2017,** *13* (34), 1701388.

20.   Liu, C.; Hsu, P. C.; Lee, H. W.; Ye, M.; Zheng, G.; Liu, N.; Li, W.; Cui, Y., Transparent air filter for high-efficiency PM2.5 capture. *Nat Commun* **2015,** *6*, 6205.

21.   Xu, J.; Liu, C.; Hsu, P.-C.; Liu, K.; Zhang, R.; Liu, Y.; Cui, Y., Roll-to-roll transfer of electrospun nanofiber film for high-efficiency transparent air filter. *Nano letters* **2016,** *16* (2), 1270-1275.

22.   Wang, L.-Y.; Liya, E. Y.; Lai, J.-Y.; Chung, T.-S., Developing ultra-high gas permeance PVDF hollow fibers for air filtration applications. *Separation and Purification Technology* **2018,** *205*, 184-195.

23.   Wang, L.-Y.; Yong, W. F.; Liya, E. Y.; Chung, T.-S., Design of high efficiency PVDF-PEG hollow fibers for air filtration of ultrafine particles. *Journal of Membrane Science* **2017,** *535*, 342-349.

24.   Wang, N.; Si, Y.; Wang, N.; Sun, G.; El-Newehy, M.; Al-Deyab, S. S.; Ding, B., Multilevel structured polyacrylonitrile/silica nanofibrous membranes for high-performance air filtration. *Separation and Purification Technology* **2014,** *126*, 44-51.

25.   Wang, Z.; Zhao, C.; Pan, Z., Porous bead-on-string poly (lactic acid) fibrous membranes for air filtration. *Journal of Colloid and Interface Science* **2015,** *441*, 121-129.

26.   Liu, B.; Zhang, S.; Wang, X.; Yu, J.; Ding, B., Efficient and reusable polyamide-56 nanofiber/nets membrane with bimodal structures for air filtration. *Journal of colloid and interface science* **2015,** *457*, 203-211.

27.   Souzandeh, H.; Johnson, K. S.; Wang, Y.; Bhamidipaty, K.; Zhong, W.-H., Soy-protein-based nanofabrics for highly efficient and multifunctional air filtration. *ACS applied materials & interfaces* **2016,** *8* (31), 20023-20031.

28.   Xiong, Z.-C.; Yang, R.-L.; Zhu, Y.-J.; Chen, F.-F.; Dong, L.-Y., Flexible hydroxyapatite ultralong nanowire-based paper for highly efficient and

multifunctional air filtration. *Journal of Materials Chemistry A* **2017,** *5* (33), 17482-17491.

29.   Li, P.; Wang, C.; Zhang, Y.; Wei, F., Air Filtration in the Free Molecular Flow Regime: A Review of High-Efficiency Particulate Air Filters Based on Carbon Nanotubes. *Small* **2014,** *10* (22), 4543-4561.

30.   Barhate, R. S.; Ramakrishna, S., Nanofibrous filtering media: Filtration problems and solutions from tiny materials. *Journal of Membrane Science* **2007,** *296* (1–2), 1-8.

31.   Podgorski, A.; Bałazy, A.; Gradoń, L., Application of nanofibers to improve the filtration efficiency of the most penetrating aerosol particles in fibrous filters. *Chemical Engineering Science* **2006,** *61* (20), 6804-6815.

Chapter 6

Robust Three-Dimensional Nanofibrous Aerogels with Unidirectional Pores Bridged by Tangled Nanofibers as Highly Efficient and Anti-Clogging Air Filters

In this chapter, NFAs, consisting of electrospun cellulose nanofibers and lignin as cross-linking agent, endowed with preferably aligned micrometer-sized fibrous channels, prepared via a facile unidirectional ice-crystals-induced self-assembly and low-temperature annealing is reported. It is verified that the hyperbranched macromolecular nature of lignin could boost the extend of cross-linking, significantly enhancing the mechanical strength and elasticity, while at the same time could minimize the annealing-induced shrinkage to maintain a reasonably low ΔP. The cross-linking mechanism of cellulose and lignin is also discussed, with hydrogenation and dehydration reactions being highlighted as the main contributing factors. The filtration results suggest that the incorporation of nanofibers together with the aligned fibrous channels promote outstanding filtration efficiency over a wider range of particles accompanied with low ΔP, and heavy loading tests also indicate anti-clogging features of such NFAs. This work provides a new strategy to prepare robust and sustainable high-performing NFA air filters.

6.1 Introduction

The work presented in Chapter 5 showed that aerogels with unconventional honeycomb-like morphology could attain comparable ultrafine filtration efficiency to that of conventional HEPA-grade filters. Simultaneously, the highly porous structure and aligned pore channels of these honeycomb-like aerogels would result in excellent air permeability, leading to significantly lower ΔP. This remarkable synergistic effect on the overall filtration performance could effectively address the typical efficiency-ΔP trade-off problem of fibrous filters. In contrast to conventional fibrous filters, using test particles with various sizes from 0.1-1.0 µm, it was revealed that the filtration mechanism of honeycomb-like aerogels depends largely on the diffusion mechanism and particle size; ultrafine particles exhibits the strongest Brownian behavior and hence, the probability of the particles impinging onto the cell walls is higher, resulting in the highest filtration efficiency. Nevertheless, the large thickness of the filter and declining filtration efficiency for larger particle sizes limit the practical applications of such unconventional aerogels. Furthermore, even though it was revealed that a small addition of graphene could reinforce the structural rigidity and reduce thermally-induced shrinkage, the aerogel still lacks elasticity, which restricts the reusability of such aerogel filters. In addition, the incorporation of GO also raises some environmental concerns. Thus, aside from addressing the elasticity and environmental impact of the material, there is also a need to design the honeycomb-like aerogel such that the specific surface area for adsorption can be increased and thinner samples can be used, while at the same time not compromising too much on the ease of air flow to maintain a low ΔP.

In recent years, a different type of 3D NFA with aligned fibrous channels have been reported in the literature [1-4]. The high specific surface area of the nanofibers could promote high filtration efficiency over a wide range of particle sizes, while the aligned nanofibrous channels could give rise to a reasonably low ΔP. Such hierarchical porous structure is a combination of the aerogel designs introduced in Chapters 4 and 5, in which both designs could make up for their individual

shortcomings. So far, only few works on such NFA structures have been explored as air filters. For instance, Nemoto et. al reported a TEMPO-oxidized cellulose nanofibril aerogel-containing filter capable of achieving a high filtration efficiency (99.999%) with a ΔP of 348 Pa for 0.125 μm particles at a face velocity of 5.3 cm/s [2]. Nevertheless, a potential drawback of highly porous 3D aerogels, no matter with random or aligned pores, is their relatively poor structural stabilities, which hinders their practical applications as air filters due to the constant compressive force exerted by the airflow in the filtration process. This weakness may be overcome by introducing chemical and/or physical cross-links to improve the robustness of NFAs. For example, Qian et. al reported a novel polyimide (PI) aerogel filter with thermally induced cross-links, which demonstrated no deformation even after 1000 loading-unloading fatigue cycles [5]. Deuber et. al used a thermal cross-linking procedure to improve the mechanical stability of their pullulan/poly(vinyl alcohol) blend 3D NFA filters and rendered their NFAs water-insoluble [3], while they also showed the potential of the NFAs as deep-bed filters, which could accommodate much higher dust loadings than nanofibrous membranes (NFMs) without compromising the filter performance [3]. As mentioned in Chapter 5, amongst various reinforcement methods, thermal cross-linking has emerged as a more facile and cheaper method. However, it is widely known that the major drawback of this method is the annealing-induced shrinkage of the porous materials, especially at relatively elevated temperatures (> 500°C), which could induce pore size reduction or even pore structural change of the porous materials [6-8]. To minimize such unfavorable morphological change, a plausible approach is to introduce hyperbranched macromolecular cross-linking agents into the systems, which could act as spacers between the fibers to prevent highly porous 3D NFAs from collapsing into much denser structures. In addition, since the contacting area between adjacent nanofibers are expected to be small in general, the contact of hyperbranched macromolecules with nanofibers may also boost cross-linking reactions. Nevertheless, so far the cross-linking agents employed are typically linear polymers [3, 9-11]. In addition, most of them are expensive and/or synthetic chemicals generated from non-renewable precursors, which hamper their practical applications and raises some environmental concerns [5, 12]. Therefore, there

is a need to identify a more economically viable and environmentally benign cross-linking agent that could make 3D NFA filters more robust and durable, while at the same time largely reduce the negative effect of the thermal cross-linking process on the morphology of the NFAs so that high filtration efficiency and low ΔP can be achieved simultaneously.

In the previous chapter, we introduced lignin, a biomass-based product that could potentially be used to fabricate high-efficiency aerogel filters. Another interesting fact of lignin is that it is also a type of hyperbranched natural macromolecules. In this chapter, we demonstrate that lignin could be used as an effective cross-linker for fabrication of lignin/cellulose-based 3D NFAs with preferably aligned pores and hierarchical porous structures, which exhibit both superior mechanical properties and ultrahigh porosities (> 99 %). The lignin/cellulose-based NFAs were fabricated via directional ice-templating and low-temperature annealing. The annealed NFAs show promising potential for the filtration of airborne PM particles of various sizes with remarkable filtration efficiency accompanied by low resistance to air flow. Unlike recently reported cellulose-based aerogels [13-16], by subjecting the as-prepared lignin/cellulose NFAs to low-temperature annealing, we revealed that the material shrinkage could be largely minimized, and hence the initial morphology of the NFAs could be largely retained after the annealing, minimizing the negative effect of thermal annealing on porosity and pore structures, which are essential for high filtration efficiency and low ΔP. Furthermore, our results also suggest that lower annealing temperatures could reduce the extent of material decomposition, retaining most functional groups for PM adsorption and also enabling a high yield of product. The relationship between the NFA morphology and filtration mechanism was also established, to further demonstrate the advantages of incorporating lignin. Long-term loading tests were also performed to validate the anti-clogging properties of the lignin-cross-linked NFAs. Through this work, it is believed that this facile cross-linking approach offers a new generic route to prepare highly efficient and robust NFA filters with clog-resistant properties.

6.2 Experimental

6.2.1 Materials

Cellulose acetate (CA, M_n = 50,000 g mol^{-1}), Kraft lignin, N,N-dimethylacetamide (DMAc, anhydrous, 99.8%), sodium hydroxide pellets were purchased from Sigma-Aldrich (Singapore) and acetone ($\geq$ 99.8%) was purchased from Fisher Scientific (U.K.). All reagents were used as received without further purification.

6.2.2 Preparation of Cellulose Acetate Solution for Electrospinning

14 wt% CA solution was prepared in a mixed solvent of acetone and DMAc in a ratio of 2:1 and left to stir overnight under room conditions. Then, the as-prepared CA solution was subjected to electrospinning, using a self-assembled electrospinning setup equipment, with an applied voltage of 15 kV, feed rate of 0.7 mL/h, working distance of 10 cm and the electrospun fibers were collected on a conductive collector for further processing. The electrospinning was run under room conditions with a relative humidity (RH) of 70-80%.

6.2.3 Fabrication of Cellulose/Lignin Aerogels

The as-spun nanofibers were then treated in a 0.5M NaOH solution to convert the acetate functional groups to hydroxyl groups, regenerating cellulose nanofibers in the process. Then, cellulose nanofiber suspension was prepared in deionized (DI) water and homogenized using an ultrasonic sonicator (Scientz-750F) to obtain a slurry with short electrospun nanofibers. A measured amount of Kraft lignin was also dissolved in DI water to prepare lignin aqueous suspension. Subsequently, the slurry and lignin solution were used to prepare 2 wt% cellulose/lignin (C/L) mixture in the ratio of 14:1. The C/L mixture was then casted in a cylindrical Teflon mold with a metal base immersed in liquid nitrogen (-196°C) to facilitate unidirectional freezing. Due to the insulating nature of the Teflon mold, the temperature gradient

created between the upper and lower sides of the C/L mixture is the main driving force for the unidirectional growth of ice crystals upwards. The frozen samples were then placed in a freeze-drier for 48 h to obtain the cellulose/lignin NFAs endowed with ice-crystal-induced aligned hierarchical porous channels and cell walls. The NFAs were further subjected to low-temperature annealing at 250°C under inert purified argon (99.9995%) atmosphere, in order to obtain robust cellulose/lignin NFAs. 2 wt% pure cellulose NFAs were also prepared based on the same methods to obtain annealed cellulose NFAs to be used as a reference for comparison. The same lignin suspension was also used to prepare pure lignin aerogels as reported in our previous work [17], which will be used as a reference for the thermogravimetric analysis of the cellulose/lignin NFAs.

6.2.4 Characterization

The morphology of the NFAs was studied under a field emission scanning electron microscopy (FESEM, JEOL 7600F) at an acceleration voltage of 5kV. The densities of the aerogels were estimated by evaluating the weighted mass and measured dimensions of the cylindrical-shaped aerogels. The porosities of the aerogels were estimated from the measured apparent densities of the NFAs and the corresponding bulk material (Porosity = $1-\rho_{NFA}/\rho_{Cellulose}$; $\rho_{Cellulose} = 1.5$ g/cm^3). The thermal stability of the aerogels was analyzed using a thermogravimetric analyzer (TGA, TA Instrument Q500). The functional groups involved with the cross-linking of NFAs were investigated with Fourier Transform Infared Spectrometry (FTIR, Perkin Elmer Spectrum One) in ATR mode. TGA-FTIR, using another TGA equipment (TA Instrument Q50) coupled with FTIR (Thermo Scientific, Nicolet iS10), was also conducted from room temperature to 300°C at a heating rate of 10°C/min using purified nitrogen (99.9995%) at a flow rate of 90 mL/min to maintain an inert atmosphere. All interferograms with adsorption spectra were collected during pyrolysis, and the spectrum scope was in the range of 600-4000 cm^{-1} with a resolution factor of 1 cm^{-1}. A tensile tester (Instron 5567) with a 10N load cell was

used to perform compression tests on the cylindrical-shaped NFAs and the compression rate adopted was 1.9×10^{-3} /s.

6.2.5 Air Filtration Test

In this work, the filtration tests were carried out in a similar method as reported in our previous works [17-19]. A schematic diagram of the testing facility is shown in Chapter 3. Briefly, also explained in Chapter 3, the model PM particles were generated by an aerosol generator (SLG 250, Topas), which utilizes diethylhexyl sebacate (DEHS) as the aerosol particles and the PM concentration was controlled by diluting the chamber with clean air down to a level equivalent to the hazardous pollution standard set by WHO (PM$_{2.5}$ ≥ 300 µg m^{-3}). The particle concentration was measured using an optical particle sizer (OPS 3330, TSI Instruments Ld) and a condensation particle counter (Nanoscan SMPS 3910, TSI Instruments Ld) before and after filtration and the data obtained was evaluated with a normalization software (MIM, TSI Instruments Ld) The pressure drop was measured using a differential pressure gauge (Digital Manometer, Bluewind Laboratory Pte Ltd). The face velocities adopted in the filtration testing were 5 cm/s, 10 cm/s and 14 cm/s, calibrated using an air velocity meter (Airflow instruments velocity meter TA430, TSI Instruments Ld). Stability tests were carried out under a constant compressive force (face velocity = 5 cm/s) for 40 h at RH 60%.

6.3 Results & Discussion

6.3.1 Morphologies and Mechanical Properties of the NFAs

The general fabrication method for the cellulose/lignin nanofibrous aerogels (CLNFAs) is shown in Figure 6.1a. In brief, the CLNFAs were first prepared via electrospinning of cellulose acetate (CA) nanofibers followed by the alkaline hydrolysis of the ester group to regenerate cellulose nanofibers and then homogenized into shorter strands of nanofibers to create a uniform aqueous

suspension. With the addition of a small amount of lignin suspension into the fiber suspension, unidirectionally aligned fibrous channels with hierarchical porous structures can be created via directional freezing with a temperature gradient followed by freeze-drying to form the CLNFAs. Subsequently, the CLNFAs were subjected to a low-temperature thermal treatment to obtain annealed CLNFAs (A-CLNFAs). The morphologies of the CLNFA and A-CLNFA are illustrated in the schematic diagram in Figure 6.1bi and shown in the FESEM images in Figure 6.1bii to iv. The top views of the NFAs (Figures 6.1bii and iv) resemble that of a typical honeycomb structure, while in the cross-sectional views we could observe aligned fibrous channels (Figures 1biii and v), which are dissimilar to commonly reported honeycomb-like nano- and micro-structured materials with solid cell walls [20-22]. At a larger magnification, it could be clearly seen that apart from the primary pores (few microns) formed simply due to fiber entanglement, the growth of ice-crystals during freezing also generated aligned secondary pores with lateral size of 50-120 µm (Figure 1c). It is also interesting to note that within these secondary pores, there are still loose fibers hanging from the cell walls, which intertwined and entangled to form pores with sizes that lies between that of the primary and secondary pores. Such hierarchically structured porosity of the NFAs could provide a larger specific surface area for PM adsorption, while simultaneously keeping ΔP low owing to the low fiber packing density in the preferably aligned secondary pores.
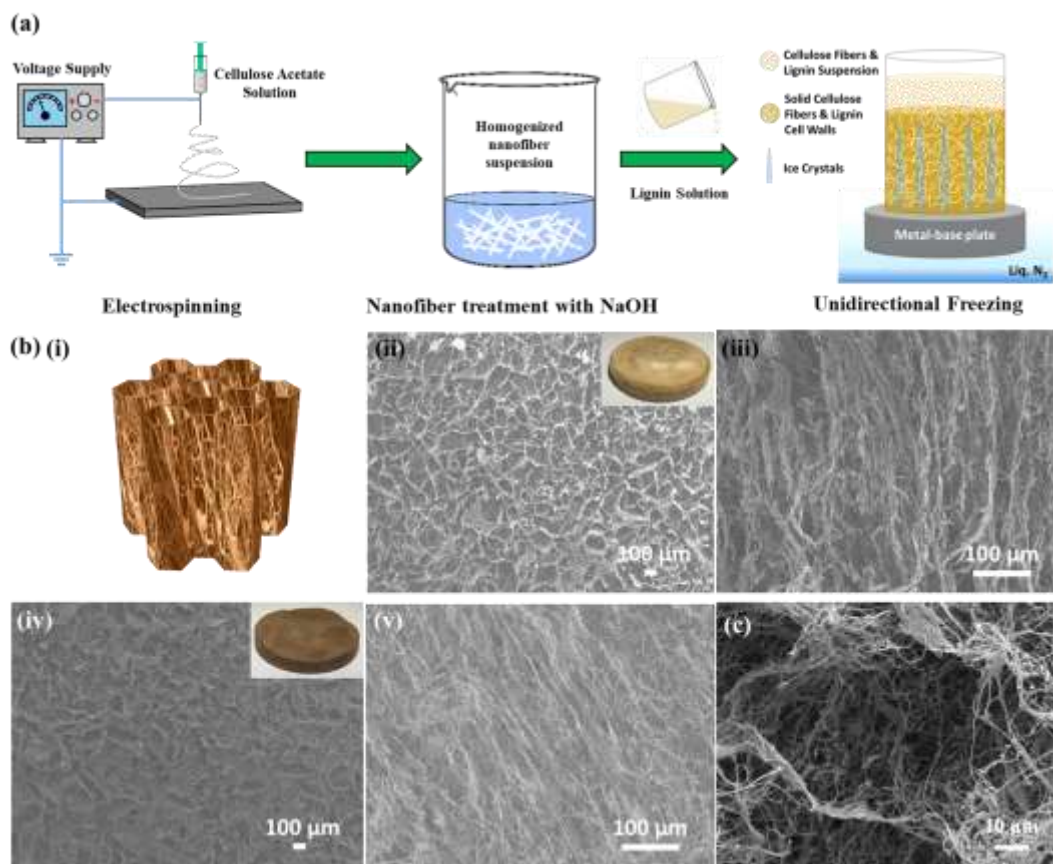
Figure 6. 1 (a) Schematic diagram of the NFA fabrication process. (b) (i) Schematic illustration of the as-prepared freeze-dried NFA. FESEM micrographs of the top view and cross-section of NFA (ii & iii) before (CLNFA) and (iv & v) after (A-CLNFA) annealing, respectively. The insets in b(ii) and (iv) are the digital photos of CLNFA and A-CLNFA, respectively. (c) FESEM micrographs of the primary and secondary pore structures of a single fibrous channel of the NFAs.

As mentioned in the introduction section, lignin was added in as a cross-linker to improve the mechanical robustness of the material in order to withstand constant compressive forces during air filtration. In order to validate this hypothesis, cylindrical-shaped CLNFA and A-CLNFA were prepared and subjected to compression tests. Similarly-shaped cellulose NFAs, in unannealed (CNFA) and annealed (A-CNFA) forms, were also prepared to be used as references for the compression tests. The resultant apparent stress-strain curves are shown in Figure 6.2a. The apparent compression moduli of the various NFAs could be estimated from

the initial, relatively straight parts of the compression curves (strain < 30%). The compression curves demonstrate that the compression moduli of the CLNFA (155 Pa) and A-CLNFA (61 Pa) are greater than that of CNFA (63 Pa) and A-CNFA (44 Pa), respectively, confirming that the addition of lignin does improved the robustness of the NFAs. Since A-CNFA and A-CLNFA used in the compression test possess similar fiber diameters and porosities (Table 6.1), it is obvious that the extent of cross-linking in A-CLNFA is greater than that of A-CNFA. Nonetheless, the insets in Figure 6.2a indicate material shrinkage as a result of the thermal cross-linking treatment. The shrinkage could result in morphological changes within the material such as the pore size and porosity, which may in turn affect the drag force across the NFA filters. Thus, it is obvious that there exists a trade-off relationship between the mechanical properties and ΔP of the NFA filters. Figure 6.2b-e shows the top view and cross-sectional morphologies of CNFA and A-CNFA. Table 6.1 also summarizes the average secondary pore sizes and porosities of CNFA, A-CNFA, CLNFA and A-CLNFA. It is apparent that the addition of a hyperbranched macromolecular cross-linking agent (lignin) can help to reinforce the structure of the NFA (Figure 6.1bii-v), minimizing the pore shrinkage, which may be beneficial in easing the air flow across the aerogel and hence, minimize the increase in ΔP. Contrastingly, with the absence of lignin, it is evident that the pore size of A-CNFA has shrunk significantly after the annealing process (Figure 6.2b-e and Table 6.1). The details of the material shrinkage on ΔP will be further discussed under the filtration performance in section 6.3.4. From the compression curves in Figure 6.2a, it is also interesting to note that the thermal treatment resulted in a reduction of the compression moduli of the NFAs, which could be attributed to the weight loss during the annealing process that resulted in slight reduction of NFA densities (Table 6.1). However, simultaneously, the elasticity of the NFAs is also improved greatly due to the cross-linking, allowing the NFAs to possess higher flexibility and is more likely to retain its initial shape when subjected to compressive forces. In order to further verify this improved elasticity, A-CLNFA was further subjected to repeated compressions by a 150g calibration weight (Figure 6.2f), which is more than 5000 times the mass of the NFA and it demonstrated remarkable recovery of its original

height. Thus, such superior mechanical integrity of the A-CLNFA further demonstrate the potential of this material as durable air filters.
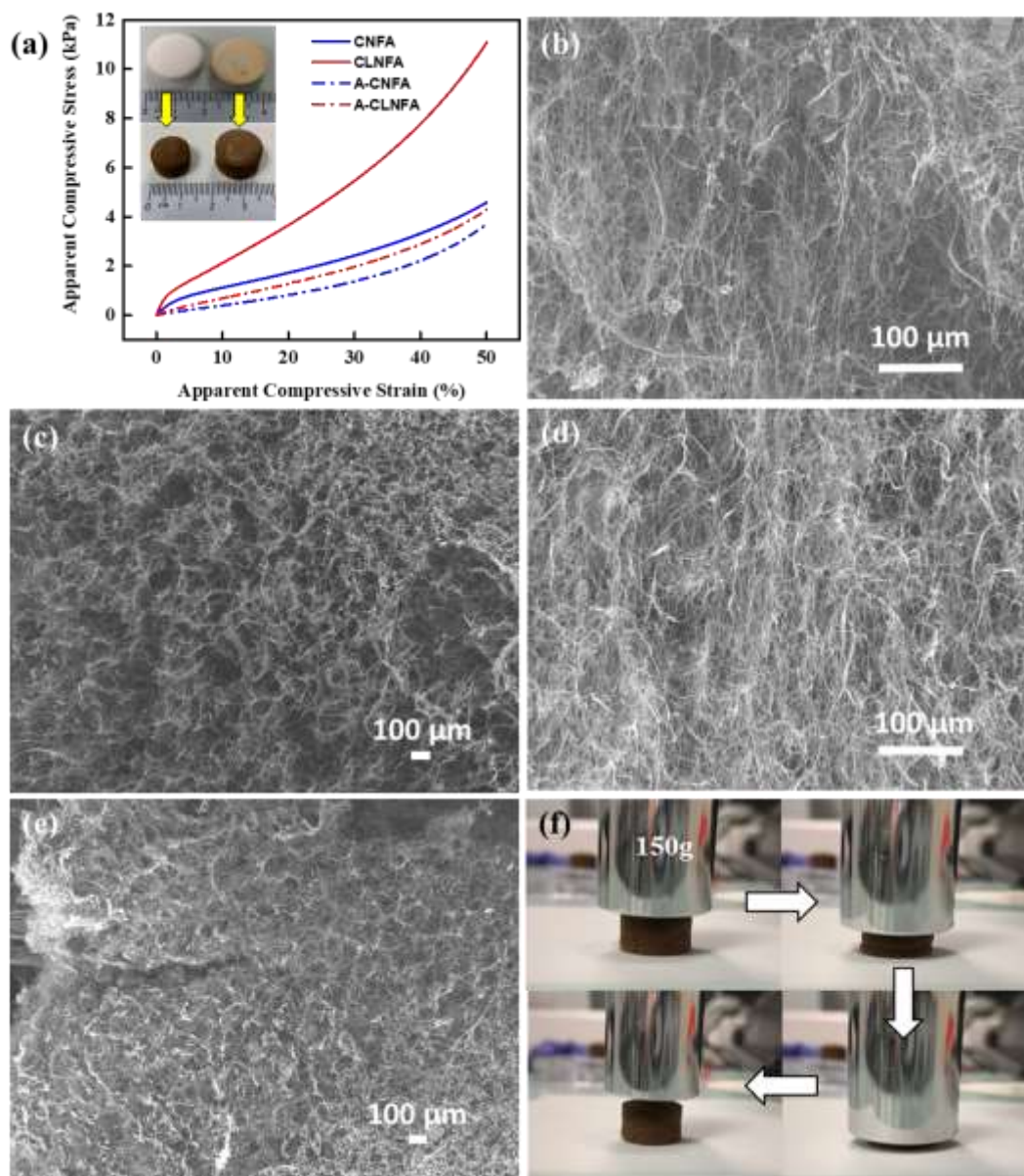
Figure 6. 2 (a) Typical apparent stress-strain curves of CNFA, CLNFA, A-CNFA and A-CLNFA. The inset in (a) is the digital pictures of CNFA and CLNFA (top), and A-CNFA and A-CLNFA (bottom) used in the compression tests before and after annealing, respectively. FESEM micrographs of the top view and cross-section of cellulose NFA (b, c) before (CNFA) and (d, e) after (A-CNFA) annealing,

respectively. (f) The compression process of an A-CLNFA using a 150g calibration weight.

Table 6. 1 Average fiber diameters, apparent densities, average secondary pore sizes and porosities of the various NFAs used for compression test.

Sample	Average Fiber Diameter (µm)	Apparent Density (mg/cm³)	Average Secondary Pore Size (µm)	Porosity (%)	Height (mm)
CNFA	0.362 ± 0.116	17.9	50-120	98.81	11.73 ±0.13
A-CNFA	0.186 ± 0.061	13.5	20-80	99.10	8.31 ±0.16
CLNFA	0.318 ± 0.099	20.3	50-120	98.65	11.60 ±0.21
A-CLNFA	0.229 ± 0.092	13.5	40-110	99.10	10.37 ±0.03

To further demonstrate the benefits of incorporating lignin, the extent of cross-linking was further studied under FESEM and the results are presented in Figure 6.3. Unlike the cross-linking that takes place only at fiber contacting points in A-CNFA (Figure 6.3a and b), FESEM evidence also reveals that the lignin not only reinforce at fiber agglutination points but also occupy the spaces within the voids of adjacent fibers (Figure 6.3c and d), providing further evidence that the presence of hyperbranched macromolecular lignin could boost the extent of cross-linking within the NFA.
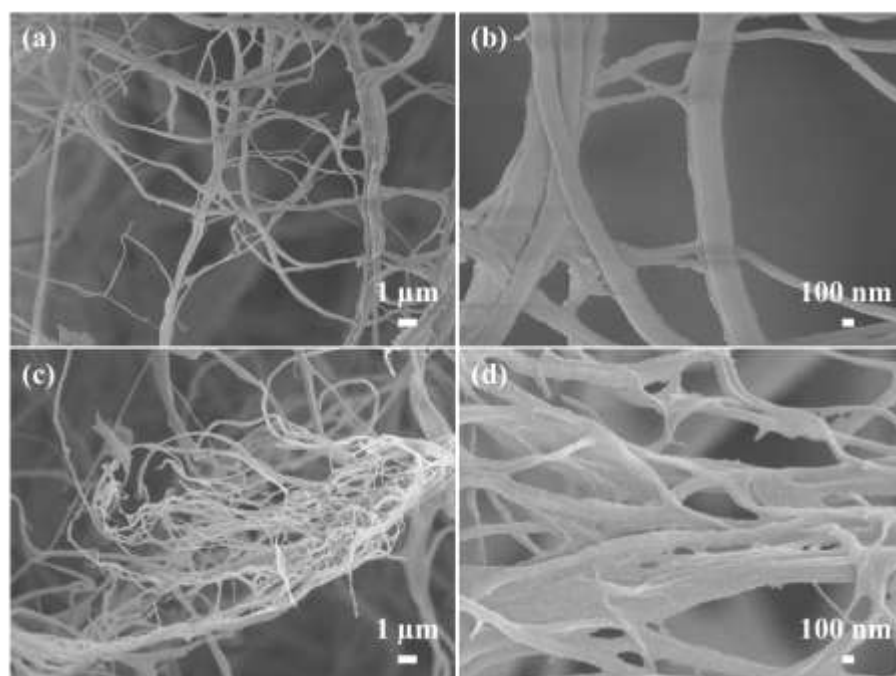
Figure 6. 3 FESEM images of the nanofibers in (a, b) CLNFA (before annealing) and (c, d) A-CLNFA (after annealing).

6.3.2 Cross-Linking Mechanism

Besides considering the effects of cross-linking on the morphology and mechanical properties, it is also important to understand the fundamental mechanisms that lead to the cross-linking process. In recent decades, extensive studies have been done to understand the pyrolysis of lignocellulosic biomass due to their promising potential as alternative energy sources (mainly bio-oil extraction) [23-26]. Nonetheless, the extraction of the different components in the biomass remains a challenge due to the complexed chemical compositions and network, which greatly affects the yield and purity of the products obtained. Although the quality of the pyrolyzed biomass products can be predicted to some extent by a simple additive law based on the individual conversion of each constituent, the reaction mechanisms that occur during pyrolysis are still poorly understood. It is also reported in the literature that the reactor temperature and heating rate, which determine the reaction pathways, are correlated to the char production [27-28]. Yu et. al mentioned that low heating rates

facilitate cross-linking reactions to take place due to the longer reaction time, indicating that the extent of cross-linking can be optimized by choosing an appropriate heating rate during the annealing process [28]. Many researchers have attempted to explain the chemical interactions of the three main lignocellulosic biomass components (lignin, hemicellulose and cellulose) individually and combined as a mixture, but most mainly focused on pyrolysis at temperatures above 500°C to 1200°C with extremely fast heating rates, which may not be sufficient to explain the cross-linking mechanisms that took place during the low-temperature annealing of CLNFAs [29-32]. Furthermore, most literatures focused on the tar formation rather than on char formation. Therefore, in this work, based on the individual and combined pyrolysis of lignin and cellulose as well as reports from the literature, an elucidation of the cross-linking mechanism was attempted.

This study adopts a low temperature (250-300 °C) for the annealing process, and also a slow heating rate (2-5 °C/min) during the annealing process to maximize the extent of cross-linking while maintaining a relatively high yield of product. The pyrolysis of lignin and cellulose was investigated via thermogravimetric analysis (TGA)/ derivative thermogravimetry (DTG). In order to provide a more comprehensive comparison, pure lignin aerogels were also prepared to be used as a reference. The conditions of the TGA is set such that the environment emulates the annealing process in the tube furnace; 5 °C/min ramp rate to 110 °C and maintaining for 1 h to remove excess moisture, followed by ramping the temperature by 2 °C/min to 250 °C and maintaining for 2 h, then ramping the temperature to 300 °C at a rate of 2 °C/min. The TGA/DTG curves of the various aerogels are shown in Figure 6.4, in which all of the aerogels demonstrated two distinctive weight loss phases. As mentioned, the first weight loss from 50°C to 110°C is due to moisture evaporation. The next significant weight loss occurs at the isothermal temperature of 250°C with the CLNFA exhibiting the largest DTG peak, demonstrating that stronger chemical interactions occurred between lignin and cellulose than that of the individual components. It is also worth noting that some extent of cross-linking within the CLNFA is initiated when temperature rises above 200°C. Nevertheless, as the

temperature increases beyond 250ºC, the decomposition of cellulose increased sharply, while the CLNFA and lignin aerogel demonstrated relatively stable and low weight changes, indicating higher thermal stability at elevated temperatures. Intriguingly, the smaller DTG curve of CLNFA beyond 250ºC implies that the presence of lignin in CLNFA enhances the thermal stability of cellulose and promotes a larger yield of CLNFA at higher temperatures. This implication is further supported by the literature that lignin is known to melt and form agglomerates at temperatures a little over 100ºC, which can form char films that wrap around the cellulose surface, acting as a heat barrier, limiting mass transfer and providing good contact between pyrolysing components that promotes re-polymerization into gas and secondary char formation [28, 31] Furthermore, it is found from our experiments that the weight loss of cellulose is in fact much higher than that of the CLNFA, as shown in the inset in Figure 6.2a. Thus, it is obvious that the actual temperature of the tube furnace is in fact higher than 250ºC but lies somewhere between 250-300 ºC.
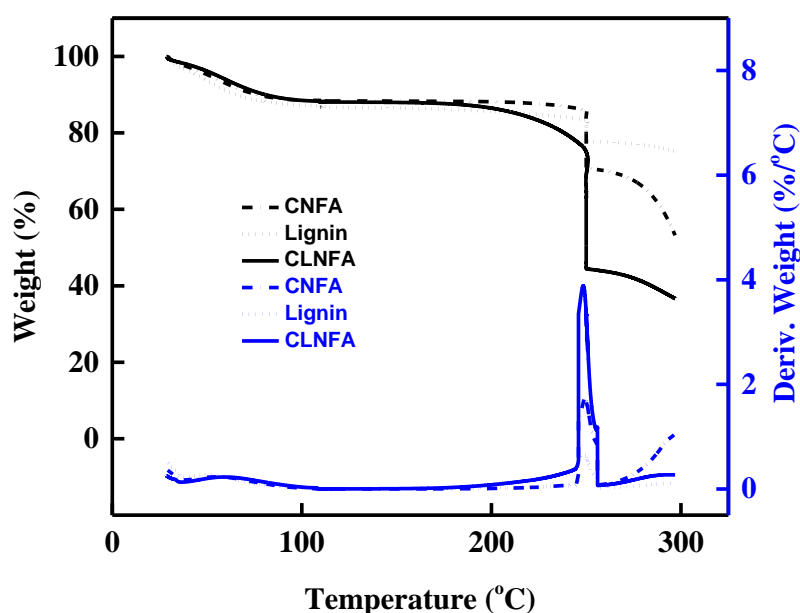
Figure 6. 4 Thermogravimetric traces of lignin aerogel, CNFA and CLNFA.

In order to identify the chemical species involved in the cross-linking process, the functional groups present before and after annealing were studied using FTIR, and TGA-FTIR have been performed to investigate the type of gaseous products that are released during the pyrolysis. The FTIR spectra (Figures 6.5, 6.6 and 6.7) confirm that most of the functional groups are retained even after the annealing process, which is crucial for PM adsorption. Since the annealing temperature fluctuates between 250-300°C, hence, the time-dependent 3D FTIR plot is provided within this temperature range.

Cross-Linking Mechanism in Cellulose

As shown in Figure 6.5a, it can be observed that the C-O ether stretching bands (1020-1061 cm^{-1}) and OH stretching band (3061-3636 cm^{-1}) are significantly reduced at 250°C, indicating the cleavage of C-O and OH bonds. This observation is in agreement with the literature as it was reported that depolymerization due to the rupture of glycosidic ether bonds can occur before 300°C, leading to the formation of levoglucosan, and dehydration reactions are the main driving force of thermal cross-linking reactions with H_2O molecules being released at temperatures as low as 200°C [27]. The new carbonyl peak of A-CNFA (1698 cm^{-1}) corresponds to the enol-keto tautomers formed during the chemical elimination of water from inter- and intra-molecular of cellulose chains [33]. The 3D FTIR plot in Figure 6.5b further confirms the release of H_2O molecules (3400-3800 cm^{-1}) during the annealing process. The C=O peaks (1758-1791 cm^{-1}) can be ascribed to the thermal degradation of the enol-keto tautomers, forming carboxyl groups, which can also fragment to give CO_2 (2308-2353 cm^{-1}) and CO (1072-1183 cm^{-1}) [33]. Cross-linking is define as the increase in the connection (physical/chemical interactions) within networks, thus, the main driving force of the cross-linking reactions in cellulose is dehydration as new covalent bonds are formed within and between cellulose chains.
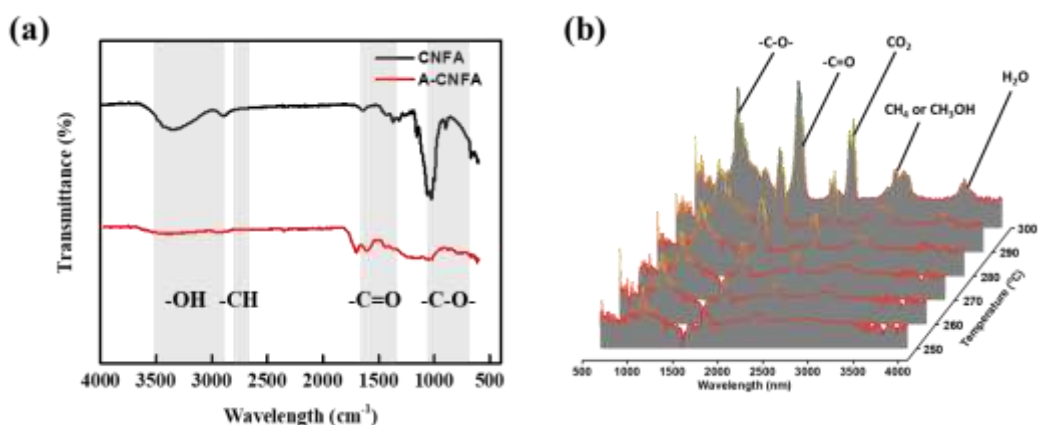
Figure 6. 5 (a) FTIR spectra of CNFA and A-CNFA. (b) 3D FTIR plot against temperature of the gaseous products released during annealing of CNFA.

Cross-Linking Mechanism in Lignin

On the contrary, lignin undergoes a different mechanism as compared to cellulose. The functional groups present before and after annealing at 250°C are presented in the FTIR spectra in Figure 6.6a. The decline in the C-O ether bands at 1038 cm⁻¹ and 1220 cm⁻¹ signifies the cleavage of the ether linkages within the three-dimensional structure of lignin. Interestingly, it is also widely reported that the (β- and α-) alkyl aryl ether linkages of lignin are the more reactive species within the complex three-dimensional network, playing a key role in the primary pyrolysis reactions, which resonates with our observation [27, 34-36]. Shen et. al also reported that the cleavage of the reactive aryl-alkyl-aryl ether bonds can give rise to side-chains with guaiacol-, syringol-, cresol-, catechol- and phenol-type derivatives, that may also take part in the cross-linking via dehydration reactions [34]. The 3D FTIR plot of the gas products released during the annealing process (Figure 6.6b) also indicates the loss of H_2O molecules (3429-3961 cm⁻¹), further reaffirming the occurrence of dehydration reactions. Furthermore, the strong aromatic (700-900 cm⁻¹) and C=O (1509-1541 cm⁻¹) bands can be attributed to the ether bond cleavage and phenolic-C_3 alkyl side chains, releasing small aromatic compounds and propanal respectively [30, 37]. The CO_2 band (2316-2378 cm-1) can be ascribed to the formation of oxygenated

141

compounds during the rearrangement of chemical groups as a result of the ether bonds cleavage [30, 38]. The weak broad band at 2878-2995 cm^{-1} also reveals the formation of methanol is being initiated from around 250°C-300°C onwards, signifying possible hydrogenation of methoxyl groups (-OCH$_3$) on the aromatic rings. To conclude, other than the cleavage of ether and carbonyl bonds, the elimination of water and hydrogenation of side chains appear to be the main cross-linking reactions, forming new covalent bonds within the lignin structure.
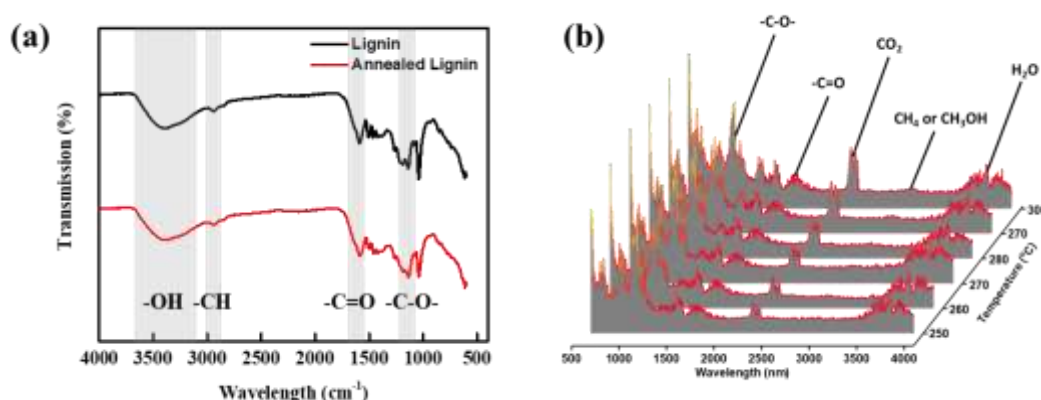
Figure 6. 6 (a) FTIR spectra of lignin before and after annealing. (d) 3D FTIR plot against temperature of the gaseous products released during annealing of lignin.

Cross-Linking Mechanism Between Cellulose and Lignin

The information derived from the individual annealing of cellulose and lignin is crucial in the comprehension of the cross-linking mechanisms of A-C/L NFAs. The FTIR spectra in Figure 6.7a show the prevailing functional groups before (CLNFA) and after (A-CLNFA) annealing, and the 3D FTIR plot in Figure 6.7b shows the temperature-dependency of the formation of gaseous products. It can be observed that the FTIR spectra of CLNFA and A-CLNFA are similar to that of cellulose (Figure 6.5a) but are dissimilar to that of lignin (Figure 6.6a), which can be attributed to the high cellulose-lignin ratio (14:1) in the CLNFA. Moreover, due to the presence of many oxygen-containing functional groups in both cellulose and lignin, strong

hydrogen bonds may be forged, over-shadowing the FTIR signals of lignin. Therefore, likewise, the FTIR spectra of A-CLNFA (Figure 6.7a) revealed the decline of both C-O (1033-1267 cm^{-1}) and OH (3031-3668 cm^{-1}) bands, suggesting similar fracturing of ether bonds and the occurrence of dehydration reactions; glycosidic bonds in cellulose and (β- and α-) alkyl aryl ether bonds in lignin. The supplementary 3D FTIR plot in Figure 6.7b also confirms the release of water vapor (3500-3900 cm^{-1}). Additionally, the prominent band occurring at 2813 cm^{-1} and 2899 cm^{-1} can be ascribed to the emission of methane or methanol, which may be attributed to the hydrogenation of the methoxyl (-OCH$_3$) group on the phenyl rings of lignin or the cracking of methylene (-CH$_2$-) side chains [34]. Also, the lack of aromatic peaks suggests that the reaction pathways have been altered significantly when lignin and cellulose are annealed together at 250°C, indicating that most of the benzene rings remain intact in the carbon backbone of lignin providing a more robust network. Furthermore, the 3D FTIR plot of the gaseous products of A-CLNFA is very much different compared to that of A-CNFA (Figure 6.5b) and A-PL (Figure 6.6b), suggesting that the dehydration and hydrogenation reactions also occur between cellulose and lignin.
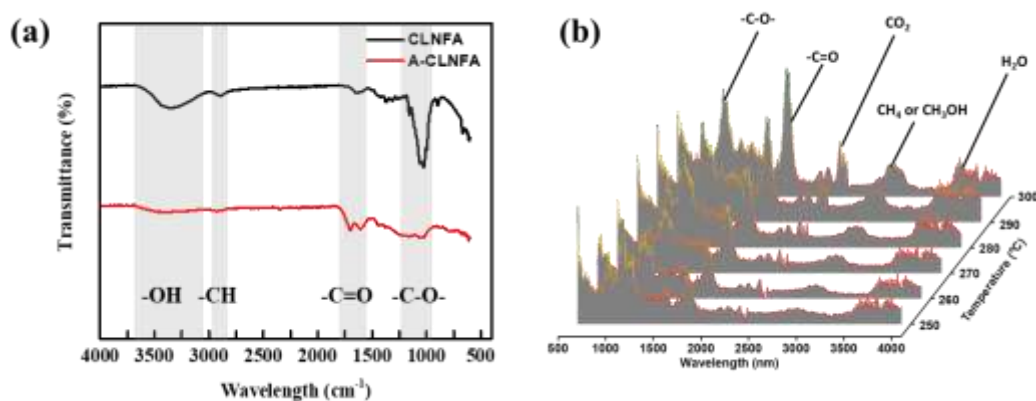

Figure 6. 7 (a) FTIR spectra of CLNFA and A-CLNFA. (b) 3D FTIR plot against temperature of the gaseous products released during annealing of CLNFA.

Therefore, based on our study and the literature, a schematic diagram of the possible cross-linking mechanisms that occur in the A-CLNFA during annealing at 250°C is shown in Figure 6.8. Since the ether bonds in lignin will be broken during annealing, it is assumed that the terminal side chains of lignin in the NFA will contain guaiacol-, syringol-, cresol-, catechol and phenol-type groups that are rich in hydroxyl groups. The scheme mainly depicts some possible dehydration and hydrogenation reactions that may occur between a hydroxyl group and any H-donor that come from either cellulose or lignin. Additionally, intra- and intermolecular dehydration of cellulose are also illustrated in the scheme, further highlighting that the cross-linking does not only occur between the two constituents but also within each constituent as well. Although not illustrated in Figure 6.8, it is also worth noting that other than dehydration and hydrogenation reactions, chemical transformations within the structures and strong hydrogen bonding also exists within/between the cellulose and lignin due to the large amount of hydroxyl, carbonyl and ether functional groups on both constituents.
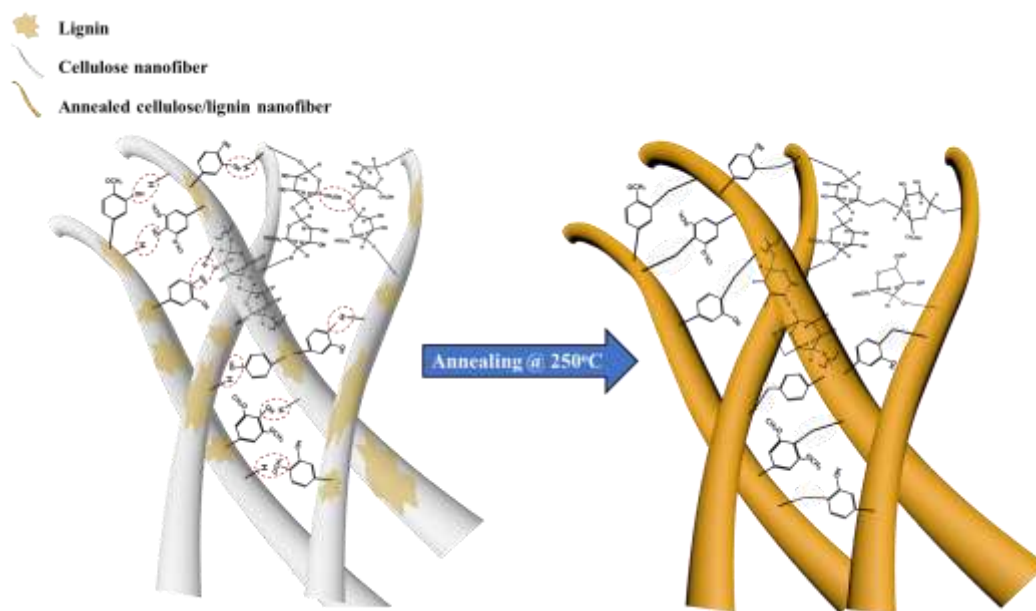
Figure 6. 8 Schematic diagram of the possible reaction mechanisms that occur during A-C/L NFA annealing at 250°C.

6.3.3 Anti-Clogging Properties of the NFAs

It was hypothesized that the multi-scale hierarchical porous structure formed from the ice-templates in the NFAs can introduce clog-resistant properties. In order to verify this feature of the NFAs, two types of A-CLNFAs were prepared and subjected to heavy loading test (Figure 6.9); one with isotropic morphology (iNFA) and with aligned fibrous channels (AFNFA). The iNFA was fabricated simply by freezing the sample at -20°C instead of using liquid nitrogen, in which the higher freezing temperature would allow larger ice crystals to form slowly and randomly within the NFA, causing the nanofibers to be randomly oriented in all directions (Figure 6.9a). Differently, the morphology of AFNFA shows the presence of both primary and secondary pores (Figure 6.9b). The apparent densities and filter thickness are presented in Table 6.2. It is also worthy to note that the iNFA was slightly denser and thicker than the AFNFA in order to achieve a comparable filtration efficiency to that of AFNFA. These NFA filters were then subjected to a continuous flow of 0.5 µm DEHS particles for 40 h (face velocity = 5 cm/s). The change in pressure drop and, the initial and final filtration efficiencies of AFNFA and iNFA were recorded, and shown in Figure 6.9c, respectively. It is apparent that the AFNFA does not clogged up as easily as the iNFA as seen in the FESEM micrographs in Figures 6.9a and b, suggesting that the aligned secondary pores of AFNFA allow for more deep-bed filtration, while the densely packed surface of iNFA gets clogged up more easily due to the higher fiber packing density and smaller pore sizes. Moreover, the greater amount of DEHS particles adsorbed (~39 g/m^2) further supports that AFNFA allows for a larger extent of depth filtration as compared to that of iNFA (~23 g/m^2). Additionally, due to such anti-clogging properties, the pressure drop of A-CLNFA remains relatively consistent even after 40 h of particle loading while at the same time maintaining a high filtration efficiency (Figure 6.9c). On the other hand, the pressure drop of iNFA significantly increased after 40 h of particle loading. Thus, it is clear that the aligned porous architectures could render the NFA filters with anti-clogging properties, which could extend the lifetime of the 3D NFA filters.
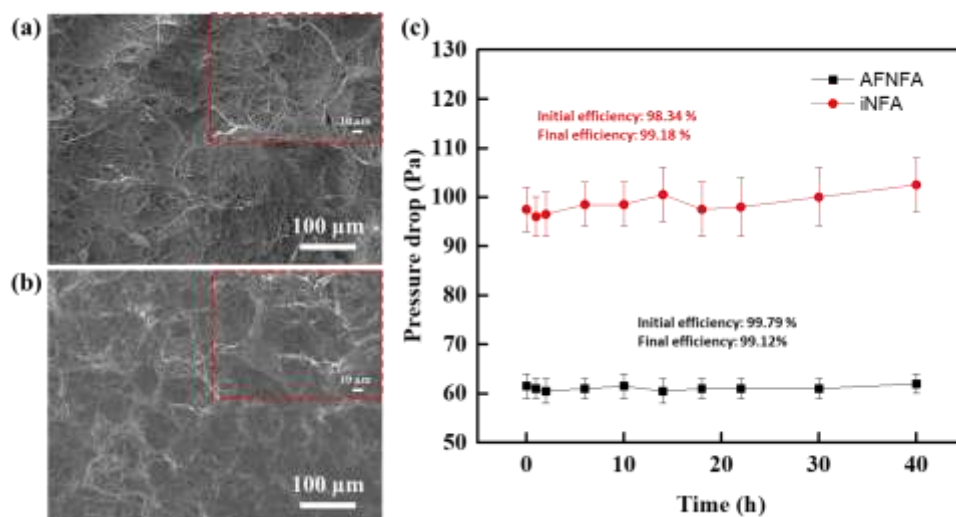
Figure 6. 9 FESEM micrographs of A-CLNFA with (a) isotropic morphology (iNFA) and (b) aligned fibrous channels (AFNFA) after 40 h of DEHS particle loading. (c) Long-term filtration performance of AFNFA and iNFA.

Table 6. 2 Thickness and apparent densities of the A-CLNFAs used for the heavy loading test.

Sample	Thickness (mm)	Apparent Density (mg/cm^3)
AFNFA	5.44	16.7
iNFA	6.47	37.8

6.3.4 Air Filtration Performance of the NFAs

The filtration efficiencies and pressure drops of the NFAs were explored using 0.1, 0.3, 0.5 and 1.0 µm DEHS particles generated via an aerosol generator (SLG 250, TOPAS), which simulates organic airborne particulate matter caused by biomass burning [39-40]. The number distributions of the generated DEHS particles are shown in Chapter 3. From the sharp peaks in the distribution curves, it is apparent that the

generated DEHS particles display a narrow size distribution around the desired particle sizes. Besides exploring the filtration efficiency and pressure drop, the quality factor (QF) of each NFA filter was also determined to assess the overall filtration performance of the filters. QF is defined as $- \ln (1-E)/ \Delta P$, where E and P denote the filtration efficiency and pressure drop across the filter respectively.

To demonstrate the benefits of lignin, both A-CLNFA and A-CNFA with comparable densities and thickness were prepared, with the latter acting as a reference. The filter thickness and their apparent densities are provided in Table 6.3. As shown in Figure 6.10, it is evident that the A-CLNFA possesses significantly lower ΔP than that of A-CNFA at the various tested face velocities (5, 10, 14 cm/s), with the ΔP amplifying proportionately with the surge of the face velocity. Besides the marginally lower apparent density of A-CLNFA (Table 6.3), the significantly lower ΔP could be attributed to the presence of a molecular cross-linking agent; lignin is the molecular cross-linker employed in this work. In order to verify this phenomenon, the cellulose/lignin (C/L) ratio was varied to investigate the effects of molecular lignin on the cell wall morphology of the aligned fibrous channels and the results are summarized in Figure 6.11a. The FESEM images show the morphologies of the cross-section of various A-CLNFAs with decreasing C/L ratio from (i) to (iv); lesser cellulose and more lignin within the NFA. It is apparent that the pores along the cell walls become more congested when the composition of lignin starts to dominate the NFA structure, creating more hollow fibrous channels in the process. This is further supported by the decreased in ΔP as the amount of lignin content increased (Figure 6.11b), demonstrating that the relatively hollow fibrous channels could give rise to lesser air resistance across the A-CLNFA filters. This occurrence could be ascribed to the molecular diffusion of lignin, which amplifies with the increasing proportion of lignin content that helps to guide more cellulose nanofibers towards the cell walls during the unidirectional freezing process. It is also interesting to note that the larger material shrinkage of A-CNFA could also be a contributing factor to the large ΔP as the smaller pore sizes (Table 6.1) could cause greater obstructions to the air flow and result in larger air resistance across the NFA filter.

Thus, owing to the presence of molecular lignin cross-linking agent, the larger and hollower fibrous channels could help to ease the air flow, which in turn minimizes the drag force across the A-CLNFA filter and hence reduce ΔP.

Table 6. 3 Average thickness and apparent densities of A-CLNFA and A-CNFA used in filtration test.

Sample	Average Thickness (mm)	Average Apparent Density (mg/cm^3)
A-CLNFA	5.35 ± 0.03	16.3 ± 0.6
A-CNFA	5.70 ± 0.26	18.0 ± 0.1
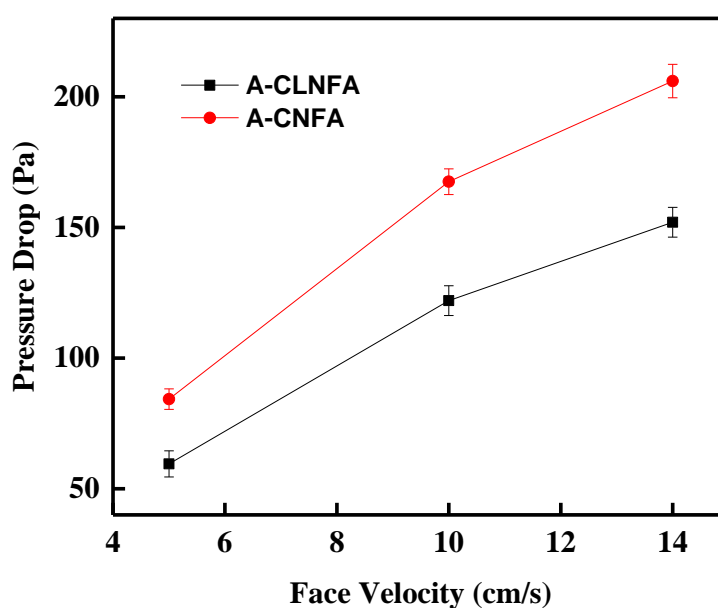
Figure 6. 10 Pressure drop of A-CNFA and A-CLNFA at various face velocities (5 cm/s, 10 cm/s and 14 cm/s).
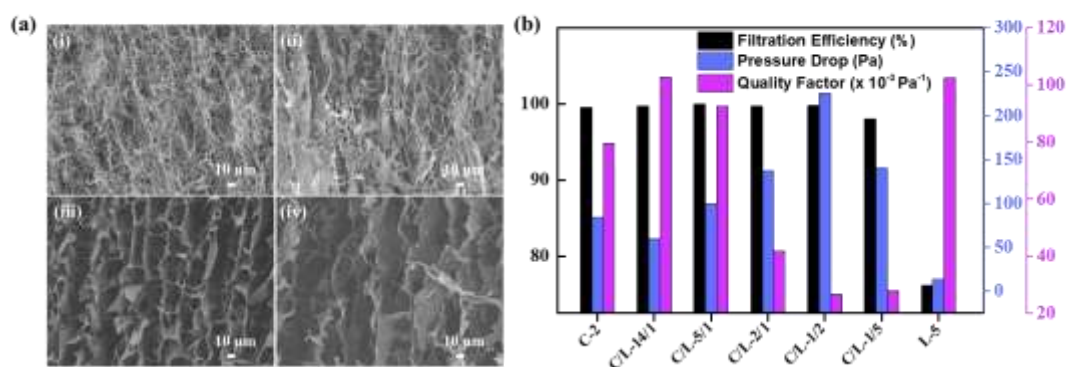
Figure 6. 11 (a) SEM images of the cross-section of the various NFAs with C/L ratio of (i) 14/1, (ii) 2/1, (iii) 1/2, and (iv) 0/1. (b) Filtration performance of the various A-CLNFAs with different C/L ratios for 0.3 µm DEHS model haze particles at face velocity of 5 cm/s.

In a typical fibrous medium, it is expected that a reduction in ΔP would ultimately decrease the filtration efficiency of the filter as this alteration in the filtration performance is often achieve via a smaller fiber packing density (smaller specific surface area for adsorption). Contrarily, in this work, the approach to reduce ΔP involves the manipulation of the positions and orientations of the cellulose nanofibers within the NFA structure. Hence, it is worthy to note that the effects of the molecular cross-linking agent on the NFA filtration efficiency and filtration mechanism have not yet been established. Therefore, the filtration efficiencies of A-CLNFA and A-CNFA for 0.1, 0.3, 0.5 and 1.0 µm particles were also investigated at various face velocities (5, 10, 14 cm/s) and the results are presented in Figure 6.12 and Table 6.4. It is evident that at face velocity of 5 cm/s, despite possessing a significantly lower ΔP, A-CLNFA displays similarly high filtration efficiency for 0.1 µm particles (99.86%) to that of A-CNFA (99.87%). Moreover, even though the A-CLNFA have a marginally smaller thickness and lower apparent density (Table S2), the filtration efficiencies for larger particles (0.3, 0.5 and 1.0 µm) have been demonstrated to be relatively higher than that of A-CNFA. The overall higher filtration efficiency of A-CLNFA could be ascribed to the presence of lignin in A-

CLNFA. Since lignin is commonly known to contain vast amounts of polar organic functional groups, these chemical groups may be instrumental to the adsorption of organic PM. On the other hand, from Figure 6.12, it is also obvious that the filtration efficiencies of both A-CNFA and A-CLNFA are particle size-dependent. Typically, in conventional fibrous filters with isotropic morphology (randomly oriented fibers), the filtration efficiency generally increases with particle sizes, in which the most penetrating particle size (MPPS) occurring around 0.3-0.5 µm where efficiency is the lowest [41-43]. It is worthy to mention that although NFA filters with aligned fibrous channels have been reported in the literature [3], the apparent density of the NFA is significantly larger (48 mg/cm^3), and therefore the filtration mechanism strongly resembled that of conventional fibrous filters. Differently, both A-CNFA and A-CLNFA prepared in this work, exhibited increasing filtration efficiency with smaller particle sizes, which is atypical of conventional fibrous filters. This anomaly could be attributed to the change in filtration mechanisms due to the significantly lower apparent densities (Table 6.3) and more hollow fibrous channels of A-CNFA and A-CLNFA. Schematic diagrams of the particle flow regimes in typical isotropic NFA filters (iNFA) and NFA with aligned fibrous channels (AFNFA) filters are illustrated in Figures 6.13a and b, respectively. It is widely known that the three main filtration mechanisms of fibrous filters for sub-micron particles are inertial impaction, interception and diffusion (Figure 6.13a). Inertial impaction occurs when a particle is so large (usually > 0.5 µm) that it is unable to adjust to the abrupt changes in the streamline direction, resulting in the collision onto nanofiber surface within a close proximity. Interception ensues when a particle (0.1-0.5 µm) following along the streamline comes within one particle radius from the nanofiber. Diffusion is the result of the erratic zigzagging Brownian motion of very small particles (< 0.1 µm) that causes collision onto the nanofiber surface. This flow regime typically governs the filtration mechanism of fibrous filters for sub-micron particles. Contrastingly, as reported in our previous work comprising of lignin-based aerogels with aligned solid channels [17], particles travel through micrometer-sized hollow channels (20-40 µm) with non-porous cell walls, in which the most effective filtration mechanism of PM is via the diffusion capture. Interception and impaction were otherwise demonstrated

to be less dominant due to the hollow nature of the filter channels. Similarly, at face velocity of 5 cm/s, both A-CNFA and A-CLNFA also demonstrated the highest filtration efficiency for the smaller 0.1 µm DEHS particles. Nonetheless, it is also intriguing to note that the filtration efficiency is the lowest for 0.3 µm DEHS particles, demonstrating that the MPPS lies close to this particle size, which is a characteristic feature of conventional fibrous filters. Since AFNFA possesses distinctive traits from both conventional fibrous filters and aerogels with aligned solid hollow channels, the filtration mechanism is a hybrid of that of these filters (Figure 6.13b).
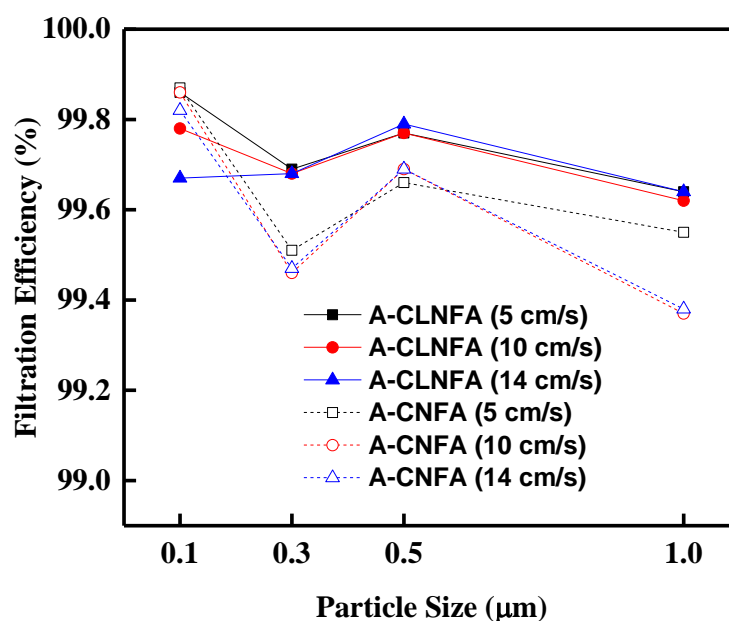
Figure 6. 12 filtration efficiencies of A-CNFA and A-CLNFA at different face velocities (5 cm/s, 10 cm/s and 14 cm/s) with 0.1 µm, 0.3 µm, 0.5 µm and 1.0 µm particles.

Table 6. 4 filtration efficiencies and pressure drop of A-CLNFA and A-CNFA for various particle sizes at different face velocities.

Sample	Face Velocity (cm/s)	Filtration Efficiency$_{0.1}$ (%)	Filtration Efficiency$_{0.3}$ (%)	Filtration Efficiency$_{0.5}$ (%)	Filtration Efficiency$_{1.0}$ (%)	Pressure Drop (Pa)

151

	5	99.86 ± 0.08	99.69 ± 0.08	99.77 ± 0.03	99.64 ± 0.06	59.5 ± 5.0
A-CLNFA	10	99.78 ± 0.08	99.68 ± 0.12	99.77 ± 0.00	99.62 ± 0.01	122.0 ± 5.7
	14	99.67 ± 0.14	99.68 ± 0.09	99.79 ± 0.01	99.64 ± 0.01	152.0 ± 5.7
	5	99.87 ± 0.08	99.51 ± 0.08	99.66 ± 0.10	99.55 ± 0.19	84.3 ± 3.9
A-CNFA	10	99.86 ± 0.06	99.46 ± 0.10	99.69 ± 0.07	99.37 ± 0.19	167.5 ± 4.9
	14	99.82 ± 0.10	99.47 ± 0.04	99.69 ± 0.07	99.38 ± 0.17	206.0 ± 6.4
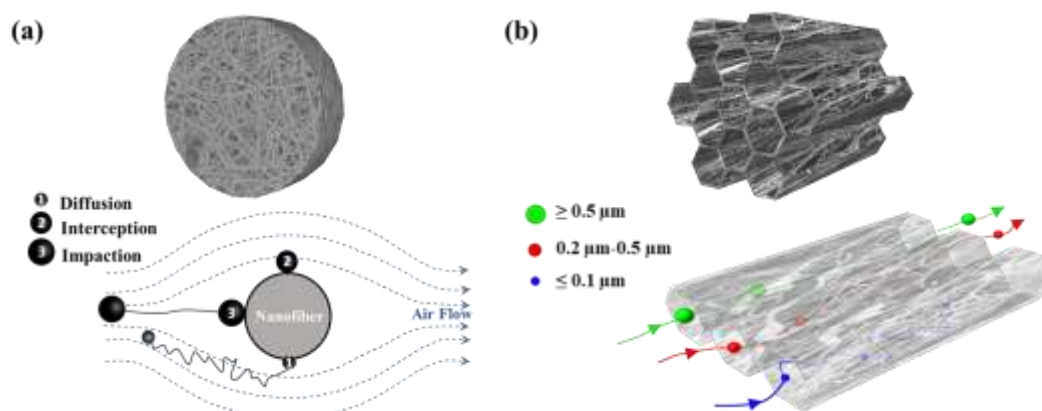
Figure 6. 13 Schematic diagrams of the particle flow regime in (a) iNFA and (b) AFNFA.

The face velocity is also an important parameter that may alter the mean free path of the airborne particles, which could eventually affect the ΔP and filtration efficiency of the NFA with (A-CLNFA) and without lignin (A-CNFA) (Figures 6.10 and 6.12). For A-CLNFA, it is obvious that the 0.1 µm particle filtration efficiency decreased significantly with increasing face velocity but the 0.3, 0.5 and 1.0 µm particle filtration efficiencies show little influence by the increase in flow rate. This could be ascribed to the much lighter mass of the ultrafine particles, which could take on a significantly straighter mean free path when subjected to a higher face velocity,

allowing the particles to penetrate through the aligned fibrous channels more easily. Another possible reason could be attributed to the lower fiber packing density within the secondary pores due to the addition of lignin, which creates slightly more hollow fibrous channels as compared to that of A-CNFA. Owing to the slightly more hollow structure, this would give rise to lesser obstruction to the flow of PM across the A-CLNFA filter, allowing the larger particles to pass through the NFA filter more easily. Since 0.5 and 1.0 µm particles possess much greater mass and inertia than ultrafine particles, the effect of face velocity on the mean free paths of these particles are less dominant, which may explain why the filtration efficiency is almost consistent even when face velocity was doubled or tripled. Hence, lower face velocities are favored to achieve higher overall filtration efficiency over a wider particle size range.

To further evaluate the overall filtration performance of the A-CNFA and A-CLNFA, the quality factors (QF) of the NFAs for different particle sizes were also tabulated and presented in Figure 6.14. It is evident that with the addition of lignin to cellulose, there seems to be a synergistic effect on the overall filtration performance; filtration efficiency increased simultaneously with the decrease in pressure drop. Moreover, A-CLNFA exhibits higher QF values for all the various tested particle sizes at all three face velocities adopted. Therefore, our results clearly demonstrate the benefits of the incorporation of lignin in the NFA. Thus, these unique aerogels exhibited remarkable filtration performance for ultrafine particles (< 0.1 µm) especially at lower face velocities. Although the addition of lignin is beneficial towards the filtration performance, it is also worthy to note that there exists an optimal C/L ratio that is crucial in achieving the optimal balance between filtration efficiency and ΔP (Figure 6.11b). Thus, in this work, the optimal tradeoff between efficiency and ΔP was determined to be C/L-14/1, which displays the highest QF value of 0.103 Pa^{-1} at face velocity of 5 cm/s.
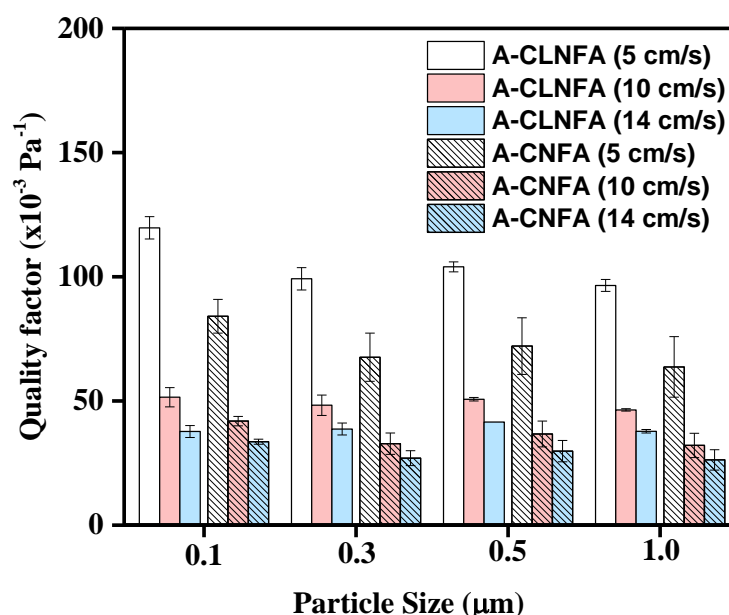
Figure 6. 14 Quality factors of A-CNFA and A-CLNFA for various particle sizes at different face velocities.

In order to further highlight the remarkable filtration performance of A-CLNFA, the filtration performance (filtration efficiency, ΔP and QF) of other aerogel filters reported in the literature and this work are summarized in Table 6.5. At relatively lower face velocities, the A-CLNFA filter shows a highly competitive filtration performance with comparably high filtration efficiency for ultrafine particles and much lower ΔP as well as the highest QF value. Therefore, this clearly demonstrates the potential of A-CLNFAs as filter materials to overcome the tradeoff between filtration efficiency and pressure drop especially for smaller particle sizes that are relatively more harmful.

Table 6. 5 Filtration performance of other aerogel filters reported in literatures and the A-CLNFA filter reported in this work.

Filter Type	Filtration Efficiency (%)	ΔP (Pa)	Particle Size (μm)	Face Velocity (cm/s)
(Tempo)-oxidized cellulose NFA [2]	99.999	348	0.125	5.3
HAP nanowire-based inorganic aerogel [44]	~99	200	$PM_{2.5}$ (Incense)	3.35
Polyimide NFA [5]	99.9	177	~0.1	25
Pul/PVA NFA [3]	99.998	550	0.208	1.5
A-lignin/G aerogel [17]	99.75	90	0.1	5.3
A-CLNFA*	99.86	59.5	0.1	5.0

*This work

6.4 Conclusion

Using a facile directional ice-templating approach and low-temperature annealing, robust, highly-efficient NFA air filters consisting of cellulose nanofibers and a small amount of lignin as reinforcing agent with preferably aligned micrometer-sized pores and hierarchical porous structures were successfully fabricated. Lignin, as a low-cost and widely available hyperbranched type of macromolecules, was verified to boost the extent of cross-linking, and when combined with thermal treatment would greatly enhance the mechanical strength and elasticity of the NFA, demonstrating their potential as durable air filters. The presence of lignin also effectively minimized the

thermally-induced shrinkage of the NFA, avoiding significant pore size reduction that may obstruct the air flow, leading to significantly lower ΔP. The filtration test results demonstrate that the addition of lignin and the aligned fibrous channels promote excellent long-term filtration efficiency over a wider range of particle sizes with anti-clogging properties, which outperforms honeycomb-like aerogels with solid cell walls. Thus, this work provides a more economically viable and environmentally benign approach to prepare robust NFA filters with sustainable high performance.

References

1.   Si, Y.; Yu, J.; Tang, X.; Ge, J.; Ding, B., Ultralight nanofibre-assembled cellular aerogels with superelasticity and multifunctionality. *Nature communications* **2014,** *5* (1), 1-9.

2.   Nemoto, J.; Saito, T.; Isogai, A., Simple freeze-drying procedure for producing nanocellulose aerogel-containing, high-performance air filters. *ACS applied materials & interfaces* **2015,** *7* (35), 19809-19815.

3.   Deuber, F.; Mousavi, S.; Federer, L.; Hofer, M.; Adlhart, C., Exploration of ultralight nanofiber aerogels as particle filters: capacity and efficiency. *ACS applied materials & interfaces* **2018,** *10* (10), 9069-9076.

4.   Wan, C.; Jiao, Y.; Wei, S.; Zhang, L.; Wu, Y.; Li, J., Functional nanocomposites from sustainable regenerated cellulose aerogels: A review. *Chemical Engineering Journal* **2019,** *359*, 459-475.

5.   Qian, Z.; Wang, Z.; Chen, Y.; Tong, S.; Ge, M.; Zhao, N.; Xu, J., Superelastic and ultralight polyimide aerogels as thermal insulators and particulate air filters. *Journal of Materials Chemistry A* **2018,** *6* (3), 828-832.

6.   Li, L.; Hu, T.; Sun, H.; Zhang, J.; Wang, A., Pressure-sensitive and conductive carbon aerogels from poplars catkins for selective oil absorption and oil/water separation. *ACS applied materials & interfaces* **2017,** *9* (21), 18001-18007.

7.   Meador, M. A. B.; Alemán, C. R.; Hanson, K.; Ramirez, N.; Vivod, S. L.; Wilmoth, N.; McCorkle, L., Polyimide aerogels with amide cross-links: a low cost alternative for mechanically strong polymer aerogels. *ACS applied materials & interfaces* **2015,** *7* (2), 1240-1249.

8.   Pakula, T.; Trznadel, M., Thermally stimulated shrinkage forces in oriented polymers: 1. Temperature dependence. *Polymer* **1985,** *26* (7), 1011-1018.

9.   Fan, J. B.; Song, Y.; Wang, S.; Meng, J.; Yang, G.; Guo, X.; Feng, L.; Jiang, L., Directly coating hydrogel on filter paper for effective oil–water separation in highly acidic, alkaline, and salty environment. *Advanced Functional Materials* **2015,** *25* (33), 5368-5375.

10.   Wang, W.; Fang, Y.; Ni, X.; Wu, K.; Wang, Y.; Jiang, F.; Riffat, S. B., Fabrication and characterization of a novel konjac glucomannan-based air filtration aerogels strengthened by wheat straw and okara. *Carbohydrate polymers* **2019,** *224*, 115129.

11.   Zhou, L.; Zhai, Y.-M.; Yang, M.-B.; Yang, W., Flexible and Tough Cellulose Nanocrystal/Polycaprolactone Hybrid Aerogel Based on the Strategy of Macromolecule Cross-Linking via Click Chemistry. *ACS Sustainable Chemistry & Engineering* **2019,** *7* (18), 15617-15627.

12.   Si, Y.; Fu, Q.; Wang, X.; Zhu, J.; Yu, J.; Sun, G.; Ding, B., Superelastic and superhydrophobic nanofiber-assembled cellular aerogels for effective separation of oil/water emulsions. *ACS nano* **2015,** *9* (4), 3791-3799.

13.   Li, X.; Lu, X.; Yang, J.; Ju, Z.; Kang, Y.; Xu, J.; Zhang, S., A facile ionic liquid approach to prepare cellulose-rich aerogels directly from corn stalks. *Green Chemistry* **2019**.

14.   Song, J.; Chen, C.; Yang, Z.; Kuang, Y.; Li, T.; Li, Y.; Huang, H.; Kierzewski, I.; Liu, B.; He, S., Highly compressible, anisotropic aerogel with aligned cellulose nanofibers. *ACS nano* **2017,** *12* (1), 140-147.

15.   Zhu, L.; Wang, Y.; Wang, Y.; You, L.; Shen, X.; Li, S., An environmentally friendly carbon aerogels derived from waste pomelo peels for the removal of organic pollutants/oils. *Microporous and Mesoporous Materials* **2017,** *241*, 285-292.

16.   Fan, P.; Yuan, Y.; Ren, J.; Yuan, B.; He, Q.; Xia, G.; Chen, F.; Song, R., Facile and green fabrication of cellulosed based aerogels for lampblack filtration from waste newspaper. *Carbohydrate polymers* **2017,** *162*, 108-114.

17.   Zeng, Z.; Ma, X. Y. D.; Zhang, Y.; Wang, Z.; Ng, B. F.; Wan, M. P.; Lu, X., Robust Lignin-Based Aerogel Filters: High-Efficiency Capture of Ultrafine Airborne Particulates and the Mechanism. *ACS Sustainable Chemistry & Engineering* **2019,** *7* (7), 6959-6968.

18.   Zhang, Y.; Zeng, Z.; Ma, X. Y. D.; Zhao, C.; Ang, J. M.; Ng, B. F.; Wan, M. P.; Wong, S.-C.; Wang, Z.; Lu, X., Mussel-inspired approach to cross-linked functional 3D nanofibrous aerogels for energy-efficient filtration of ultrafine airborne particles. *Applied Surface Science* **2019,** *479*, 700-708.

19.   Ma, X. Y. D.; Ang, J. M.; Zhang, Y.; Zeng, Z.; Zhao, C.; Chen, F.; Ng, B. F.; Wan, M. P.; Wong, S.-C.; Li, Z., Highly porous polymer nanofibrous aerogels cross-linked via spontaneous inter-fiber stereocomplexation and their potential for capturing ultrafine airborne particles. *Polymer* **2019,** *179*, 121649.

20.   Zhang, H.; Hussain, I.; Brust, M.; Butler, M. F.; Rannard, S. P.; Cooper, A. I., Aligned two-and three-dimensional structures by directional freezing of polymers and nanoparticles. *Nature materials* **2005,** *4* (10), 787-793.

21.   Gutiérrez, M. C.; Ferrer, M. L.; del Monte, F., Ice-templated materials: Sophisticated structures exhibiting enhanced functionalities obtained after unidirectional freezing and ice-segregation-induced self-assembly. *Chemistry of Materials* **2008,** *20* (3), 634-648.

22.   Qian, L.; Zhang, H., Controlled freezing and freeze drying: a versatile route for porous and micro-/nano-structured materials. *Journal of Chemical Technology & Biotechnology* **2011,** *86* (2), 172-184.

23.   Goyal, H.; Seal, D.; Saxena, R., Bio-fuels from thermochemical conversion of renewable resources: a review. *Renewable and sustainable energy reviews* **2008,** *12* (2), 504-517.

24.   Alonso, D. M.; Bond, J. Q.; Dumesic, J. A., Catalytic conversion of biomass to biofuels. *Green chemistry* **2010,** *12* (9), 1493-1513.

25.   Kumar, G.; Shobana, S.; Chen, W.-H.; Bach, Q.-V.; Kim, S.-H.; Atabani, A.; Chang, J.-S., A review of thermochemical conversion of microalgal biomass for biofuels: chemistry and processes. *Green Chemistry* **2017,** *19* (1), 44-67.

26.   Azizi, K.; Moraveji, M. K.; Najafabadi, H. A., A review on bio-fuel production from microalgal biomass by using pyrolysis method. *Renewable and Sustainable Energy Reviews* **2018,** *82*, 3046-3059.

27.   Collard, F.-X.; Blin, J., A review on pyrolysis of biomass constituents: Mechanisms and composition of the products obtained from the conversion of cellulose, hemicelluloses and lignin. *Renewable and Sustainable Energy Reviews* **2014,** *38*, 594-608.

28.   Yu, J.; Paterson, N.; Blamey, J.; Millan, M., Cellulose, xylan and lignin interactions during pyrolysis of lignocellulosic biomass. *Fuel* **2017,** *191*, 140-149.

29.   Hosoya, T.; Kawamoto, H.; Saka, S., Cellulose–hemicellulose and cellulose–lignin interactions in wood pyrolysis at gasification temperature. *Journal of analytical and applied pyrolysis* **2007,** *80* (1), 118-125.

30.   Cao, J.; Xiao, G.; Xu, X.; Shen, D.; Jin, B., Study on carbonization of lignin by TG-FTIR and high-temperature carbonization reactor. *Fuel processing technology* **2013,** *106*, 41-47.

31.   Stefanidis, S. D.; Kalogiannis, K. G.; Iliopoulou, E. F.; Michailof, C. M.; Pilavachi, P. A.; Lappas, A. A., A study of lignocellulosic biomass pyrolysis via the pyrolysis of cellulose, hemicellulose and lignin. *Journal of analytical and applied pyrolysis* **2014,** *105*, 143-150.

32.   Zhang, J.; Choi, Y. S.; Yoo, C. G.; Kim, T. H.; Brown, R. C.; Shanks, B. H., Cellulose–hemicellulose and cellulose–lignin interactions during fast pyrolysis. *ACS Sustainable Chemistry & Engineering* **2015,** *3* (2), 293-301.

33.   Scheirs, J.; Camino, G.; Tumiatti, W., Overview of water evolution during the thermal degradation of cellulose. *European Polymer Journal* **2001,** *37* (5), 933-942.

34.   Shen, D.; Gu, S.; Luo, K.; Wang, S.; Fang, M., The pyrolytic degradation of wood-derived lignin from pulping process. *Bioresource technology* **2010,** *101* (15), 6136-6146.

35.   Asmadi, M.; Kawamoto, H.; Saka, S., Thermal reactions of guaiacol and syringol as lignin model aromatic nuclei. *Journal of analytical and applied pyrolysis* **2011,** *92* (1), 88-98.

36.   Asmadi, M.; Kawamoto, H.; Saka, S., Thermal reactivities of catechols/pyrogallols and cresols/xylenols as lignin pyrolysis intermediates. *Journal of Analytical and Applied Pyrolysis* **2011,** *92* (1), 76-87.

37.   Yang, H.; Yan, R.; Chen, H.; Lee, D. H.; Zheng, C., Characteristics of hemicellulose, cellulose and lignin pyrolysis. *Fuel* **2007,** *86* (12-13), 1781-1788.

38.   Wang, S.; Wang, K.; Liu, Q.; Gu, Y.; Luo, Z.; Cen, K.; Fransson, T., Comparison of the pyrolysis behavior of lignins from different tree species. *Biotechnology Advances* **2009,** *27* (5), 562-567.

39.   See, S. W.; Balasubramanian, R.; Wang, W., A study of the physical, chemical, and optical properties of ambient aerosol particles in Southeast Asia during hazy and nonhazy days. *Journal of Geophysical Research: Atmospheres* **2006,** *111* (D10), n/a-n/a.

40.   See, S. W.; Balasubramanian, R.; Rianawati, E.; Karthikeyan, S.; Streets, D. G., Characterization and source apportionment of particulate matter≤ 2.5 μm in Sumatra, Indonesia, during a recent peat fire episode. *Environmental science & technology* **2007,** *41* (10), 3488-3494.

41.   Podgorski, A.; Bałazy, A.; Gradoń, L., Application of nanofibers to improve the filtration efficiency of the most penetrating aerosol particles in fibrous filters. *Chemical Engineering Science* **2006,** *61* (20), 6804-6815.

42.   Leung, W. W.-F.; Hung, C.-H.; Yuen, P.-T., Effect of face velocity, nanofiber packing density and thickness on filtration performance of filters with nanofibers coated on a substrate. *Separation and purification technology* **2010,** *71* (1), 30-37.

43.   Tang, M.; Chen, S.-C.; Chang, D.-Q.; Xie, X.; Sun, J.; Pui, D. Y., Filtration efficiency and loading characteristics of PM2. 5 through composite filter media consisting of commercial HVAC electret media and nanofiber layer. *Separation and Purification Technology* **2018,** *198*, 137-145.

44.   Zhang, Y.-G.; Zhu, Y.-J.; Xiong, Z.-C.; Wu, J.; Chen, F., Bioinspired Ultralight Inorganic Aerogel for Highly Efficient Air Filtration and Oil–Water Separation. *ACS applied materials & interfaces* **2018,** *10* (15), 13019-13027.

Chapter 7

Conclusion and Outlook

In this chapter, the threads of this thesis are being drawn together. The main conclusions of the works introduced in the previous chapters are summarized and linked back to the respective objectives listed in Chapter 1. The overall findings reveal that: (a) robust fibrous or non-fibrous aerogels with random or aligned porous architectures are fabricated successfully via different facile cross-linking approaches; (2) the control of the extent of cross-linking have been demonstrated to influence the structure, morphology and filtration performance of the various aerogels; (3) the aerogel filters demonstrated high filtration efficiency accompanied with a significantly lower ΔP as compared to conventional 2D fibrous filters. The understandings derived from the findings of this work can act as a guideline to design a facile approach to fabricate robust, high-performing aerogel filters for various filtration applications. Finally, based on the results obtained, some suggestions on future work are discussed.

7.1 Conclusions

In this thesis study, three types of macro/microstructural designs are employed to prepare highly efficient 3D aerogel air filters with contrastingly different hierarchical porous structures: nanofibrous aerogel (NFA) with random morphology and honeycomb-like aerogels with solid or fibrous cell walls. The aerogel fabrication method involves either freeze-drying directly in a mold or unidirectional freezing followed by freeze-drying, which would endow the aerogels with ultrahigh porosity. Since the structural properties of these highly porous materials tend to be weak, different individual cross-linking methods were also selected to study the effects of reinforcement on the mechanical properties of the respective aerogels and how the cross-linking could influence the structures and morphologies of the aerogels. In addition, selection of the starting materials is also leaned towards the fabrication of sustainable high performance filters. The potential applications of these aerogels as 3D air filters were also demonstrated and based on these results, the filtration mechanisms were elucidated. The key findings of each aerogel designs are summarized below.

Firstly, electrospun PLLA/PDLA blend nanofibers were used to prepare highly porous and isotropic NFAs via a facile freeze-drying step. It is verified that spontaneous inter-fiber stereocomplexation could take place when the PLLA/PDLA blend nanofibers come into contact, leading to inter-fiber agglutination such that the NFAs exhibited significantly enhanced compression resistance. By adjusting the mass ratio of high-molecular-weight PLLA to low-molecular-weight PDLA in the blend, the extent of stereocomplexation-induced inter-fiber agglutination could be easily controlled to achieve the desired microstructures. Filtration tests also showed that a composite filter consisting of a HEPA filter combined with a thin layer of NFA is capable of achieving higher filtration efficiency for ultrafine particles with only a slight increase in pressure drop (ΔP) compared to that of a standalone HEPA filter. Meanwhile, compared to a compact nanofibrous mat of similar mass, the larger thickness of the NFA provides a longer residence time for PM adsorption, such that

164

the probability of being adsorbed through Brownian motion is much larger, leading to a higher filtration efficiency for ultrafine particles.

The focus of the second work is to further reduce the ΔP of the aerogel filter, employ cheaper alternative starting materials and to adopt a more facile approach to prepare highly robust and porous aerogel filters. Differently, a type of non-fibrous aerogel with aligned porous channels is introduced and, the effects of cross-linking on the aerogel structure, morphology and filtration performance were studied. Using a facile unidirectional ice-crystal-induced self-assembly followed by low-temperature annealing, honeycomb-like aerogels with composite cell walls composed of cross-linked lignin and a small fraction of graphene, and aligned micrometer-sized pores was fabricated. It is shown that the aligned pore channels could improve the ease of air flow, which efficiently reduces the ΔP of the aerogels. The low-temperature annealing of biomass lignin could significantly enhance the mechanical strength, thermal stability and water/humidity resistance of the aerogels, while retaining much of the functional groups essential for PM adsorption. Besides, directional-freezing-induced self-assembly of graphene layers along the aerogel cell walls is also demonstrated to enhance the aerogel stiffness, reduce the annealing-induced volume shrinkage and facilitate the formation of more defined microstructures, which ultimately reduces the ΔP and boosts the mechanical robustness of the honeycomb-like aerogels. When used as air filters, the aerogels exhibit more superior long-term filtration efficiency for ultrafine particles accompanied with significantly lower ΔP as compared to conventional high-efficiency HEPA filters. In addition, the honeycomb-like aerogel filters demonstrate a unique air filtration mechanism, which is dissimilar to that of fibrous media.

Finally, the last part of this thesis study combines the two aerogel designs introduced in the first and second parts. The high specific surface area of NFAs promotes high PM adsorption accompanied with a ΔP that is still relatively high, while the honeycomb-like aerogels demonstrated low ΔP but with declining filtration efficiencies for larger particles. Thus, the combination of both designs could make

up for their individual shortcomings, producing a synergistic effect on the aerogel filtration performance. Similar to the second part, adopting a facile directional freezing method followed by annealing, robust, highly-efficient NFA air filters comprising of cellulose nanofibers and a small amount of lignin as cross-linking agent with aligned hierarchical porous structures were fabricated. It is verified that hyperbranched macromolecular lignin could act as spacers between the fibers and boost the cross-linking within the NFA, and together with the annealing process would greatly improve the mechanical strength and elasticity of the NFA. In addition, it is proven that lignin could also reduce the annealing-induced shrinkage of the NFAs, effectively minimizing the pore size reduction, leading to lower ΔP of the NFA filters. Compared to the honeycomb-like aerogels with solid cell walls, filtration tests reveal that the preferably aligned fibrous channels within the NFA promote outstanding long-term filtration efficiency over a wider range of particle sizes. In addition, such aligned microstructures of the NFA also give rise to anti-clogging features, which would give rise to an extended service life.

In addition, a chart is given in Figure 7.1 to provide a better overall visualization of the differences between the various filtration systems discussed in this work.
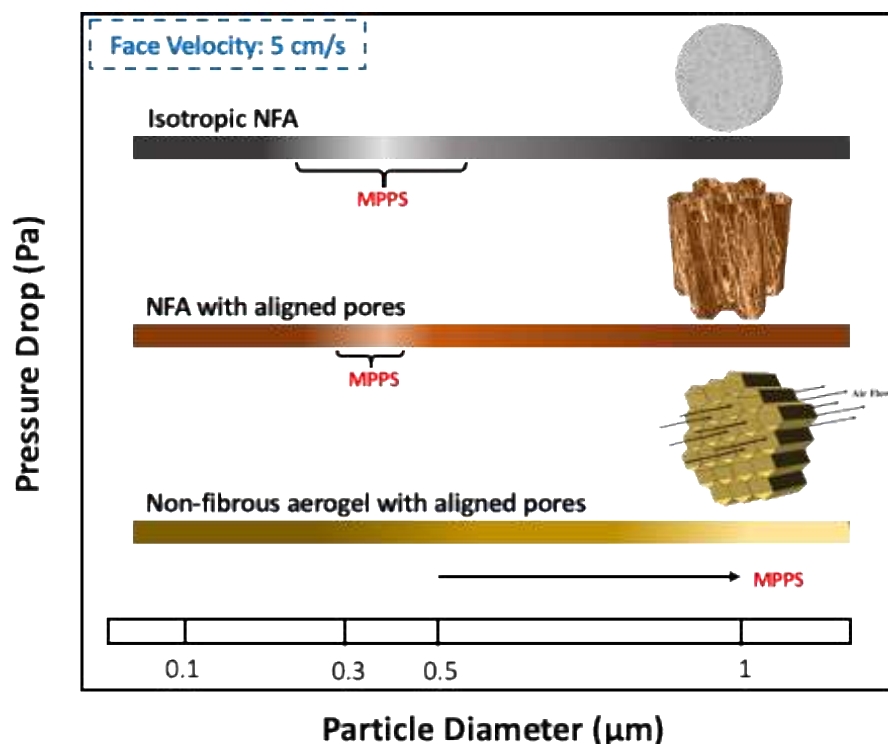
Figure 7.1 Comparison of different systems developed in this thesis work.

7.2 Significant and Novel Outcomes

This thesis study has led to several major findings and outcomes such as:

1. It is verified for the first time that stereocomplex formation can occur spontaneously at inter-fiber junctions of electrospun PLLA/PDLA blend nanofibers, which serves as cross-links to reinforce the 3D structure of the NFA. The correlation between the molecular weight of the homopolymer (PLLA or PDLA) and the extent of inter-fiber stereocomplexation within the PLLA/PDLA-SC NFA are also established, which will affect the final morphology of the NFA. With the controlled tailoring of the NFA structure, the concept of 3D air filtration was demonstrated successfully.

2. It is confirmed that aerogels with aligned micrometer-sized channels can promote the diffusion capture of ultrafine particles, while at the same time

the hollow pores would allow relatively low ΔP to be achieved. The tailoring of aerogel pore size is demonstrated to be successful simply by adjusting the concentration of lignin and GO, which can largely alter the overall filtration performance of the aerogel filter. With the filtration test conducted using different sizes of the model haze particles, the filtration mechanism of such aerogel-based filters is also proposed, i.e., size-dependent filtration efficiency with higher efficiency achieved for smaller particle size.

3. It is also verified that the presence of lignin, a hyperbranched macromolecular cross-linking agent, can boost the extent of cross-linking within a NFA with preferably aligned pores. The presence of lignin is also proven to minimize the annealing-induced shrinkage of the NFA, which could help to lessen the pore size reduction that would eventually affect the ΔP of the NFA filter. The cross-linking mechanism is also proposed in this study.

These research findings provide a good grasp of understanding on the aerogel cross-linking mechanism and their effects on the filtration performance of the aerogel filters, which will allow for the facile fabrication of aerogel-based filters for 3D air filtration. Furthermore, the proposed filtration mechanism of aerogel filters with preferably aligned pores can also set the foundation for the development of such aerogel filters for 3D air filtration applications.

7.3 Future Work

7.3.1 Regeneration of Aerogel-Based Filters

The reusability of the filter material is an important feature to ensure that the aerogel filter could offer an extended service life, which could effectively reduce the operational costs of employing these filters for air filtration purposes. In order to regenerate the filters after use, the filters have to be washed and dried, which would

often lead to mechanical-stress induced permanent deformation and shrinking of the material [1]. Since the filter materials such as fibers are in the stretched state or may contain some deformation during the fabrication process, the material have a tendency to resume a more stable state during the washing process, which induces material shrinkage. Upon washing, absorption of water also occurs, which causes swelling of the material, leading to the expansion of the material cross-section. Eventually, the material will remain in the shrunken state after the drying process. This shrinking phenomenon would alter the structure and morphology, such that the filter will no longer serve its intended purpose.

In order to investigate the reusability of our aerogels, the wash test was performed on the cellulose/lignin NFA. Although the enhanced mechanical properties of the NFA exhibited potential to be used as durable air filters, the material shrinkage was still inevitable after the wash test. In order to overcome this material shrinkage, there is a need to either release the stresses formed during the fabrication process, forge stronger cross-linking bonds to resist the mechanical deformation during washing or to reduce the swelling as a result of water absorption. Several strategies have been reported to be effective in rendering polymeric materials with shrink resistance. Yanai et. al reported a novel shrink-proof approach of cellulosic fibers via liquid ammonia treatment to transform the crystalline structure to cellulose III type, followed by a steam treatment to release the stresses within the fibers, improving the material's shrink resistance [1]. Yang et. al and Haske-Cornelius et. al incorporated glycerol as plasticizer to improve the shrinkage stabilities of their materials [2]. Ciolacu et. al exploited the reactivity of lignin and cellulose with epichlorhydrin to form stable and covalently-cross-linked hydrogels [3]. Alternatively, wu et. al also demonstrated that low swelling ratio of PVA and lignin cross-linked with epichlorohydrin can be achieved when smaller molecular weights are used or when the phenolic hydroxyl content of lignin is reduced [4]. Meanwhile, other researchers have also reported the use of lignin or cellulose reactive resin to reinforce the material. Thus, by applying one or a combination of the aforementioned strategies, the fabrication of aerogel-based filters with shrink-resistant properties may potentially be realized. It is also worthy to note that while we address the issue of

material reusability, efforts should also be devoted to investigate the degradation process of the biodegradable materials used in this study, such that there is a balance between these two properties in order for them to be potentially explored as reusable air filters.

### 7.3.2 Refining the Filtration Test Conditions

In this work, the as-prepared aerogel filters were tested using a self-assembled filtration testing setup under standard filtration testing conditions as mentioned in Chapter 3. In order to further demonstrate the potential of our aerogels as filter materials, efforts should also be devoted to test the aerogel filters under real-life environments such as air-ducts of HVAC systems of buildings or vehicles. These tests would provide a better assessment of our aerogels as potential filter materials and gives a more practical overview on the filtration performance.

7.3.3 Investigation of Antibacterial Properties of Aerogel-Based Filters

Besides addressing the most common efficiency-ΔP trade-off of air filters, the antibacterial activity of a filter is also an important issue. Although the removal of PM pollutants is the major concern in air filtration, the challenge to simultaneously eliminate airborne microorganisms, such as bacteria and viruses, is often neglected. During air filtration, especially for indoors applications, airborne microorganisms are also deposited onto the filter surface and with the appropriate amount of moisture and dust nutrients, they can start to proliferate within the filter medium [5-6], which could ultimately deteriorate the filter performance and air quality, or even cause respiratory infectious diseases [7-9]. To address this problem, many researchers have attempted to incorporate antibacterial agents in the fabrication of filters but majority focused typically on the use of CNTs [10-11] or metal/metal oxide nanoparticles such as Ag and TiO_2 as antibacterial agents [12-14], which could generate cytotoxic effects to humans, hampering their practical applications. Moreover, these antibacterial agents require an additional synthesis step during the filter fabrication process, which often involves dangerous and/or expensive chemicals. Thus, the issue of adopting

greener fabrication methods to prepare high efficiency filters with microorganism-deactivating function should also be addressed.

Research have shown that green tea leaves, a material that can be easily obtained from nature, contain cellulose (10-15%), flavonols (5-10%) and in particular, large amounts of catechins (30-40%), which are known to exhibit antibacterial behavior [15-17]. The commonly studied catechins of green tea are catechin (C) epicatechin (EC), epicatechin gallate (ECG), epigallocatechin (EGC), epigallocatechin gallate (EGCG) and gallocatechin gallate (GCG). So far, there are no reported works in the field of filtration, which explored the antibacterial activity of green tea. Hence, in this study, we adopted a facile and straightforward fabrication method to prepare spent green tea leaves (SGTL) derived NFAs with natural antibacterial function via ultra-sonication, unidirectional freezing and low temperature annealing at 290°C (Figure 7.2). It should be noted that green tea catechins are only moderately soluble in water such that significant catechin content still remains in the tea waste [18-19], which makes this recycled material suitable for the preparation of potentially antibacterial aerogel-based filters.
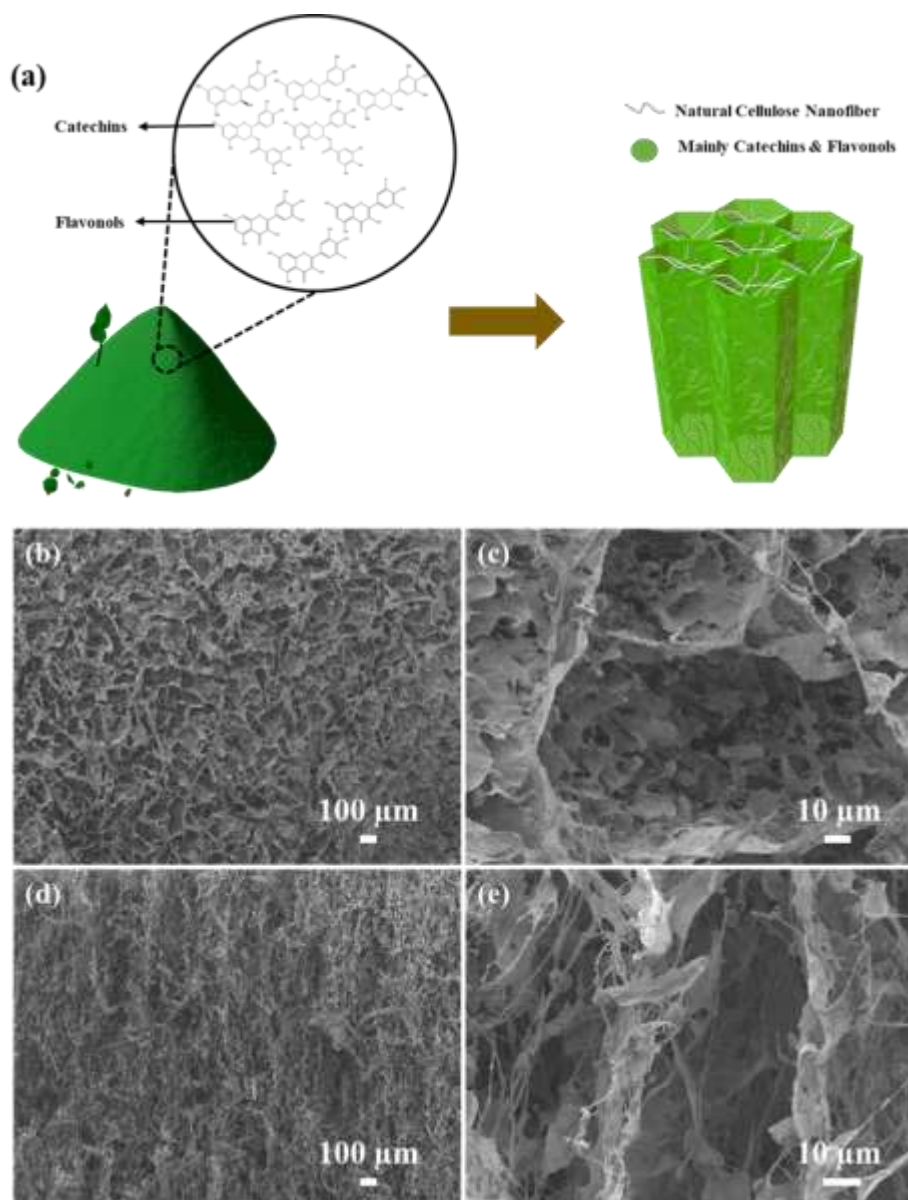
Figure 7. 2 (a) The schematic diagram of the fabrication process of SGTL NFAs. FESEM micrographs of the (b, c) top view and (d, e) cross-sections of the SGTL NFAs.

In this work, the antibacterial activities of the SGTL NFAs was investigated with *E.coli* and the samples were cultured at 37°C for a duration of 24 h. As shown in Figure 7.3, our preliminary results demonstrated obvious inhibition of bacteria growth by both the annealed and unannealed samples of the SGTL NFAs. It is also interesting to note that the annealed NFA (Figure 7.3a) exhibited stronger

antibacterial activity than the unannealed one (Figure 7.3b). This phenomenon could be attributed to the annealing process, which induces the epimerization of epigallocatechin gallate (EGCG) to gallocatechin gallate (GCG) that is largely responsible for the antibacterial activity of green tea [20-22]. Thus, to further demonstrate the advantages of the antibacterial properties of green tea in filtration applications, further tests could be performed using bacteria such as Staphylococcus or Streptococcus that are commonly found in indoor air filters. Since the SGTL NFAs is targeted to filter out bacteria-containing particles, it would be more appropriate to investigate the bacterial inhibition activity on the effective filtration area of the NFA. Furthermore, studies have shown that crude catechins, including EGCG and GCG, exhibit bacterial inhibition activity that would increase with longer incubation time when suspended in phosphate-buffered saline (PBS) solution [21], which positions the green tea as potential material to be used as long-term indoor filters. It is also reported that thermal treatment of green tea at different temperatures can affect the antibacterial activity of green tea leaves due to the loss of catechins [23]. Hence, it is also important to optimize the annealing temperature such that a balance between the mechanical properties and antibacterial activity can be achieved. Besides the bacteria inhibition activity, bacteria filtration tests should also be conducted to assess the bacteria filtration efficiency of the SGTL NFAs.
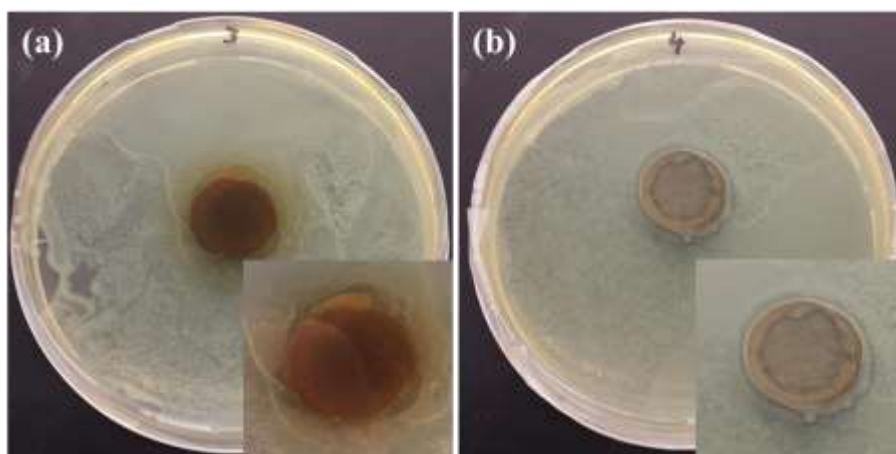
Figure 7. 3 Antibacterial activities of (a) annealed and (b) unannealed 3 wt% SGTL NFAs against *E.coli*.

References

1.   Yanai, Y.; Uno, K.; Ishikawa, T.; Isogai, T., Shrink-proof treatment of cellulosic fiber textile. Google Patents: 2002.

2.   Haske-Cornelius, O.; Bischof, S.; Beer, B.; Bartolome, M. J.; Olakanmi, E. O.; Mokoba, M.; Guebitz, G.; Nyanhongo, G., Enzymatic synthesis of highly flexible lignin cross-linked succinyl-chitosan hydrogels reinforced with reed cellulose fibres. *European Polymer Journal* **2019,** *120*, 109201.

3.   Ciolacu, D.; Oprea, A. M.; Anghel, N.; Cazacu, G.; Cazacu, M., New cellulose–lignin hydrogels and their application in controlled release of polyphenols. *Materials Science and Engineering: C* **2012,** *32* (3), 452-463.

4.   Wu, L.; Huang, S.; Zheng, J.; Qiu, Z.; Lin, X.; Qin, Y., Synthesis and characterization of biomass lignin-based PVA super-absorbent hydrogel. *International journal of biological macromolecules* **2019,** *140*, 538-545.

5.   Maus, R.; Goppelsröder, A.; Umhauer, H., Survival of bacterial and mold spores in air filter media. *Atmospheric Environment* **2001,** *35* (1), 105-113.

6.   Yoon, K. Y.; Byeon, J. H.; Park, C. W.; Hwang, J., Antimicrobial effect of silver particles on bacterial contamination of activated carbon fibers. *Environmental science & technology* **2008,** *42* (4), 1251-1255.

7.   Burger, H., Bioaerosols: prevalence and health effects in the indoor environment. *Journal of Allergy and Clinical Immunology* **1990,** *86* (5), 687-701.

8.   Douwes, J.; Thorne, P.; Pearce, N.; Heederik, D., Bioaerosol health effects and exposure assessment: progress and prospects. *The Annals of occupational hygiene* **2003,** *47* (3), 187-200.

9.   Walser, S. M.; Gerstner, D. G.; Brenner, B.; Bünger, J.; Eikmann, T.; Janssen, B.; Kolb, S.; Kolk, A.; Nowak, D.; Raulf, M., Evaluation of exposure–response relationships for health effects of microbial bioaerosols–a systematic review. *International journal of hygiene and environmental health* **2015,** *218* (7), 577-589.

10.   Park, J. H.; Yoon, K. Y.; Na, H.; Kim, Y. S.; Hwang, J.; Kim, J.; Yoon, Y. H., Fabrication of a multi-walled carbon nanotube-deposited glass fiber air filter for

the enhancement of nano and submicron aerosol particle filtration and additional antibacterial efficacy. *Science of the total environment* **2011,** *409* (19), 4132-4138.

11.   Barhate, R. S.; Ramakrishna, S., Nanofibrous filtering media: Filtration problems and solutions from tiny materials. *Journal of Membrane Science* **2007,** *296* (1–2), 1-8.

12.   Ko, Y.-S.; Joe, Y. H.; Seo, M.; Lim, K.; Hwang, J.; Woo, K., Prompt and synergistic antibacterial activity of silver nanoparticle-decorated silica hybrid particles on air filtration. *Journal of Materials Chemistry B* **2014,** *2* (39), 6714-6722.

13.   Wang, Z.; Pan, Z.; Wang, J.; Zhao, R., A novel hierarchical structured poly (lactic acid)/titania fibrous membrane with excellent antibacterial activity and air filtration performance. *Journal of Nanomaterials* **2016,** *2016*.

14.   Zhu, M.; Hua, D.; Pan, H.; Wang, F.; Manshian, B.; Soenen, S. J.; Xiong, R.; Huang, C., Green electrospun and crosslinked poly (vinyl alcohol)/poly (acrylic acid) composite membranes for antibacterial effective air filtration. *Journal of colloid and interface science* **2018,** *511*, 411-423.

15.   Graham, H. N., Green tea composition, consumption, and polyphenol chemistry. *Preventive medicine* **1992,** *21* (3), 334-350.

16.   Reto, M.; Figueira, M. E.; Filipe, H. M.; Almeida, C. M., Chemical composition of green tea (Camellia sinensis) infusions commercialized in Portugal. *Plant foods for human nutrition* **2007,** *62* (4), 139.

17.   Gopal, J.; Muthu, M.; Paul, D.; Kim, D.-H.; Chun, S., Bactericidal activity of green tea extracts: the importance of catechin containing nano particles. *Scientific reports* **2016,** *6*, 19710.

18.   Farhoosh, R.; Golmovahhed, G. A.; Khodaparast, M. H., Antioxidant activity of various extracts of old tea leaves and black tea wastes (Camellia sinensis L.). *Food Chemistry* **2007,** *100* (1), 231-236.

19.   Zhang, H.; Chen, L.; Yang, T.; Liu, Q.; Chen, X.; Zhang, Y.; Shu, G.; Li, J., Production of superfine green tea powder from processing wastes: Characterization of chemical composition and exploration of antimicrobial potential against Ralstonia solanacearum. *LWT* **2019,** *104*, 142-147.

20.   Chen, Z.-Y.; Zhu, Q. Y.; Tsang, D.; Huang, Y., Degradation of green tea catechins in tea drinks. *Journal of agricultural and food chemistry* **2001,** *49* (1), 477-482.

21.   Hara-Kudo, Y.; Yamasaki, A.; Sasaki, M.; Okubo, T.; Minai, Y.; Haga, M.; Kondo, K.; Sugita-Konishi, Y., Antibacterial action on pathogenic bacterial spore by green tea catechins. *Journal of the Science of Food and Agriculture* **2005,** *85* (14), 2354-2361.

22.   Sugita-Konishi, Y.; Hara-Kudo, Y.; Amano, F.; Okubo, T.; Aoi, N.; Iwaki, M.; Kumagai, S., Epigallocatechin gallate and gallocatechin gallate in green tea catechins inhibit extracellular release of Vero toxin from enterohemorrhagic Escherichia coli O157: H7. *Biochimica et Biophysica Acta (BBA)-General Subjects* **1999,** *1472* (1-2), 42-50.

23.   Takahashi, T.; Aso, Y.; Kasai, W.; Kondo, T., Improving the antibacterial activity against Staphylococcus aureus of composite sheets containing wasted tea leaves by roasting. *Journal of wood science* **2010,** *56* (5), 403-410.